3-26-2015

Reflections of a Wave: An Analysis of Photonic Doppler Velocimetry Systems

Brian K. Lagrange

REFLECTIONS OF A WAVE: AN ANALYSIS OF PHOTONIC DOPPLER VELOCIMETRY SYSTEMS

THESIS

Brian K. Lagrange, 2nd Lt., USAF

AFIT-ENY-MS-15-M-242

DEPARTMENT OF THE AIR FORCE
AIR UNIVERSITY

AIR FORCE INSTITUTE OF TECHNOLOGY

Wright-Patterson Air Force Base, Ohio

AFIT-ENY-MS-15-M-242

REFLECTIONS OF A WAVE: AN ANALYSIS OF PHOTONIC DOPPLER VELOCIMETRY SYSTEMS

THESIS

Presented to the Faculty

Department of Aeronautical Engineering

Graduate School of Engineering and Management

Air Force Institute of Technology

Air University

Air Education and Training Command

in Partial Fulfillment of the Requirements for the

Degree of Master of Science in Aeronautical Engineering

Brian K. Lagrange, B.S.E.E.

2nd Lt., USAF

March 16, 2015

AFIT-ENY-MS-15-M-242

REFLECTIONS OF A WAVE: AN ANALYSIS OF PHOTONIC DOPPLER VELOCIMETRY SYSTEMS

THESIS

Brian K. Lagrange, B.S.E.E.
2nd Lt., USAF

Committee Membership:

Dr. R. B. Greendyke
Chair

Dr. M. F. Reeder
Member

Maj. D. M. Liu, PhD
Member

Abstract

Munitions are one of the Air Force's most effective weapons in eliminating targets, but also one of the most expensive. Due to the inherent high-cost in deploying munitions, munition shock wave detonation must be better observed and quantified for munitions to be more cost-efficient. PDV systems have the potential to achieve this quantification of shock wave properties on a molecular scale during solid-aginst-solid impacts. The overall goal of this research was to determine whether the current photonic Doppler velocimetry (PDV) system at Eglin Air Force Base is prepared for future explosive sensitivity testing. This determination was done through an uncertainty analysis of the PDV system's results. The PDV system was given shock detonation velocities comparable to experimental explosive detonation velocities to investigate how well the system performed. This thesis concluded that the current PDV system employed by the Advanced Initiation Sciences team, (Munitions Directorate, AFRL) is capable of explosive sensitivity testing. The errors from the data results shows the current PDV system is within reasonable range to measure molecular shock wave interaction, with the highest noise fraction percentage at 5.1 percent. The highest noise fraction percentage corresponded to a peak frequency of 1.27×10^{10} Hz, which corresponds to 3700 m/s. The bounds for velocity uncertainty were between 0.41 m/s to 1.51 m/s for all data sets in this thesis which lies in accordance with past PDV experimental data.

Table of Contents

Page

List of Figures

Preface

This thesis is an original B.K. Lagrange production.

REFLECTIONS OF A WAVE: AN ANALYSIS OF PHOTONIC DOPPLER VELOCIMETRY SYSTEMS

I. Introduction

"If you are going to use military force. Use too much and deliberately use too much...You'll save lives, not only your own, but the enemy's too" [4]. This quote is by one of the Air Force's greatest warriors and leaders, General Curtis E. LeMay. General LeMay was a Chief of Staff of the Air Force in his later years, but he is more famously known for his bombing campaign against Japan in World War II. He changed the United States bombing strategy against Japan from daylight bombing to night-time bombing. On the night of March 10th, he flew alongside 325 B-29s loaded with firebomb clusters ready to bring hell to Japan, as he would say.

The first night of the firebombing campaign was devastating. The raid hit over 16 square miles of land, resulting in the killing of about 100,000 people, civilian and military included. According to the official Air Force History report of World War II, "No other air attack of the war, either in Japan or Europe, was so destructive of life and property." The nighttime firebombing campaign continued for months until the end of the war. At the end of the war, LeMay's forces had dropped incendiary munitions on 63 Japanese cities, leaving millions homeless.

Although this sort of tactic worked well in World War II, it is not popular with the majority of the global audience as seen by the civilian response to Vietnam. The Vietnam War is considered the first television war because many Americans, from the comfort of their home, were able to watch horrific visuals of civilian casualties from war fighting. These visuals led to many protests and propaganda denouncing

the American military. This unpopular opinion of the American military lasted for several years after Vietnam. In order to combat this unpopular opinion, the American military had to realize that "Total War", as defined by Clauswitz, is not possible.

About 55,000 civilian lives were claimed by United States bombings alone [22]. This number dropped significantly in the Gulf War to 3,500 civilian lives claimed from bombings [24]. This statistic included bombings from both sides of the conflict. During the Iraq War from 2003 until 2015, only 5,300 civilian casualties were accounted for by air attacks alone [1]. The majority of these casualties stemmed from the first five years in theater. This number is incredible given the time frame this number is distributed over but regardless of how precise the United States Air Force bombing is, collateral damage and casualties do not assist the troops on the ground. Our current enemies use these civilian casualties against us to win over the general population in the Middle East, mainly in Afghanistan and Syria [20]. These extremists manipulate people's anger to perform heinous acts. Al-Qaeda and the Islamic State continually gain members through the use of anti-foreign military propaganda specifically aimed at the United States Armed Forces and the collateral damage caused by warfare [6]. Terrorists' use of social media has been to their advantage with the ability to globally share their videos and pictures that promote their anti-foreign message [20]. As long as this anti-foreign promotion continues, the U.S. troops will continue having difficulty winning the hearts and minds of the middle eastern citizens [6].

This anti-foreign promotion can be attenuated through a reduction of collateral damage. Ever since the advent of asymmetric warfare, terrorists have been using guerrilla tactics and hostages to combat their enemies. These guerilla tactics prove formidable against any countries' military tactics, as shown currently in Syria, Libya, and Nigeria. The effectiveness of these tactics is because the enemy themselves do not follow the Law of Armed Conflict nor respect any haven for religion or displaced

refugees. Terrorists do not wear any formal uniforms, which makes them difficult to identify [10, p. 11]. They literally could be anyone and the military would not know it without prior intelligence. Terrorists also tend to hideout in mosques and schools, knowing the military will not attack these places because it would be against the military's rules of engagement [11]. The only way places of religious practice and public servitude can be targeted is if intelligence reveals that the specific building in question is accommodating hostiles and/or equipment related to hostile activity [2]. If this sort of intelligence is confirmed, the building becomes a legitimate target under the international Law of Armed Conflict and the military is allowed to attack the targeted building [2].

Even if the hostiles are identified, they are usually never in open areas or fields. Operations Iraqi Freedom and Enduring Freedom introduced a long-forgotten type of warfare recognized as Urban Warfare. Battles and ambushes take place in the middle of markets or even civilian's neighborhoods. This sort of urban warfare requires incredible precision and accuracy in explosive munition deployment to minimize civilian casualties. As stated before, any civilian casualties during these type of battles will just be attributed to allied military forces and used as propaganda. In order to increase precision and accuracy in munitions and reduce collateral damage, it is vital to understand explosive munitions themselves.

Explosive munitions can be detonated multiple ways but usually are pulse detonated in military application. Pulse detonated or pressure detonated explosives means the explosive is ignited when strong pressure waves can cause the explosive to detonate. The detonation event itself occurs on a microscale within the explosive. Observing these microscaled events in an explosive will lead to better manipulation of munitions in the future. The greater control the Air Force has over munitions, the fewer bombs are required to eliminate a target. Due to the reduction of deployed

bombs the Air Force will eventually save money and lives as well.

Munitions cost millions of dollars to operate in combat. The LeMay way of munition deployment would not only be highly unpopular in today's age, but it would also be exorbitantly costly. With the United States government reducing funds to national defense, munitions must be used wisely in theater and more importantly, complete the mission successfully the first time. A major problem in theater is shielding from explosive munitions [15, p. 23]. It usually requires several munitions to penetrate an enemy's defenses even behind a simple barrier, such as concrete or stone because the munition tends to detonate on impact against the barrier before reaching the target. The more munitions that are deployed, the more likely there will be collateral damage suffered by the local community. The ideal situation would be for the munition to penetrate through the defensive barrier and then detonate directly on target [15, p. 23].

In order for this ideal detonation to occur, munition detonation must be understood on a molecular level through cost-effective analysis. High-frame rate or high-speed cameras have been used in past explosive research, but they do not reveal any new information on a microscale. These sort of cameras are only useful on a macroscale. In order to overcome the limitations of a high-speed camera, it would have to be very close to the explosive and zoom in on the explosive until it can view phenomenon on a microscale. This type of experiment would be very expensive because the camera would be destroyed or at least damaged in the process of observing microscale decomposition. Recently, a new method of microscale observation using lasers and the study of velocimetry has shown the most promise of effectively analyzing shock-detonation phenomenon on a microscale in a cost-efficient manner.

Velocimetry is the study of the "velocity of fluids" and has been of great interest recently in the hydrodynamics community [23]. The reason for this sudden spark of

interest is because it allows for accurate measurements of fluid properties at temporal resolutions as small as a femtosecond in some velocimetry systems. Particularly for this research, the temporal resolutions for both the traditional and upshifted photonic Doppler Velocimetry (PDV) systems are on the nanosecond scale. The frequency resolution for both systems in this particular research is measured in gigahertz, which allows for the measurement of velocities in km/s [9]. The way a photonic Doppler Velocimetry works is that a laser source at a particular wavelength, in this case $\lambda =$ 1550 nanometers, is split into two beams [9]. The target laser beam is reflected off of the moving target and is shifted based on the Doppler effect. The reference laser and the shifted properties are combined and compared, from which target velocity can be determined [9].

The flexibility and simplicity of the system is what makes the photonic velocimetry system appealing for shock wave experimentation [9]. Wherever a Velocity Interferometer Sensor for Any Reflector (VISAR) is being used, a PDV can also be installed and also be repaired quicker if damaged [9]. Results from PDV systems have been shown to be "consistent" with VISAR readings [9]. Velocity resolution is better with PDV system than VISAR, but uncertainty has yet to be determined with PDV system which this research aims to resolve [9]. Also, there is a trade off between temporal resolution and velocity resolution in PDV systems, but "the actual limits have not been investigated" [9].

This thesis is aimed to test the upper limits of a single point PDV system and calibrate the system for future explosive sensitivity testing through an in-depth analysis of shock-wave digitization by the PDV system. The PDV system will digitize and measure shock wave velocities comparable to shock detonation velocities of explosives to test the PDV system's functionality. The experimental range of velocities will be between 1500-4000 m/s from which uncertainties will be determined. The PDV sys-

tems's overall uncertainty will be quantified in noise fraction percentage, frequency uncertainty, and velocity uncertainty. The uncertainty of this PDV system should be comparable to uncertainties from past PDV experiments in order to prove it is prepared for explosive sensitivity testing. The particular pressure at which certain explosives detonate can be more precisely estimated in the future, which in turn leads to greater control over detonation mechanisms for bombs on target. In order to gain this mastery of munitions, a better understanding of shock-initiated detonation of explosives is required to become more effective and cost-efficient in combat theater. Timing is a huge factor when deploying munitions and meticulous analysis of shock initiation of explosives will improve lethality, increase safety for munition handlers, operators, and civilians, and reduce costs to the Air Force.

II. Background

2.1 Early Initiation Theories

When the first explosives were formulated, many experiments were conducted to analyze them. It soon became apparent that an explosion is just a special case of combustion [25, p. 174]. The combustion within an explosion is dependent on "the chemical kinetics and energetics of the reaction" between the fuel and oxidant [25, p. 174]. The fuel and oxidant are usually in physical contact in most explosions [25, p. 174]. The combustion happens so rapidly in an explosion "about an initiation source that the heat generated as a consequence of the reaction cannot diffuse away from the reaction front" [25, p. 174]. This heat from the initiation source causes other ignition points to begin their combustion and "expand the gaseous products of combustion" [25, p. 175]. From these rapid reactions, the gas products are compressed because they cannot escape the reaction front and causes a "steep pressure gradient" [25, p. 175]. The pressure gradient itself becomes so steep that it eventually becomes a jump increase in pressure, "or shock wave" [25, p. 175]. This shock wave is known as the detonation wave "which then moves through the rest of the unconsumed mixture at supersonic velocity" [25, p. 175]. The velocity of the detonation wave is relative to the "speed of the sound in the undisturbed medium" [25, p. 175]. Therefore, keeping all other factors constant, materials with a higher density will have higher sound speeds, which results in higher detonation velocities [25, p. 175].

Detonation waves were first "observed around 1880 in France" [25, p. 175]. A "high-velocity flame front" was seen as it propagated down a combustion tube in several experiments back then [25, p. 175]. This phenomenon, identified as a shock wave, was explained two decades later by Chapman(1899) and Jouguet(1906) [25, p. 175]. Their explanations have been the basis for all shock wave research to this

modern day [25, p. 175]. A "reaction zone" just behind the front of a detonation wave "propagates the wave at a constant velocity through the energetic, also known as an explosive, transforming the energetic into gaseous detonation products" [25, p. 175]. The main difference between a regular shock wave and a detonation wave is that a "reaction zone" exists in a detonation wave to propel it and a regular shock wave does not contain one. It is important to keep in mind both are "steady discontinuous waves" [25, p. 175]. An analysis of how well the PDV system at Eglin AFB can trace shock-wave interaction with thin-walled materials is the sole purpose of this thesis. Detonation waves, given more resilient technology, will also be analyzed in the future as well.

Before detonation can occur, the explosive must go through a state of deflagration from a result of shock impact[25, p. 175]. Deflagrations are not as unstable as detonations, but can be stabilized "through the use of the additives and physical controls over burning rates" [25, p. 175]. Over the course of deflagration, given the correct conditions, "the gas expansion reactions transition from being controlled by the decomposition kinetics of the energetic material to the physics of the shock wave" [25, p. 175-176]. Depending on the strength of the impact, the period of time to transition from deflagration to detonation "may occur relatively slow or quick" [25, p. 176]. The faster the impact, "the higher the intensity of the shock, the more rapidly the explosive reaches a stable detonation" [25, p. 176]. Also, the containment of the energetic material helps causes Deflagration to Detonation Transition (DDT). The main difference between a deflagrant and a pure explosive is the presence of an oxidizer. A deflagrant requires an oxidizer while a pure explosive already has the oxidizer present in its chemical molecular structure. The only factor missing to ignite a pure explosive is an increase in the material's temperature which comes from a transfer of heat into the material. This heat transfer can come from both a steady

heat transfer into the energetic, like putting it in an oven, or from an increase in pressure which translates to an increase in temperature, such as a shock from impact, which is the preferred method.

2.2 Thermal Explosion Theory

According to Zukas, thermal explosion is defined as "spontaneous ignition of an energetic material which generally means the sudden inflammation of a uniformly heated mass of material" [25, p. 176]. Thermal explosion theory deals with the relative rates of heat generation from the exothermic reaction versus the sources of heat loss which are convection, conduction, and radiation [25, p. 176]. As the temperature of the "reacting medium" increases during self-heating, it eventually rises above the "temperature of the surroundings" [25, p. 176]. When the energetic material's temperature rises above the temperature of the surroundings, the heat from the material begins to leak into the surroundings through the surface of the material [25, p. 176]. As the heat dissipates to the surroundings, the reaction rate decreases [25, p. 176]. Two theories were proposed to describe this phenomenon: Semenov's Theory and Frank-Kamenetskii Theory [25, p. 176].

2.2.1 Semenov's Theory

Between 1928 and 1932, Semenov assumed an Arrhenius reaction form to the chemical oxidation of a given energetic [25, p. 176] Therefore, the rate of heat generated rises exponentially as a function of temperature but the rate of heat dissipation is a linear function of temperature [25, p. 176]. Given this information, there exists a "Critical Temperature" in which heat generation by exothermic reaction greatly exceeds heat dissipation to surroundings which results in "ignition" of an explosive [25, p. 177]. This "critical temperature" is the boundary between deflagration of an

explosive or its complete decomposition leading to detonation [25, p. 177]. Note, an explosive will always oxidize on its own. What matters is how fast this oxidation occurs to cause an ignition of the explosion.

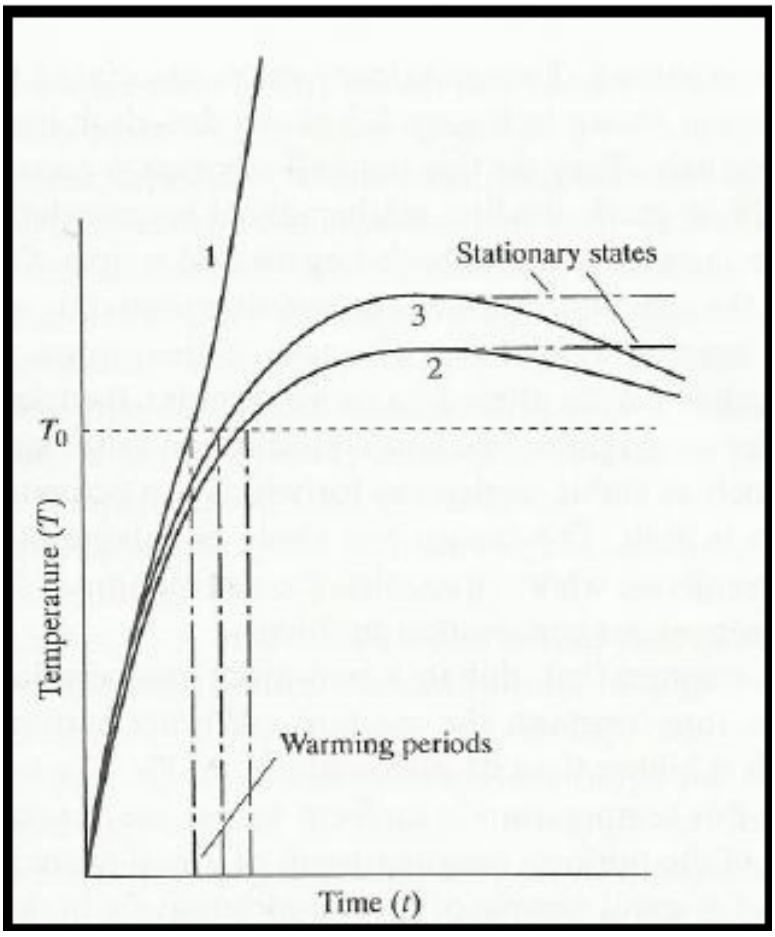

Figure 1. Temperature curves as a function of time under different conditions in self-heating [25, p. 177]

In Figure 1, each curve represents different self-heating reacting conditions for the same material [25, p. 177]. Also note in Figure 1 T_0 represents the temperature of the local environment surrounding the energetic. Curve 1 in Figure 1 represents the condition when the rate of heat generation exceeds the rate of heat loss which results in an explosion [25, p. 177]. Curve 2 in Figure 1 displays what happens

when "the rate of heat loss, after some time, exceeds the rate of heat production" [25, p. 177]. Curve 3 is the most important of the curves because it represents the peak temperature at which stable decomposition can occur which will not result in an explosion which is known as the "critical condition" [25, p. 177]. In Figure 1, as the warming periods become shorter to reach the same temperature, which means a higher rate of heat generation, the energetic will more likely explode.

In 1928, Semenov made the first mathematical representation of a critical condition but it was very simplified given the time period. It was originally a partial differential equation but Semenov had to make glaring assumptions in order to solve for it because, during that time, there were no ways to solve the partial differential equation. He assumed the energetic self-heated to a uniform temperature throughout the material, which as scientists know, is blatantly wrong due to "hot spot" theory which will be explained later in this chapter. The following equation describes heat generation according to Semenov Theory:

$$\frac{dq_1}{dt} = QV\rho A exp\left(\frac{E}{RT}\right) \tag{1}$$

Here, Q is the exothermicity of the reaction, ρ is the density of the explosive, and V is the volume of the explosive in equation (1) [25, p. 178]. To continue with equation (1), A is known as the pre-exponential factor, E is the activation energy, T is temperature, and R is the universal gas constant.

Semenov also assumed the rate of heat loss was linear, which is correct according to a Newtonian Law of Cooling, but Semenov only considered convection as the sole form of heat transfer between the energetic and its surroundings [25, p. 178]. He did not consider radiation, conduction, nor advection. The equation for heat loss according to Semenov Theory is as follows:

$$\frac{dq_2}{dt} = \chi S(\overline{T} - T_0) \tag{2}$$

In equation (2), χ is the heat transfer coefficient which Semenov assumed was independent of the temperature, but later developments showed this variable was very dependent on the temperature [25, p. 178]. S is the surface area, $\overline{T}$ is the uniform temperature of the explosive material, and T_0 is the temperature of the surroundings [25, p. 178]. When equation (1) equals equation (2), a "steady thermal state" is achieved [25, p. 178]. A steady thermal state is quite difficult to achieve in reality and is quite transitory [25, p. 179]. Semenov's research although was far from the truth in combat application, it did pioneer into a new aspect of explosives in which different forms of heat transfer became important for explosive initiation [25, p. 182]. In 1961, experiments proved that Semenov Theory aligned well with well-stirred liquids [25, p. 179]. In combat applications, the military usually utilizes solid explosives instead of liquid ones due to the higher stability of solid-molded explosives where conduction has a huge influence on initiation.

2.2.2 Frank-Kamenetskii Theory

In Semenov Theory, the main mode of heat dissipation was convection. In Frank-Kamenetskii Theory (1939), the main mode of heat dissipation was convection as well, but into the energetic itself. An erroneous assumption Frank-Kamenetskii made was that thermal conductivity between the reactant and surroundings was small, but as shown in combat missile testing, thermal conductivity must be considered as a factor especially in the coldness of high altitude. The Frank-Kamenetskii Theory is great for thin-walled containers but military projectiles are thick-walled which causes a temperature gradient in the wall or the reactant [25, p. 183]. He did consider the heat conductivity within the reactant itself as a form of heat dissipation, which contrasts

with Semenov Theory [25, p. 182]. This consideration assumes a distributed temperature in the reactant itself, where Semenov assumes a uniform temperature in the reactant, which makes Frank-Kamenetskii Theory much more realistic than Semenov [25, p. 182]. This consideration also allows for Frank-Kamenetskii to approximate "hot spot" heating as well as bulk heating for a reactant [25, p. 182]. A temperature difference, or heat sink, must exist between the center of the material and the surface. This temperature difference is important because later experiments showed that "hot spots" in an energetic begin not at the surface, but within the energetic. Experiments also have shown that resistance to heat flow in a reactant exists both at the surface and within the material itself which means realistic heat transfer exists between Semenov's and Frank-Kamenetskii's theory. Frank-Kamenetskii applies best to unstirred liquid explosives and low-conductivity solids [25, p. 183].

$$\nabla\cdot(\lambda\nabla T) = C_v\frac{\partial T}{\partial t} \tag{3}$$

Fourier's Law of Heat Conduction, as shown in equation (3), formed the basis for the equation representation of Frank-Kamenetskii's Theory [25, p. 183]. Here, λ is the thermal conductivity of the material and C_v is the heat capacity per volume [25, p. 183]. In order for equation (3) to be solved, isotropic conductivity must be assumed [25, p. 183]. After this assumption, equation (3) becomes a partial differential equation which means exact solutions were only possible for three geometries. These geometries are an infinite plane slab, an infinite circular cylinder, and a sphere. From these geometries, equation (3) can be expanded into the following:

$$\lambda\nabla^2 T - C_v\frac{\partial T}{\partial t} = -Q\cdot f(c)\cdot A exp\left(-\frac{E}{RT}\right) \tag{4}$$

In equation (4), ∇^2 represents the Laplacian operator [25, p. 183]. Also, $f(c)$ is a

function of the reactant concentration related to the material's density [25, p. 183]. The three major assumptions made in Frank-Kamenetskii were assuming steady state, assuming the energetic was in the shape of one of the three geometries, and assuming a series approximation for the exponent term [25, p. 184]. The first assumption allows for a constant density throughout the material. The second assumption is acceptable for theoretical studies but does not capture the complexities of the real world. The third assumption makes use of Semenov's identity for "critical temperature". These assumptions turned the partial differential equation into an ordinary differential equation because Frank-Kamenetskii eliminated time and two spatial dimensions but his elimination of time was highly incorrect.

$$T_{crit} = \frac{RT_0^2}{E} \tag{5}$$

This identity was reached after a Taylor Series Expansion in equation (4) for the exponential term [25, p. 185]. After lengthy non-dimensionalization using equations (5) and (4), Frank-Kamenetskii Theory was proven to be seen as the lower bound of "critical temperature" approximations while Semenov's Theory was the upper bound. A thermal explosion study by Merzhanov in 1959 of molten tetryl measured critical temperatures of the energetic at specified oven temperatures [25, p. 188]. Conclusions from this study stated that the true critical temperature was between the predicted values by Semenov and Frank-Kamenetskii [25, p. 188]. Further investigation of this study revealed that assumptions of both Semenov and Frank-Kamenetskii were violated. The thermal gradient within the reactant violated Semenov's assumption of a uniform temperature. The temperature difference between the energetic's surface and the surroundings violated the assumption of convection only happening going into the energetic. Regardless of these violations in the study, Merzhanov's experiments, through time-dependent numerical solutions, led to quantitative and qualitative in-

sight into "hotspot" initiation.

2.3 Early Detonation Theory

There is a specific "critical mass" for each explosive where anything less than this mass and the explosive will deflagrate, or burn slowly, given the explosive is in an open area uncontained [25, p. 189]. At the specific "critical mass", the explosive will detonate in an open area uncontained [25, p. 189]. The explosive still has the capability to detonate at a mass less than the critical mass "if the explosive were under confinement" [25, p. 189]. An explosive's detonation can also cause other explosives to detonate under conditions where they would not "if the explosive was subjected only to an open flame condition" [25, p. 189].

These studies on deflagration and detonation were conducted during the late nineteenth century in order to see how quickly, and specifically where in the energetic, these events occurred [25, p. 189]. Shock-wave theory was also emphasized during this time and scientists began to realize that "compression waves of finite amplitude" can be increased in small steps of pressure and velocity at the front of the wave which it will cause it to become endlessly steep [25, p. 189]. This ever-increasing steepness in the wave ultimately would result in a discontinuous, or a jump, supersonic wave known as a "shock wave" which will be described in greater detail later in this chapter [25, p. 189]. When the detonation reaches a state of stability, the chemical transformation of the explosive into gas products supplies energy to the shock wave to continue steadily or accelerate [25, p. 191].

Rarefactions appear from these gas products which merge with shocks and reduce a shock wave's amplitude and velocity [25, p. 191]. There is a "critical diameter" in which the detonation products must be greater than in order to maintain the shock wave [25, p. 191]. When the column of detonation products is greater than the

critical diameter, the rarefaction waves form "too far from the shock wave to affect the detonation front" [25, p. 191]. If the column is less than the critical diameter, the rarefaction waves collide with the detonation front and decelerate the shock wave due to the gas products expanding perpendicular to the direction of the detonation wave [25, p. 191].

Data on chemical changes is vital to the study of shock waves, especially in the hydrodynamic theory of detonation [25, p. 192]. Within this data set, the variables must include the heat of explosion, the amount of gas products, the detonation temperature, and the pressure at detonation [25, p. 192]. Multiple techniques, such as calorimetric bombs and scanning calorimeters, have been utilized to gain experimental data which are compared to theoretical solutions [25, p. 192].

2.4 Shock Initiation of Warheads

Shock initiation is the main method of detonating explosives in combat. An increase in pressure in the warhead from a shock wave causes an increase in temperature. The increase in pressure must be on the order of gigapascals for prompt detonation [25, p. 192]. The microstructure within the explosive itself is compressed into small little voids inherent in the physical structure of the material. This compression in such a small void leads to an enormous increase in temperature very rapidly within the void which affects the grains of explosive surrounding the void. These voids of extreme temperature are called "hotspots." [25, p. 188].

Hotspots are essentially where the detonation process begins and it occurs on a molecular scale. Hotspot areas are significantly hotter than the rest of the material by at least 10 orders of magnitude. There are two types of hotspots: inert and reactive [25, p. 188]. Reactive hotspots occur within the explosive itself and inert hotspots occur within the voids of the explosive material [25, p. 188]. Inert hotspots are more

likely to happen after a shock-wave passes through the explosive.

Deflagration to detonation transitions can occur when the explosive is contained but it is easier to study detonations from shock inputs [25, p. 192]. Deflagration to detonation transitions are difficult to study because the "high-confinement" systems make it difficult to observe the phenomenon [25, p. 192]. Shock inputs are much more controllable and also can be more easily observed in terms of amplitude and duration which is important for this thesis [25, p. 192]. Hopefully in the future, PDV systems can be applied to analyze how explosive material interacts with shock-waves on a molecular scale.

As stated before, this thesis deals with the shock propagation similar to that seen in flyer-type initiators used in detonators. Gap tests were performed in 1958 and 1960 to "determine the thickness of barrier required to prevent the receptor charge" in the explosive from detonating in 50% of the experimental tests [25, p. 192]. Shock initiation theory is dependent on the chemical reaction rate that is initiated by the original shock going through the barrier [25, p. 193]. In turn, the chemical reaction rate is dependent on the amplitude of the shock [25, p. 193]. The weaker the shock is, the slower reaction is, and the less likely the explosive will detonate and more likely deflagrate [25, p. 193]. The way the shock was weakened in gap tests was through the incremental increase in barrier thickness [25, p. 193]. As the barrier thickness increased, the weaker the initial shock entering the receptor became [25, p. 193]. The input shock amplitude is decreased until a threshold is reached "for a given explosive in a given geometry" where detonation does not occur [25, p. 193]. The accuracy of this input shock threshold is what this thesis lays the foundation for in future experiments. Photonic doppler velocimetry systems can give scientists better insight into improving the control of shock initiated detonations.

2.5 Hugoniots

A Hugoniot represents the loci of equilibrium products from isentropic expansion back down to equilibrium. Essentially, they represent the equation of state for a specific explosive at a certain pressure and volume. Equations of state are "all of the equilibrium states in which a material can exist and is written in terms of three variables: specific internal energy, pressure, and specific volume" [7, p. 186]. One perfect example of an equation of state is the ideal gas equation, shown below [7, p. 186].

$$PV = nRT \tag{6}$$

Gases are not of great concern within this thesis but the main interest is solids [7, p. 186]. The perfect equation of state for solids is listed below [7, p. 186].

$$e = f(P, v) \tag{7}$$

Through some equation manipulation, "the internal energy, e, term is eliminated, resulting in the following relationship" [7, p. 186].

$$P = f(v) \tag{8}$$

The equation (8) is known as the Hugoniot equation, but there are many versions of this equation [7, p. 186]. Through the use of the conservation of mass, momentum, and energy, a multiplex of variables can be related. These variables include shock velocity, U, and particle velocity, u [7, p. 186]. A list of relationships is listed below.

$$P - U, P - u, P - v, U - u, U - v, u - v \tag{9}$$

Over the years of explosives research, it was experimentally determined that "the shock velocity was linearly related to the particle velocity, for most materials" [7, p. 186]. An equation for the linear relation was developed [7, p. 186].

$$U = C_0 + su \tag{10}$$

The most useful of the variable relationships stated beforehand are the U-u plane, P-v plane, and the P-u plane [7, p. 186].

2.5.1 The U-u plane

As seen in equation (10), the shock velocity and the particle velocity are linearly related. The y-axis intercept, C_0, from equation (10) is known as the "bulk sound speed" [7, p. 186]. The term, s, represents merely the slope of the line and has no physical value [7, p. 186].

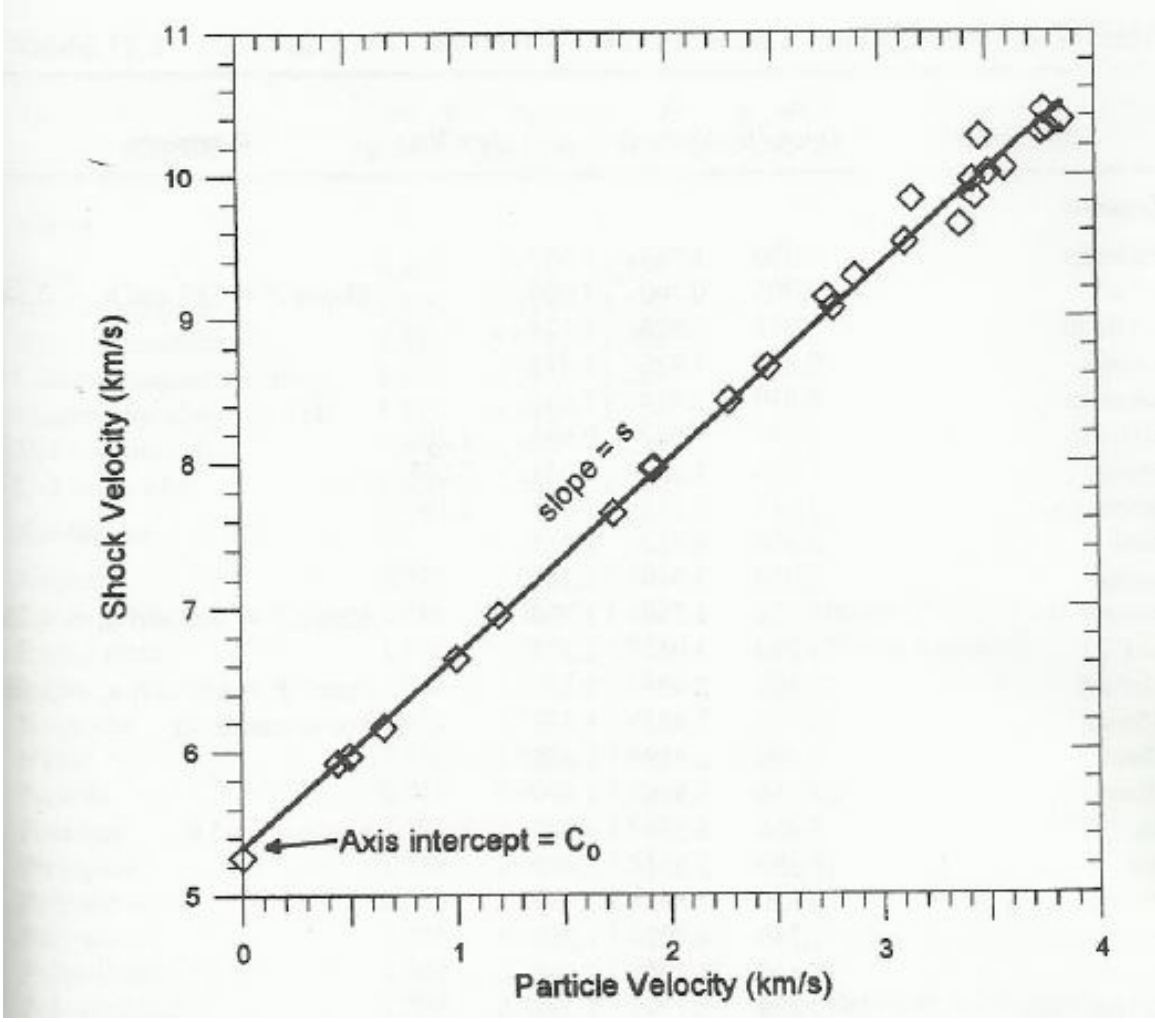

Figure 2. *U-u* Hugoniot Data for 6061 Aluminum from [7, p. 187]

The linear relationship between shock velocity and particle velocity can also be visualized on a chart, as shown in Figure 2. For a specific material, the initial shock velocity can be predicted after the particle velocity has been calculated using a graph similar to Figure 2. The square blocks on Figure 2 are shock states of that specific material and these square blocks are data points that were obtained experimentally. After plotting the data points, it was determined a first degree polynomial was the best fit curve, hence how the linear relationship was constructed. This experimentation and calculation was done for many inert materials and unreacted explosives.

As the particle velocity increases, the accuracy of the linear equation decreases as seen in Figure 2. The linear Hugoniot equations for all materials are not listed in any references across the spectrum of explosives research [7, p. 187]. How scientists work around this setback is through extrapolation from similar materials [7, p. 187]. Scientists try to match materials from "same chemical families and similar crystal structure" in order to extrapolate a linear relationship from a known material [7, p. 187]. The best case scenario from this matching methodology "will yield guesstimated values within a 10 to 15 percent range of reality" [7, p. 189].

2.5.2 The *P-u* plane

The *U-u* Hugoniot equations are manipulated to eliminate the shock velocity and just leaving *P-u* [7, p. 199]. The biggest difference between the *P-v* plane and the *P-u* plane is that the *P-v* plane is Lagrangian while the *P-u* plane is Eulerian [7, p. 199]. The *P-v* plane assumes the initial particle velocity, u_0, to be zero which meant looking at the shock "relative to the material" [7, p. 199]. The *P-u* plane takes into account the motion of the material before the shock impacts the material [7, p 199]. The Lagrangian *P-v* equation is:

$$P_1 = p_0 C_0 u_1 + p_0 s (u_1)^2 \tag{11}$$

and after an Eulerian transformation becomes [7, p. 199]

$$P_1 = p_0 C_0 (u_1 - u_0) + p_0 s (u_1 - u_0)^2 \tag{12}$$

This transformation can also be viewed visually.

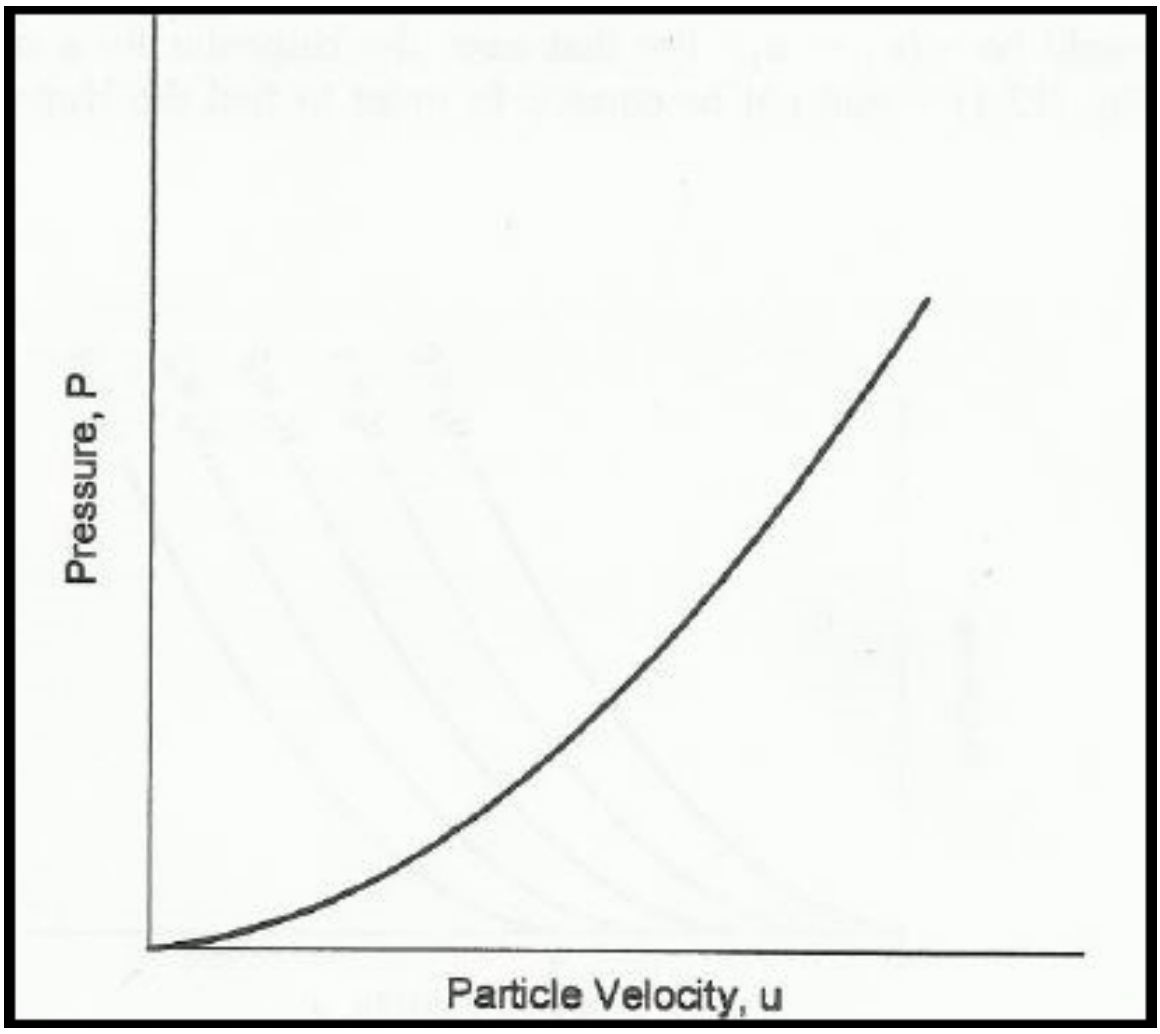

Figure 3. *P-u* Lagrangian Hugoniot Plot with u_0 at zero from [7, p. 199]

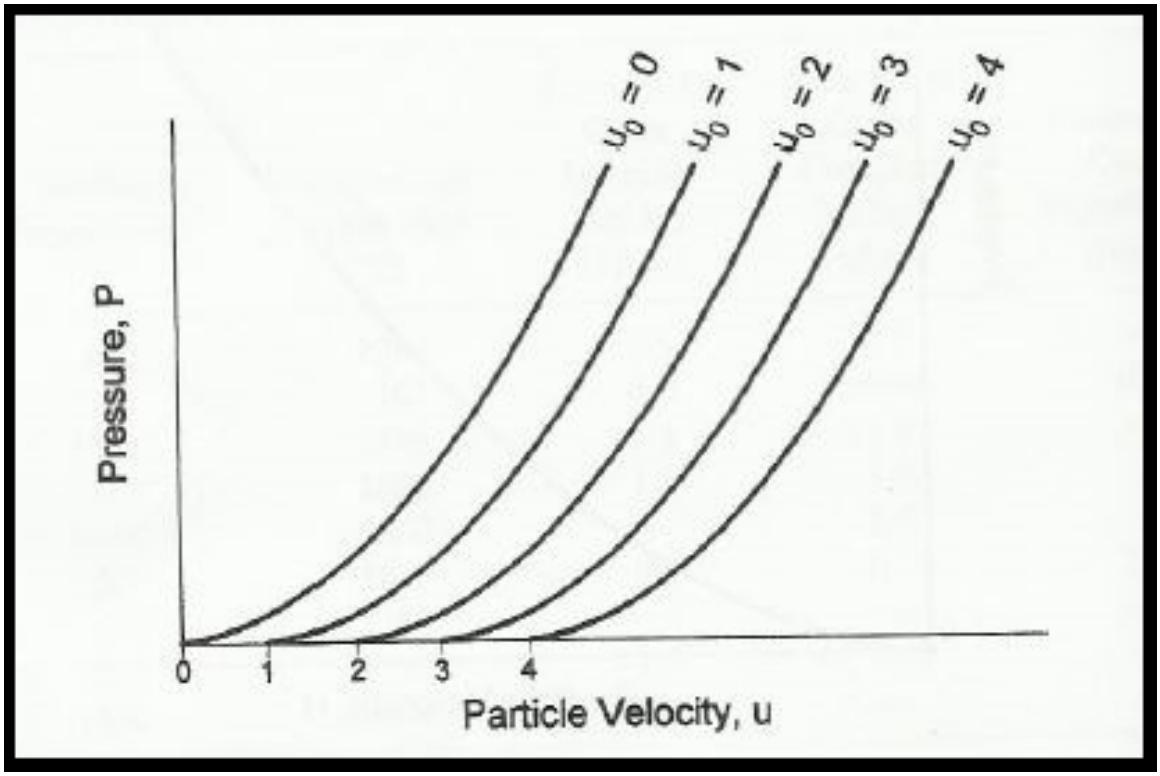

Figure 4. *P-u* Eulerian Hugoniot Plot with u_0 at different constants from [7, p. 200]

Figure 3 is Lagrangian and Figure 4 is after the Eulerian transformation [7, p. 199-200]. Each plot in the series of P-u Hugoniots in Figure 4 represent a different u_0. Each Hugoniot curve in Figure 4 represents a different initial particle velocity, but the same Hugoniot, hence why they are parallel. [7, p. 200]. The slope from initial conditions to final conditions along the Hugoniot is also a straight line, which is the same in the P-v plane [7, p. 200]. The equation for the slope of the jump is:

$$(\text{slope of jump}) = (P_1 - P_0)/(u_1 - u_0) = p_0(U - u_0) \tag{13}$$

From equation (13), "the slope of the jump condition on the P-u plane is also a function of shock velocity" [7, p. 200]. The U in equation (13), represents shock velocity with respect to laboratory coordinates [7, p. 200]. The Lagrangian shock

velocity is symbolized by the quantity $U-u_0$ [7, p. 200]. Both types of shock velocities can be solved for through simple algebra [7, p. 200].

$$(\text{slope of jump})/p_0 + u_0 = U_E \text{ Eulerian/laboratory Coordinates} \tag{14}$$

$$(\text{slope of jump})/p_0 = U_L \text{ Lagrangian Coordinates} \tag{15}$$

2.5.3 The *P-v* plane

This planar relationship was the most vital for this research because both variables can be directly measured from experiments and the relationship can easily be proven. If it is assumed P_0=0 and u_0=0 in *U-u* Hugoniot equation, an expression *P=f(v)* can be derived by discarding the particle and shock velocity terms [7, p. 189]. The Hugoniot in the *P-v* plane is expressed as the following [7, p. 191]:

$$P = ((C_0)^2)(v_0 - v)[v_0 - s(v_0 - v)]^{-2} \tag{16}$$

As stated before, a Hugoniot represents a particular material's locus of potential equilibrium states in which it can exist, not necessarily the course of stress the material takes [7, p. 191]. Multiple experiments and simulations have to be performed in order to discover each equilibrium state for a specific material [7, p. 191]. An example of these results is shown in Figure 2 for aluminum 6061 [7, p. 191]. The Hugoniot itself can be considered an isentrope for applicative purposes in engineering explosives [7, p. 191]. In theory, the Hugoniot is not the isentrope itself but the values for both are so similar, they can be considered the same for practical purposes [7, p. 193]. As pertaining to the thermodynamic laws, isentropic functions are continuous, therefore relief waves, also known as rarefactions, are continuous as well [7, p. 191]. This

characteristic of continuity is why the Hugoniot is also known as "the unloading isentrope" [7, p. 193].

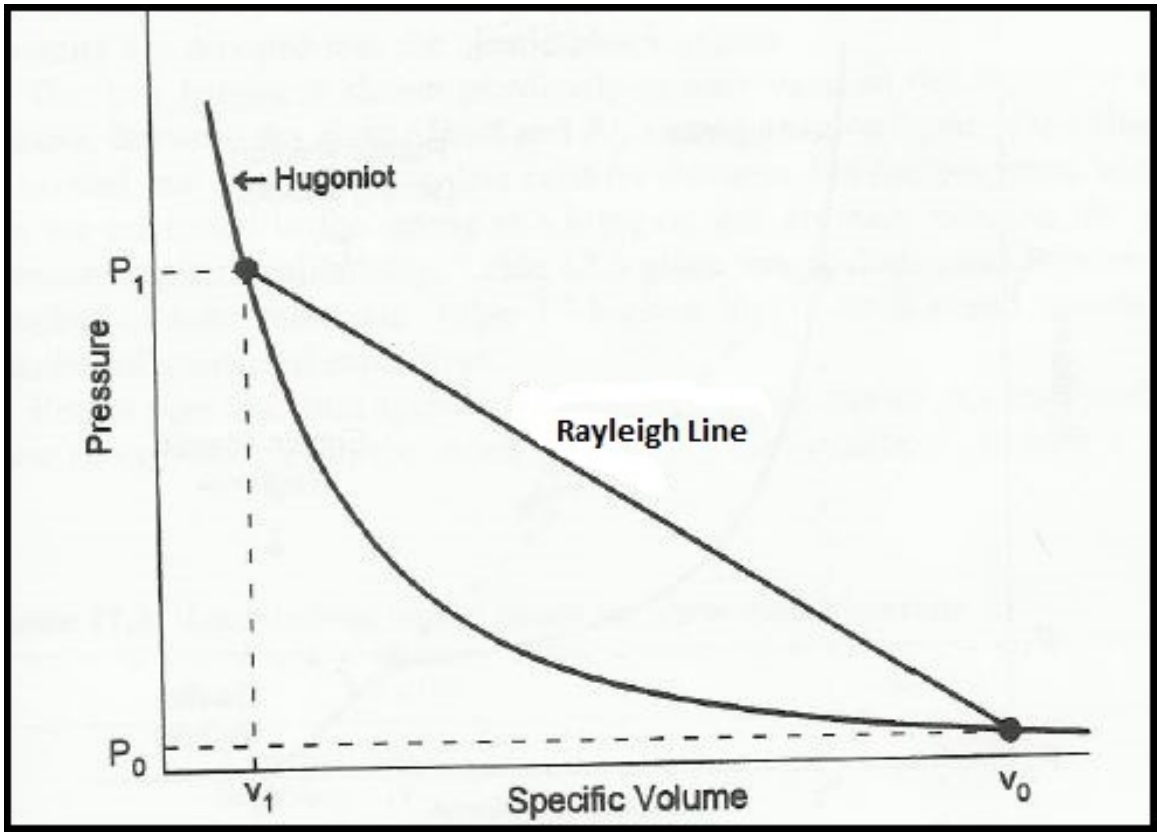

Figure 5. A general *P-v* Hugoniot from [7, p. 193]

The Hugoniot shown in Figure 5 is a chart that will be referred to quite often throughout this thesis. The Rayleigh line in Figure 5 represents the jump condition, and it "joins the initial and final states" which means it is discontinuous [7, p. 193]. The equation for the Raleigh line is as follows:

$$P_1 - P_0 = \frac{U^2}{v_0} - \frac{U^2}{v_0^2} v_1 \tag{17}$$

If equation (13) is treated as the point-slope form of a line equation, then the slope of the line is $\frac{-U^2}{v_0^2}$ [7, p. 193]. The shock velocity can be solved for from this

information, as shown below [7, p. 193]:

$$U = -(\text{slope of jump})/p_0 \tag{18}$$

Also, if either the final P-v state or the initial P-v state along with the shock velocity is known, we can solve for the other unknown state [7, p. 193].

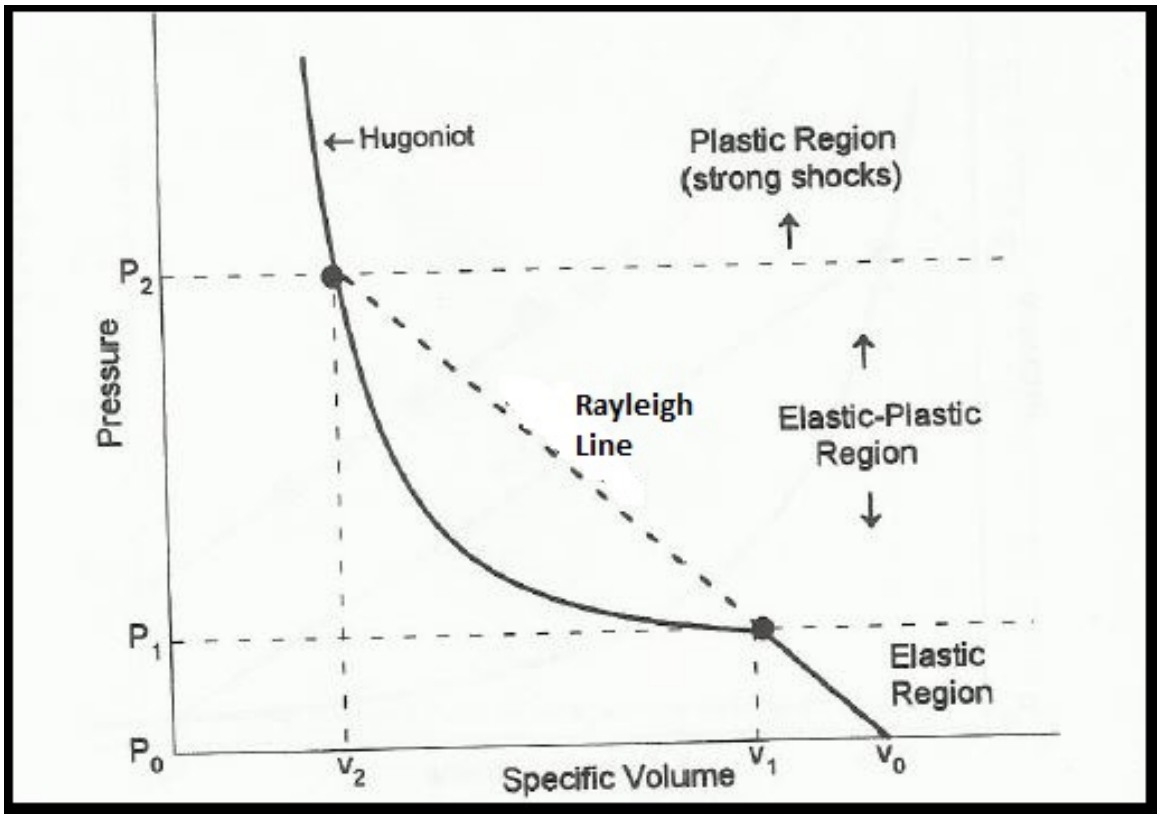

Figure 6. Elastic-Plastic Region P-v Hugoniot from [7, p. 194]

Looking at Figure 6, there are three different regions: Plastic, Elastic-Plastic, and Elastic. The line at P_1 is the "elastic limit" [7, p. 193]. The straight line going through P_0, v_0 and P_1, v_1 is just linear elastic stress-strain correlation [7, p. 194]. This correlation means any pressure waves that are contained within the elastic region will have the same longitudinal sound speed, C_L [7, p. 194]. The longitudinal sound speed

is just simply the "characteristic velocity of a uniaxial elastic wave" [7, p. 194]. This longitudinal sound speed is not the same as C_0 from the U-u, although the two are related. Generally, C_L is higher than C_0 by 15-20 percent for most materials [7, p. 194]. If a pressure wave passing through is higher than P_2 from Figure 6, it will have a "Rayleigh line slope greater than the slope of the elastic Hugoniot, and will have a shock velocity higher than C_L" [7, p. 194]. The region above P_2 is also known as the "strong shock" region, as shown in Figure 6 [7, p. 194]. This region is the "strong shock region" because "no pressure waves can be faster at the shock front than the shock velocity" and the pressure waves in this region also have a "sharp, discontinuous front" [7, p. 194]. This discontinuity at the shock front is known as the peak pressure. The plastic, or strong shock, region is investigated greatly throughout this research [7, p. 194].

As shown in Figure 6, between the elastic region and the plastic region is the elastic-plastic region. If a pressure wave from the initial state moves to any pressure between P_1 and P_2, "it will have a shock velocity below C_L" [7, p. 194]. This phenomenon is proven just by simply looking at Figure 6 because the "Rayleigh line slope is less than that of the elastic Hugoniot." A pressure wave that is within the elastic-plastic region is essentially two waves [7, p. 194]. There is an "elastic wave traveling at C_L" and a plastic shock wave whose shock velocity is given by the Rayleigh line slope at that specific pressure [7, p. 194]. Both waves are moving in the same direction, but the plastic shock wave "trails farther and farther behind" as time progresses [7, p. 194]. This progressive trailing means the wave will eventually dissipate due to the faster "elastic precursor" [7, p. 194]. Also, the rarefaction wave reaching the back of the shock helps dissipate the initial pressure wave as well [7, p. 194]. Through rarefaction and "smearing" of the wave, the pressure wave in the elastic-plastic region eventually becomes an acoustic wave [7, p. 194].

The only Hugoniot plane that exists in the strong shock region is the U-u plane. There is very little data on the elastic-plastic region due to the difficulty of measuring transitioning Hugoniots [7, p. 195].

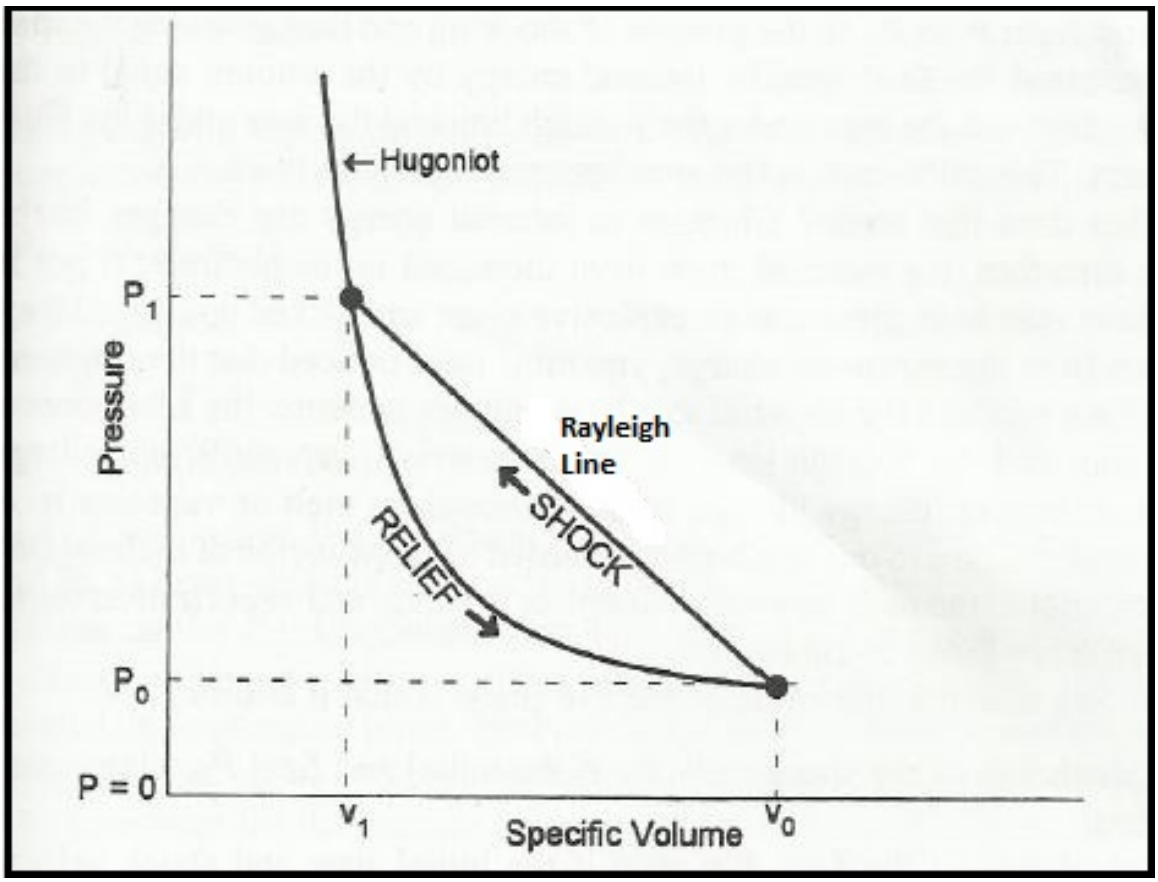

Figure 7. The path a shock takes on a *P*-*v* Hugoniot from [7, p. 197]

Figure 7 represents a visualization on how the energy transforms during the shock process in the plastic region [7, p. 195]. As stated before, the Rayleigh line represents the jump condition "from an initial state (P_0, v_0) to a state behind the shock (P_1, v_1)" [7, p. 196]. Through elimination of the shock velocity from the mass and momentum equation and assuming u_0=0, an expression for shock energy can be derived [7, p. 196].

$$\frac{1}{2}u_1^2 = \frac{1}{2}(P_1 - P_0)(v_0 - v_1) \tag{19}$$

The term on the left side of equation (19) is the "kinetic energy per unit mass of the material in the state behind the shock (KE=$\frac{1}{2}mu^2$), which is also known as the specific kinetic energy" [7, p. 196-197]. The term on the right side of equation (19) is the "area of the triangle bounded by the Rayleigh line" where the Rayleigh line represents the hypotenuse of the triangle [7, p. 197]. From equation (19), it can be deduced that if the area of the triangle increases, the specific kinetic energy will increase as well [7, p. 197]. Using the energy equation, an equation for the change in specific energy can be found [7, p. 197].

$$\begin{aligned} e_1 - e_0 &= \frac{1}{2}(P_1 + P_0)(v_0 - v_1) \\ &= \frac{1}{2}(P_1 + 2P_0 - P_0)(v_0 - v_1) \\ &= \frac{1}{2}(P_1 - P_0)(v_0 - v_1) + P_0(v_0 - v_1) \end{aligned} \tag{20}$$

This change in specific energy is equal to "the area of the triangle plus the area of the rectangle bounded by $P = P_0$, $P = 0$, $v = v_0$, and $v = v_1$" [7, p. 197]. As the pressure wave follows the path of the Rayleigh line, the relief wave follows the "path of the isentrope" which essentially is the Hugoniot [7, p. 197]. The relief wave returns the material back to its initial state at P_0, v_0 [7, p. 197]. Knowing this information about the relief wave, it can be seen from Figure 7 that "the change in specific internal energy for the relief wave is the total area under the Hugoniot segment from P_0 to P_1" [7, p. 198]. Upon further inspection of Figure 7, there is an area between the Raleigh line and the Hugoniot [7, p. 198]. The area between the Raleigh line and the Hugoniot is the "final specific internal energy" the energetic material was increased by [7, p. 198]. This observation makes sense because this area is "the difference between the area under the Raleigh line and the area under the Hugoniot segment" [7, p. 198]. The increase in the material's internal specific energy is due to an increase in temperature in the material's thermal state [7, p. 198]. This increase in temperature

was caused by an increase in pressure from the initial shock wave passing through the material [7, p. 198]. If the initial shock wave is strong enough in magnitude, "the area between the Hugoniot and the Raleigh line, for some materials, gets sufficiently large that the final internal energy change is great enough to melt or vaporize it" [7, p. 198].

2.6 Impact of Two Slabs

In order to better visualize the experiments, an example will be utilized to explain similar phenomenon seen in the experiments. Imagine there are two slabs, slabs A and B, where "slab A is flying from the left toward slab B on the right at a velocity of $u_0 = u_{0A}$" [7, p. 203]. The slabs are very thick in this case in order to better highlight rarefaction waves, but rarefaction waves are not of major importance in this thesis. Upon impact between the two slabs, "a pressure or shock pulse is formed" which moves into slab B toward the right as well to the left into slab A [7, p. 203]. In accordance with this thesis, the chip colliding with the PMMA window is slab A and the PMMA window is slab B.

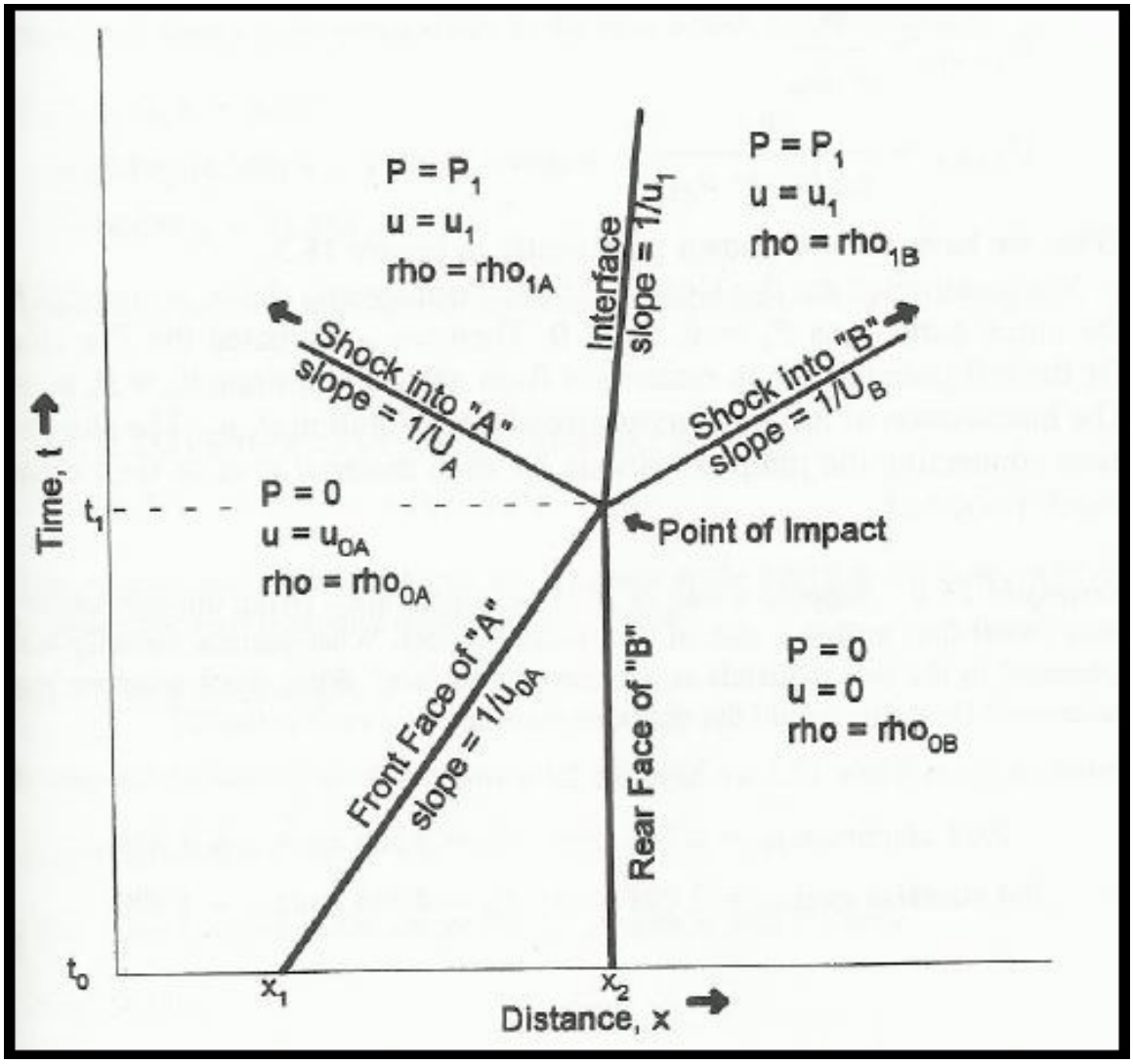

Figure 8. An x-t diagram of slab A impacting slab B from [7, p. 205]

As long as contact is maintained between slab A and slab B, the pressure and particle velocity "on both sides of the interface, must remain the same and equal" in that moment of collision [7, p. 204]. As seen in Figure 8, slab A continues to move towards slab B "as time progresses" while slab B stands still [7, p. 204]. This phenomenon can be seen by the line segment from (x_1, t_0) to (x_2, t_1) where the slope of this line segment is the reciprocal of slab A's particle velocity [7, p. 204]. Therefore as the particle velocity gets smaller, the slope becomes steeper [7, p. 204]. Any of

the shock velocities being displayed in Figure 8 are in reference to the lab coordinate system. [7, p. 204]. At time t_1, slab A impacts slab B where two shocks are essentially created: one that runs into slab A and one that runs into slab B [7, p. 204]. The shocks originated from the same impact, which means both the pressure and particle velocity are same for both materials [7, p. 204]. The shock velocities cannot be the same for both materials due to impedance, which will be explained later [7, p. 204]. Using the Hugoniot equations for both the right-running and left-running shock, the particle velocity u_1 can be solved for along with P_1 [7, p. 205].

Hugoniot for right-running shock [7, p. 204]:

$$\begin{aligned} P_R &= p_0 C_0 (u_1 - u_0) + p_0 s (u_1 - u_0)^2 \\ p_0 &= p_{0B}, C_0 = C_{0B}, s = s_B, u_0 = 0 \\ P_1 &= p_{0B} C_{0B} u_1 + p_{0B} s_B u_1^2 \end{aligned} \tag{21}$$

and the Hugoniot for left-running shock [7, p. 205]:

$$\begin{aligned} P_L &= p_0 C_0 (u_0 - u_1) + p_0 s (u_0 - u_1)^2 \\ p_0 &= p_{0A}, C_0 = C_{0A}, s = s_A, u_0 = u_{0A} \\ P_1 &= p_{0A} C_{0A} (u_{0A} - u_1) + p_{0A} s_A (u_{0A} - u_1)^2 \end{aligned} \tag{22}$$

Using the set of equations from equation (21) and equation (22), "the shock velocity in both materials can be solved for" [7, p. 206].

$$U_{LAB,B} = \frac{P_1}{u_1 p_{0B}} \tag{23}$$

$$U_{LAB,A} = \frac{P_1}{p_{0A}(u_1 - u_{0A})} + u_{0A} \tag{24}$$

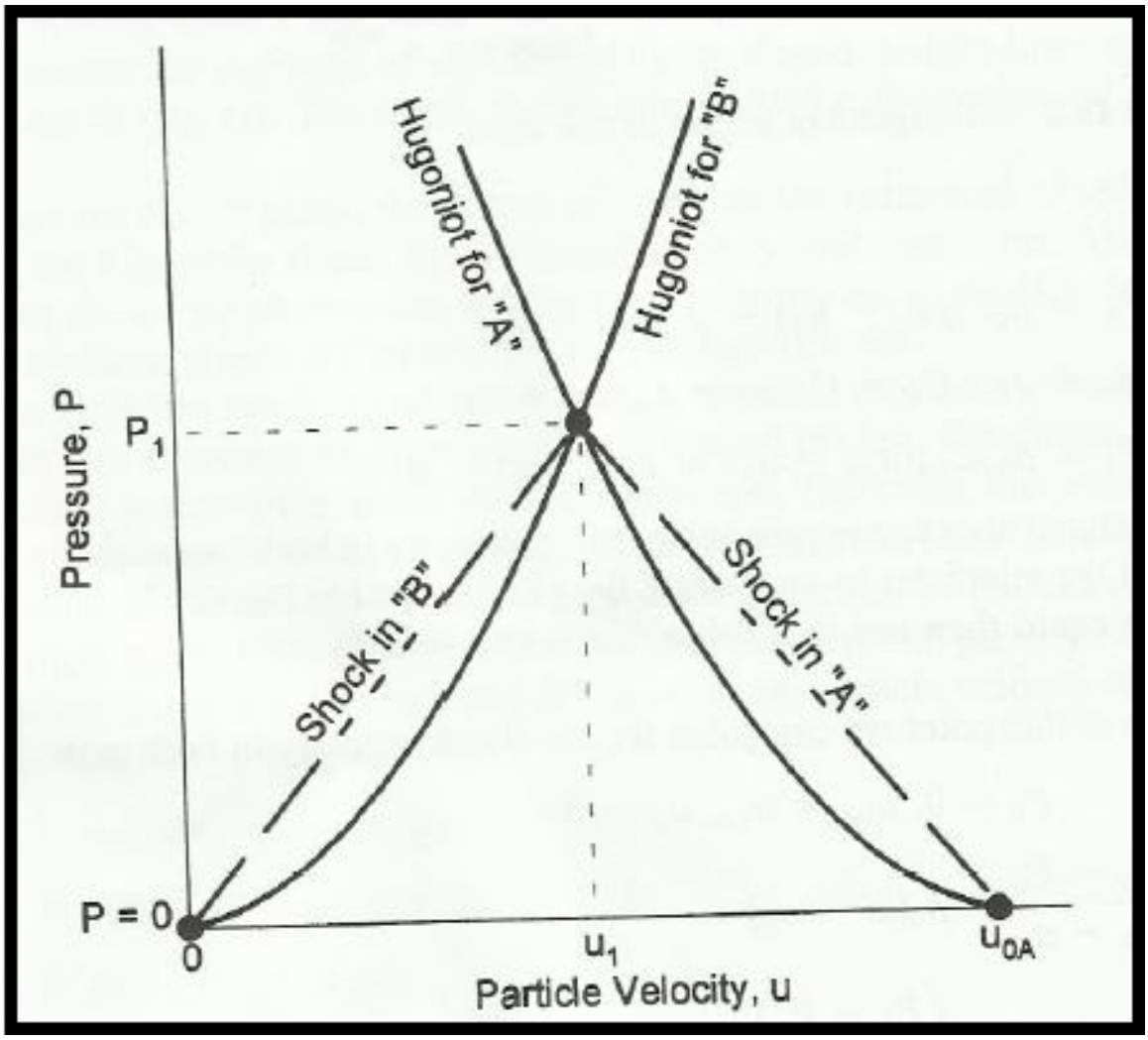

Figure 9. A P-u diagram of slab A impacting slab B from [7, p. 206]

A graphical representation of each slabs respective shock velocities and Hugoniots can be seen in Figure 9 Notice how the shock in slab A is moving from right to left and the shock in slab B is moving from left to right. The intersection of both curves in Figure 9 at P_1, u_1 represents the final jump condition for both materials [7, p. 206]. The shock velocity for each material is also the "slopes of lines connecting the jump conditions for each material" [7, p. 206].

2.6.1 Impedance: Shock at Interface

Impedance, Z in this case, is defined as "the measure of the opposition that a system presents to an acoustic flow when an acoustic pressure is applied to it" [21]. The equation for shock impedance, according to Cooper, is [7, p. 208]:

$$Z = p_0 U \tag{25}$$

As seen from equation (25), density, p_0, is one of the terms on the right side of the equation along with shock velocity, U [7, p. 208]. For this thesis, consider the shock velocity is constant as it moves through both slabs of material [7, p. 208]. Pressure increases with increasing shock velocity, as shown in the momentum equation below.

$$P = p_0 u U \tag{26}$$

The change in pressure is very slow for each material in a such a short time span that the shock velocity can be considered constant throughout the collision [7, p. 208]. Therefore, in this case, the only factor that can alter a specific material's impedance is the density [7, p. 208]. The higher the density of a material, the higher the impedance of that material given the same shock velocity when comparing to other materials [7, p. 208]. In this research, the shock will travel from a high-impedance material to a low-impedance material for every experiment, therefore only what happens to the shock during this phenomenon will be clarified[7, p. 208].

As a shock passes from a high-impedance material to a low-impedance material, the shock pressure will decrease [7, p. 208]. This in turn will decrease the particle velocity of the shock, dissipating the shock throughout the material which will lengthen the time the shock passes through the material [7, p. 208].

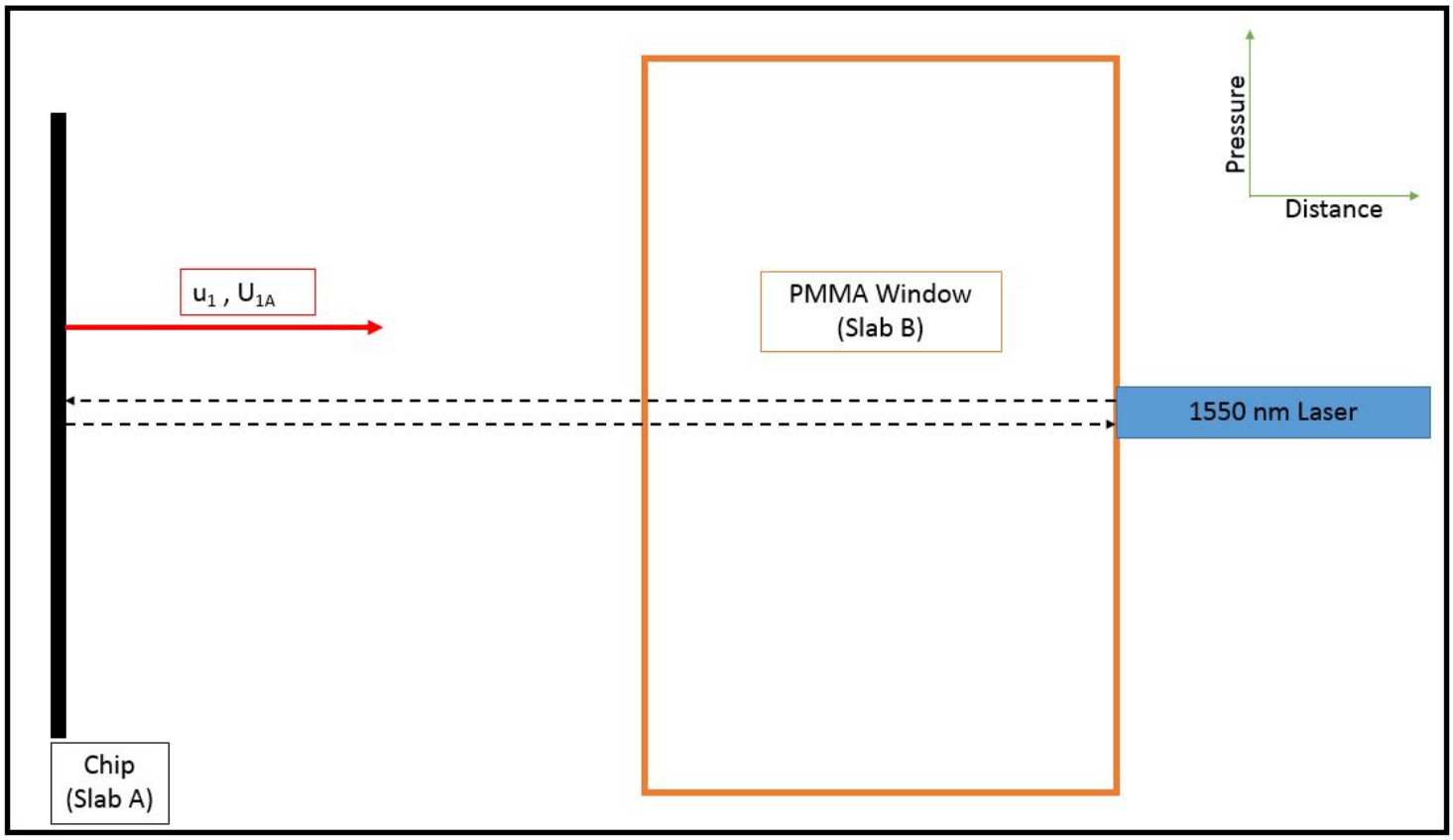

Figure 10. A P-X diagram of slab A approaching slab B

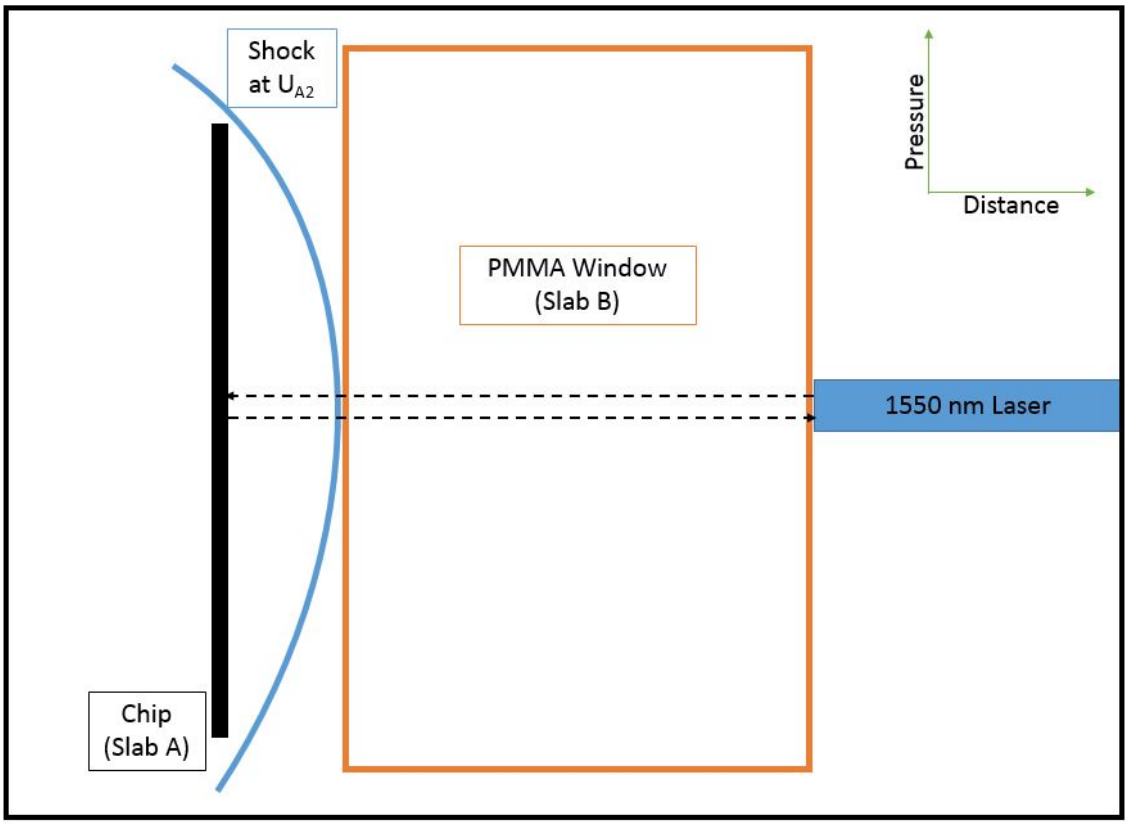

Figure 11. A P-X diagram of slab A approaching slab B just before impact from [7, p. 214]

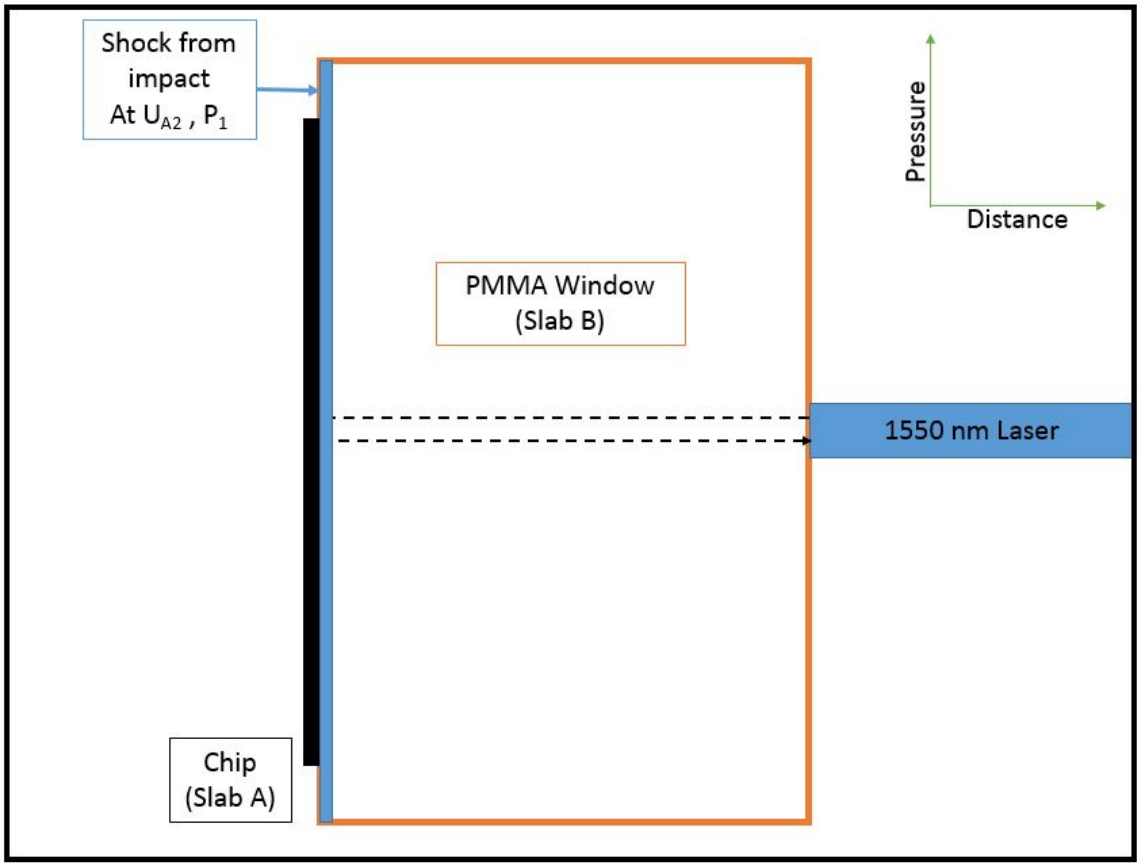

Figure 12. A P-X diagram of slab A approaching slab B at moment of impact from [7, p. 214]

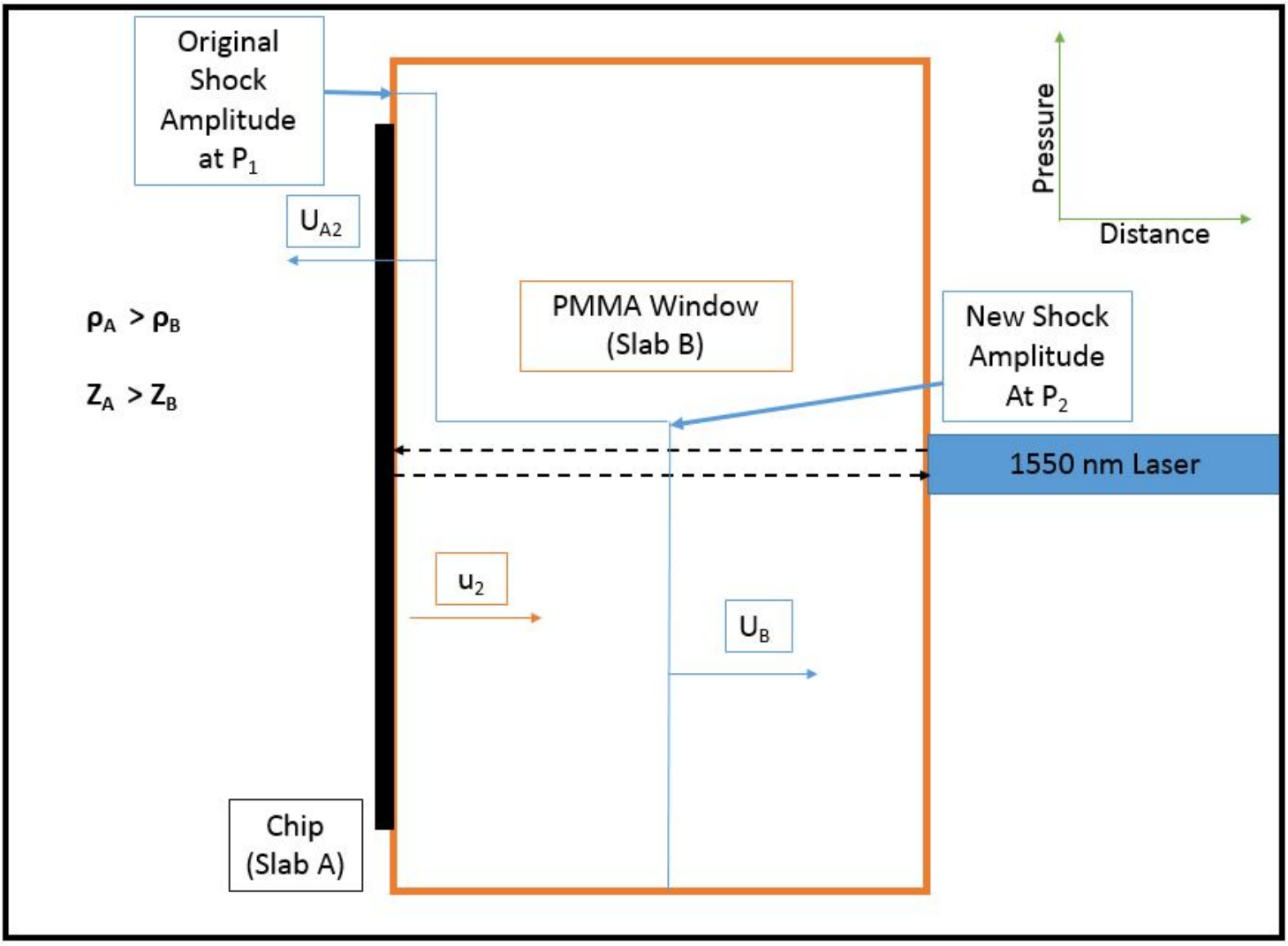

Figure 13. A P-X diagram of slab A colliding against slab B just after impact from [7, p. 215]

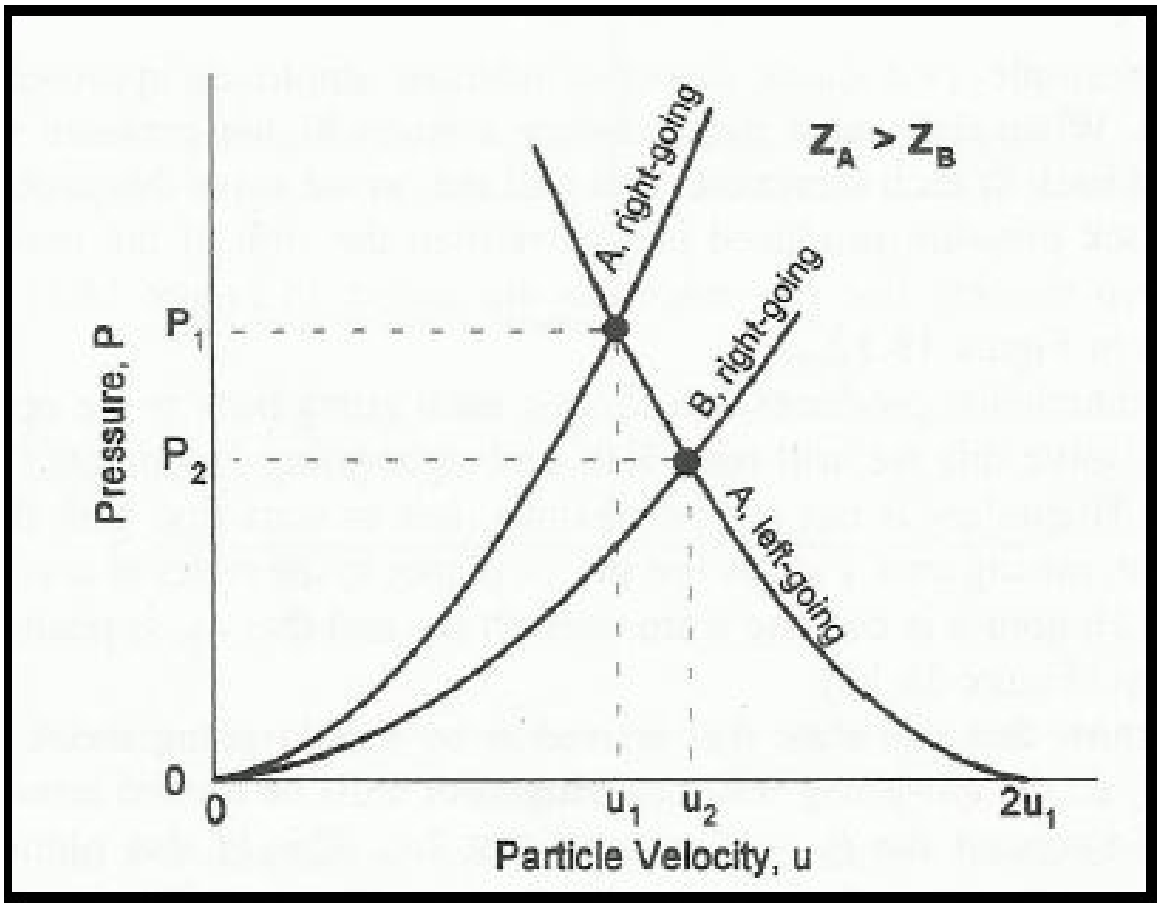

Figure 14. A shock depiction of when Z_A is greater than Z_B from [7, p. 215]

Due to the higher impedance of slab A, the Hugoniot of slab B will be lower than the Hugoniot of slab A as shown in Figure 14 [7, p. 213]. In Figure 10, slab A is approaching slab B. Slab B has all initial conditions at zero because it is stationary while slab A has specific initial conditions. In Figure 11, slab A is just about to impact slab B but the shock itself is just slightly ahead of slab A. This means the shock from slab A impacts slab B before slab A physically collides with slab B. The fact that there is a shock ahead of the flying slab is important in this thesis. In the data, this is shown as a spike in the frequency analysis, representing the highest shock pressure throughout the whole event. The spike is known as the peak pressure and will be explained later during the discussion of the results.

After the collision, a shock passes through slab A and a separate shock passes through slab B as shown in Figure 12. Both of these shocks are identical in magnitude initially. Figure 13 is the aftermath of the impact and the shocks are still passing through their respective slabs. Note the pressure for shock U_{A2} in Figure 13 is the same as the initial pressure condition because it is passing through the same material in Figure 10. The pressure for shock U_B in Figure 13 is of lower magnitude than initial conditions because the original shock is passing from a high-impedance material to a low-impedance material.

The original shock emitted from slab A at impact is essentially split into two shocks, but each shock is identical to the original. In Figure 14, the two identical shocks are represented by the slab A right-going Hugoniot and the slab A left-going Hugoniot. Note, both Hugoniots intersect at P_1 which is the same pressure of slab A at initial conditions, before impact. While the left-going Hugoniot moves away from the interface between the slabs, the right going Hugoniot goes towards the interface as shown in Figure 12. After the right-going Hugoniot passes through the interface, the right-going shock's pressure drops due to the impedance change from high to low, which can be seen in Figure 13. The drop in pressure for the right-going shock passing through the slab B material is represented by the right-going B Hugoniot in Figure 14. The right-going B Hugoniot has dropped to a pressure level of P_2 according to Figure 14. This drop in pressure will also be seen in Chapter 4.

2.7 Photonic Doppler Velocimetry (PDV) Overview and History

Photonic Doppler Velocimetry (PDV) systems were used successfully in laboratory experiments throughout the early 2000s and its flexibility was truly demonstrated during an "R-Damage series" experiment [17]. This experiment dealt with the analysis of shock waves and magnetic fields. The fact that the PDV system was still intact

and did not require recalibration after the experiments demonstrated the robustness of the system. A PDV is essentially a "Michelson interferometer" contained in optical fiber wiring which allows it to operate at high frequency. A laser at an original wavelength (λ_0) of 1550 nanometers (nm) is split into two paths. Some percentage of the laser is used as a reference laser and is aimed at the interferometer unaltered. The rest of the laser's percentage is aimed at a moving surface which causes a Doppler-shift in that percentage of the laser. The Doppler-shift results in a different laser wavelength, and hence frequency, being reflected off the moving target. The interferometer receives the Doppler-shifted light reflected off the moving surface and recombines it with the reference laser. This recombination of the two laser paths results in a fringe pattern, or beat frequency, due to the differences in wavelength from each path. This beat frequency is then proportional to the velocity of the specified moving target by $(\lambda_0)/2$ [12]. A current PDV system utilizes a wavelength of 1550 nm because of the excellent compatability this wavelength has with fiber optic cables, as proven through commercial telecommunication operations.

Highly efficient digitizers record these signals and are able to produce graphs of frequency vs. time through "Fast Fourier Transform techniques." The velocity of the moving surface can be obtained as well by just simply multiplying this frequency by $\lambda/2$ which is a constant proportionality between the velocity and the beat frequency [12]. The use of optic fiber cables in the PDV system is also what makes the system so appealing. The optic fiber cables make it more compact, lightweight, and easy to setup in a mere few hours as opposed to past interferometers which would take days to be fielded. As to be seen in data analysis, noise frequency will always be a problem but can be avoided simply through a band filter or band pass [12]. Other velocimeters, such as Velocity Interferometer System for Any Reflector (VISAR) or Fabry-Perot, operate in the amplitude domain which limit these velocimeters in cer-

tain experimental configurations [17].

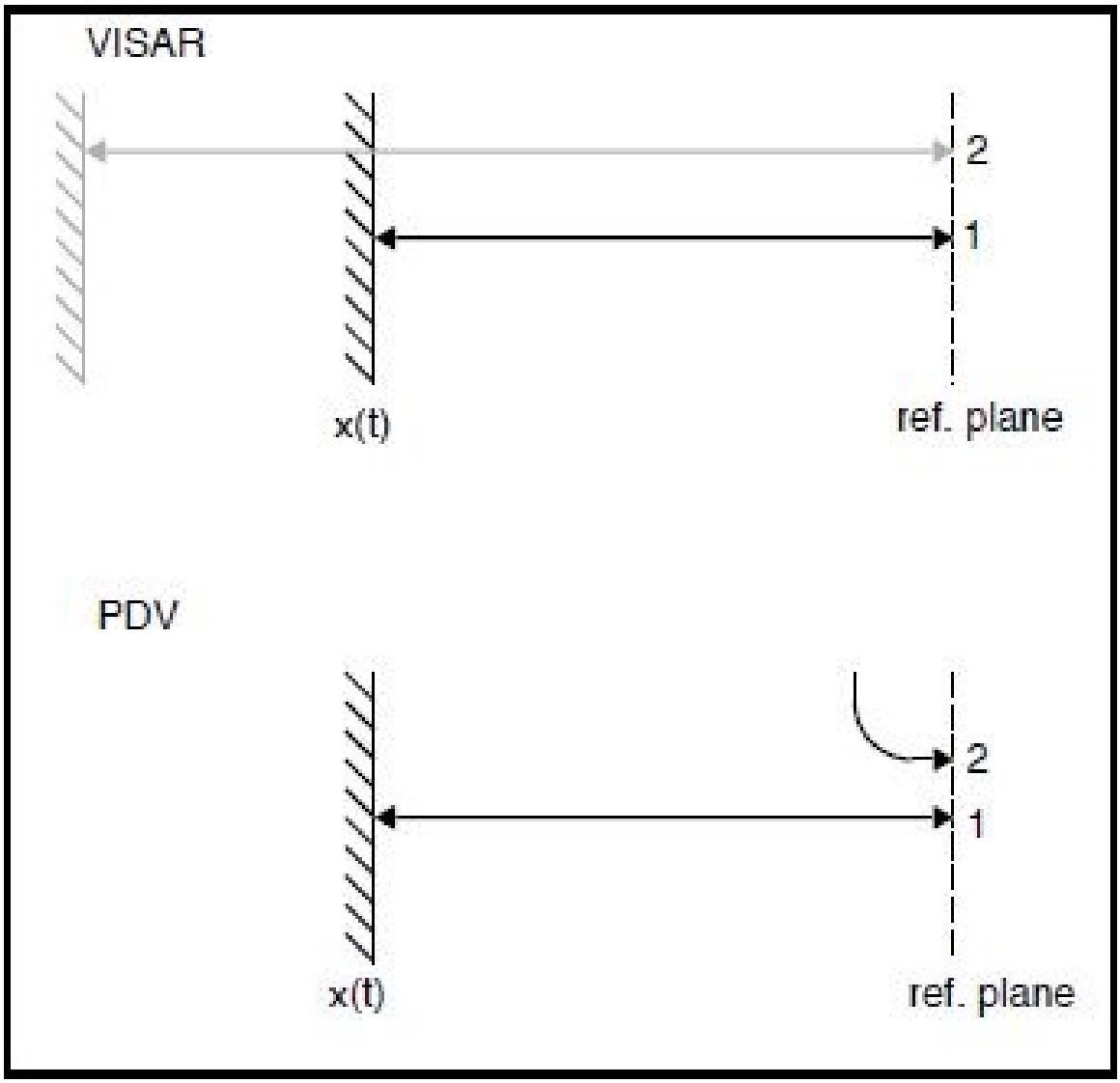

Figure 15. Differences between how VISAR measures versus how PDV measures

Also, VISAR measures position at two different discrete times while a PDV continuously measures position while the target moves as shown in Figure 15 [12]. This difference in each system's measurement procedures means a scattering shift for a change in velocity looks as a ramp for a VISAR while it looks as a step for a PDV. Analysis of signals for both VISAR and PDV is an approximation. PDV systems

operate in the frequency domain which allows for a versatile range of dynamic data analysis under "a wide variety of experimental conditions." The way displacement is measured in a PDV is that the reflected beam signal from the moving target is recorded as well as the reference beam signal in which a fringe pattern can be deduced. The sources of interference for the reflected beam signal is from the steady velocity of the analyzed target, surface roughness, and surface temperature variation. In past flyer plate shock experiments at Livermore Laboratories and Sandia, similar to this thesis research, PDV was shown to have an accuracy error of less than 0.1%. Los Alamos National Laboratory conducted a series of experiments to "measure the shock induced damage and spall of cylindrical targets" and PDV tracked the spall as well as the shock passing through the material until complete deceleration of the material.

2.7.1 Strand's Research

Dr. Oliver Ted Strand, from the Livermore National Laboratory, was a pioneer in applying PDV systems to shock physics experiments in the early 2000's[16]. Before PDV systems, interferometers could only measure velocity on "a few discrete points on a target's surface" at a very high cost. Dr. Strand led a team to design and develop a multiplexed photonic Doppler velocimetry (MPDV) that utilizes 96 optical channels to acquire velocity data at a "fraction of the former cost." PDV finds the difference between two waves, known as the "beat frequency", to determine velocity of a moving target. These two waves are "the reference laser and the Doppler-shifted light reflected from a moving surface. This method of finding the beat frequency is known as the "heterodyne method." The maximum velocity a PDV can measure is "limited by the bandwidth of the electronics and the sampling rate of the digitizers." The larger the beat frequency is, the higher the velocity.

Dr. Strand's team continued to do improvements on the MPDV system by "increasing the data-recording capacity by an order of magnitude and reduced the cost per data channel five fold." MPDV systems also "incorporates frequency- and time-division multiplexing to provide increased channel count, simultaneously measuring up to 32 discrete surface velocities onto a single digitizer" through fiber-optic cables. Dr. Strand's advancements in PDV systems provided scientists at Los Alamos and Lawrence Livermore with "high-quality data" in shock physics experiments. The scientists have utilized this data to better "predict shock and material conditions", as well as more in-depth "comparisons between computational and experimental results.

Progress in telecommunications hardware, specifically in fiber-optic technology, allowed for the effective application of PDV systems [14]. The variety of fiber-optic components that operate at 1550 nm has increased greatly since the early 2000's, "along with many high bandwidth electrical components." These components are cheap to construct, "relatively abundant", and commercially available in today's modern age. Also, the components are lightweight and fairly easy to setup and operate as well. Usually, it only takes a few hours to setup and begin recording data when installing a PDV system in a new facility.

The biggest disadvantage of PDV systems is their operable electromagnetic spectrum range. The laser operates in the infrared spectrum. It would be much more useful to have a visible wavelength laser to see "the illuminated spots on the target surface." The Advanced Initiation Sciences (AIS) team located at Eglin Air Force Base is currently constructing a green laser with a 532 nm wavelength. The visible wavelength corresponds to a frequency-doubled Nd:YAG laser which emits light at 532 nm. Another disadvantage of PDV systems is that if fluctuations in the system are too large, it could skew the dynamic range at which the PDV is taking data, causing it to overlook "low beat amplitudes."

Fiber optic cable coupling allow for the high efficiency of the PDV system [14]. The only air transport being allowed is at the probes which greatly reduces noise in the data. Most fiber cables on average have about 95-99 percent light transport efficiency, meaning 95-99 percent of the light from the source is reflected upon the moving surface [14].

Dr. Strand performed a sliding Fourier transform on his raw data from his experiments in order to obtain frequency versus time information. The raw data for this thesis used a Short Time Fourier Transform, which is slightly better than Dr. Strand's Fourier Transforms. A program, similar to Dr. Strand's, named SIRHEN by Sandia National Laboratories was sued to reduce data along with several other programs. SIRHEN will be described in great detail under the Methodology chapter. Windows of raw data are chosen to perform Fourier transforms upon, and the length of the windows present tradeoffs. Shorter windows result in better time resolution but "noiser data." Longer windows have better frequency resolution but "lower time response." User discretion is advised when reducing data to perform Fourier transforms that give results that make "physical sense."

2.7.2 Air Force Materiel Command and Air Force Research Laboratory PDV Research

In the last three years, Air Force Research Laboratory has been funding PDV research at the High Explosives Research and Development (HERD) facility located at Eglin Air Force Base under Air Force Materiel Command. In 2010, experiments were done using the PDV and a high-speed camera in order to better analyze controlled fragmentation [8]. Controlled experimental fragmentation alone is difficult to achieve, much less analyze it. The data processed by the PDV has assisted hydrocodes in predicting and modeling case failure and fragmentation [8]. The case being observed was

a scored cylinder case and the model being calibrated was the Johnson-Cook damage model. The PDV was able to obtain the average fragment velocity, approximate time to complete fragmentation, and highest peak pressure before complete fragmentation. The PDV, along with an ultra-high speed framing camera, resulted in "a coupled data set with high confidence and meaningful input to the model." The fragment distributions and mass distributions recovered from the experiment itself were then compared to the Johnson-Cook model fragment and mass distributions given the same scenario. This comparison between experimental results and computer simulated results ensued in the model's improved calibration [8].

In 2011, the HERD began doing experiments with mixture design of explosives [18]. Mixture design experimentation is "statistically rigorous" with massive amounts of data due to the small incremental changes in the explosive composition. These small changes are then processed and compared in order to find the most efficient combination of explosives for "safety and performance." A large amount of information is known about each explosive individually therefore risk is reduced when combining these explosives. Essentially, small adjustments are being made to an explosive composition and the effects of these adjustments are being analyzed. These minor chemical composition changes are in order to increase the energy of the explosive while reducing the sensitivity of the explosive but not entirely for the explosive still needs to detonate to achieve the mission. Sensitivity testing of these new explosives is what the PDV system is being prepared for in the future through this thesis. The explosive should be able to crash through multiple layers of concrete and still be able to detonate on target. In order to perform this mission successfully, explosive sensitivity must be analyzed on a microscopic scale to see effects from impact, friction, and electrostatic discharge.

III. Methodology

3.1 Data Reduction and Analysis Programs

This section will go over the three programs used in reducing the data given by the HERD at Eglin Air Force Base. The Sandia InfraRed HEtrodyne aNalysis (SIRHEN) is a program engineered by Sandia National Laboratories at Albuquerque, New Mexico. The two other programs are used jointly at the HERD PDV laboratory: pTool and PlotData. All programs result in the same data reduced plots, just with slightly different formats. SIRHEN will prove to be the most versatile of the three programs.

3.1.1 Sandia InfraRed HEtrodyne aNalysis (SIRHEN)

The program is independently operable and does not require any use of other programs to transform signals [5, p. 12]. It is operable on every commercially available platform (Mac OS X, Windows XP/Vista, and Linux) and it was written in MATrix LABoratory (MATLAB) but can only be operated on MATLAB versions 2008b or later. MATLAB is not a requirement to use this program because there is also an executable file available but can only be used on Windows XP.

PDV data can be reduced in either a displacement framework or velocity framework [5, p. 13]. The displacement mode analysis was used for this research because shock-phenomenon can be more easily seen, even though the velocity mode is the foundation of operation for the SIRHEN program [5, p. 13].

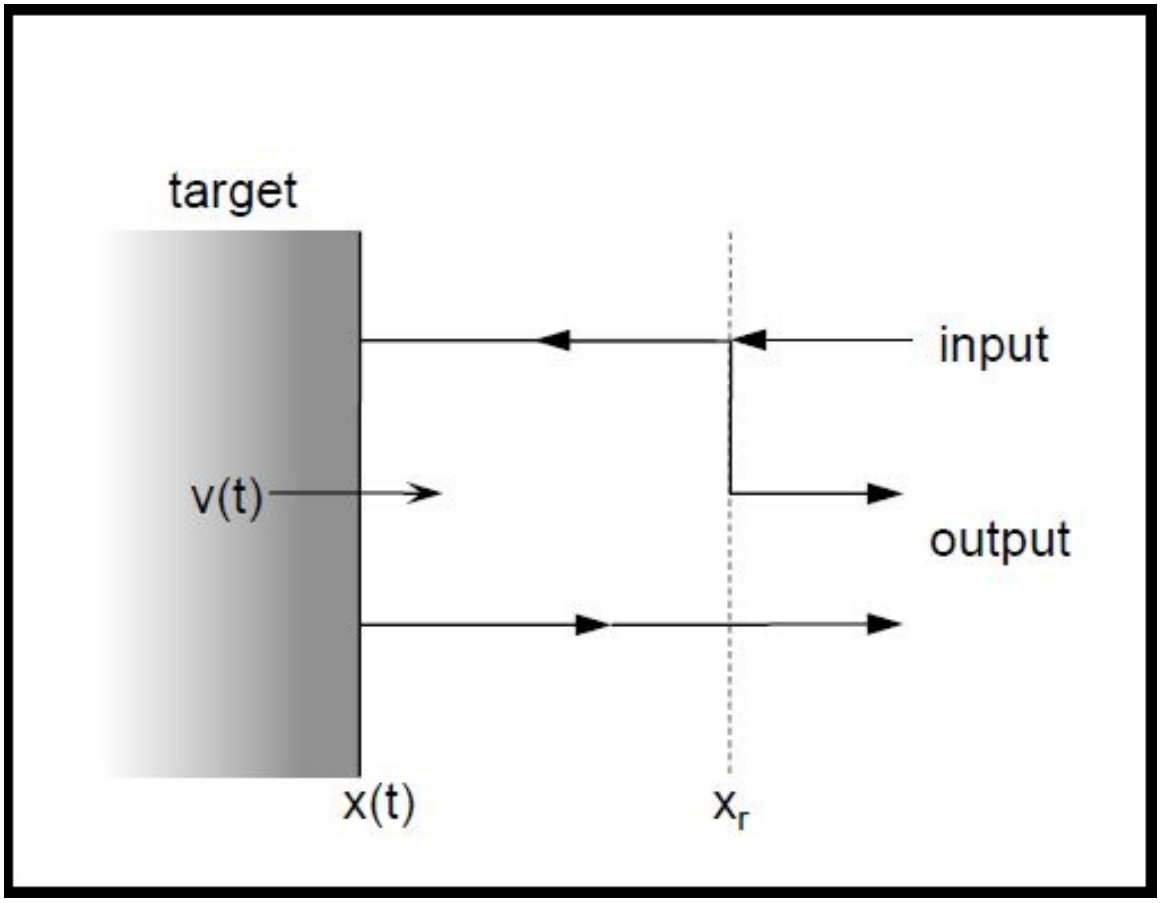

Figure 16. Conceptual figure for PDV measurement from [5, p. 14]

In the displacement mode, the light input is split into different paths as shown in Figure 16 [5, p. 13]. One path is channeled directly into the output and the other path is reflected off of the moving target at position $x(t)$ in Figure 16. The reflected light off the moving target is then combined with the "unshifted reference light" that is fed directly into the output. The combination of these two lights at position x_r results in a fringe, or interference, which creates a "beat frequency" that is proportional to the moving target's velocity at that moment. This proportionality is written in an equation below.

$$f = 2v/\lambda_0 \tag{27}$$

The wavelength is still 1550 nanometers for all PDV systems so far. Other wavelengths are being considered which will be discussed in Chapter 5. From the beat frequency, velocity can be obtained and can also be cross-examined with numerical differentiation through phase changes but this cross-examination could result in noise amplification [5, p. 16].

For the velocity mode to obtain valid results, the target must be accelerating slowly over a certain time interval, τ. The average velocity of that specific time interval is represented by $\overline{v}$ and the center of the time interval is represented by $\bar{t}$. From the prior variables, the radial beat frequency ($\overline{w}$) within the signal can be calculated as:

$$\overline{w} = \frac{4\pi\overline{v}}{\lambda_0} \tag{28}$$

A short-time Fourier transform (STFT) is then performed on that specific window of time. The STFT is able to extract the beat frequency from the peak of the power spectrum at each time of interest ($\bar{t}$) within each time duration (τ). The average velocity is then given as:

$$\overline{v} = \frac{\lambda_0}{2}\overline{f} = \frac{\lambda_0}{4\pi}\overline{w} \tag{29}$$

The resolution of the average velocity is determined by how well the frequency peak can be extracted from the STFT. SIRHEN transforms the detector signal in the time domain (represented by the input function $s(t)$) into the frequency domain (represented by the output function $S(f)$) through a discrete Fourier transform (DFT). DFT can only work successfully if the input function is discrete and the non-zero values have a finite duration. This type of Fourier transform fits perfectly for digitizing a continuous PDV electrical signal at a finite sampling rate. Normally, DFTs are time-consuming but can be computed efficiently using a fast Fourier transform

(FFT) algorithm. Discrete Fourier transforms are not to be confused with discrete-time Fourier transforms (DTFT). DFT only evaluates enough frequency components from the signal to reconstruct the original finite segment that was analyzed [5, p. 17]. This information means DFT assumes the finite segment analyzed is one complete period of an infinitely extended periodic signal, which is an erroneous assumption to make for experimental signals. In order to overcome this assumption, a window function must be used to reduce the artifacts in the spectrum. Window functions are essentially weighting functions applied to reduce spectral leakage when analyzing finite observation intervals. Spectral leakage are a series of frequency "side-lobes" that have leaked from the original signal spectrum into other frequencies. When a certain interval of a signal is being viewed using a window function, any signal data outside the interval is zeroed so all that remains is the signal segment being observed. The criteria for the spectral response of a window are the main lobe width, the attenuation of the side lobes' peaks, and the attenuation rate of the side lobes' peaks. The ideal spectral response would be a narrow main lobe, a low first-side-lobe, and rapid fall-off of the remaining side-lobes. These ideal criteria correspond to high frequency resolution and noise suppression in order to more clearly see any limitations of the PDV. SIRHEN program has four available window functions for DFT analysis: Boxcar, Hann, Hamming, and Blackman.

Table 1. Chart describing advantages of each window function in SIRHEN from [5, p. 18]

Window	Highest Side-lobe Level (dB)	Side-lobe Fall Off (dB/oct)	Comments
Boxcar	-13	-6	sensitive to signal phase
Hann	-32	-18	preferable with low noise (1%)
Hamming	-43	-6	preferable with moderate noise (5%-10%)
Blackman	-58	-18	widest main-lobe

The fact that SIRHEN has four spectral window functions, as shown in Table 1, shows how much more versatile it is than the other two programs. pTool and PlotData can only do three window functions. The advantages of each of SIRHEN's window functions are listed in Table 1 as well. The Hamming function was the function chosen for the data reduction process in this thesis. The Hamming function best suited the environment the experiments were conducted given the amount of noise from the equipment and the impact itself from the target colliding against the circular plastic plate. After using the STFT analysis to create a power spectrum, the strongest peak must be located within the spectrum.

Table 2. Chart describing advantages of each peak finding method in SIRHEN from [5, p. 21]

Method	Frequency Range	Comments
maximum	all f	velocity "hopping"
Gaussian	$f_1 \leq f \leq f_2$	computationally intensive
centroid	$f_1 \leq f \leq f_2$	computationally efficient
parabola	$f_1 \leq f \leq f_2$	fitting restricted to near peak
robust	all f	centroid method over entire data

The five-peak finding methods are listed in Table 2. Each method has its advantages and disadvantages but the Gaussian method was the best suited for this data set. Although the Gaussian method is computationally intensive, this disadvantage did not affect this data set due to the small amount data derived from each experiment. Each individual experiment itself only lasted nanoseconds hence the digitized data from these experiments could easily be computed with complex algorithms. The maximum method may seem the most attractive method because it is the least computationally intensive of the methods and will always produce a result. The accuracy of said result from the maximum method is more prone to error than the other methods[5, p. 22].

Adding "zero-padding", or generating more frequency points to the spectrum, results in a lower peak finding error for all peak finding methods. However, adding more frequency points to the spectrum will slow computation time greatly. The maximum method's most notable disadvantage is mapping out rapid transitions between "low and high velocities as the intensities of the two spectral peaks compete in magnitude" [5, p. 22]. The maximum method results in a jagged velocity history as it tracks between the two extreme frequency values. The Gaussian method produces much smoother transitions between low and high velocities which noticeably improves peak frequency location over the maximum method. Also, the Gaussian method only has a moderate amount of zero-padding to the signal which does not slow-down the computation considerably.

A standard PDV configuration was used in all of the experiments at Eglin Air Force Base. The following equation shows the relationship between time duration of a target's accelerationτ and width between peak frequencies in the STFT Δf in order to achieve an accepted precision:

$$(\Delta f)(\tau) \geq \frac{1}{4\pi} \tag{30}$$

Using the acceptable rule by equation (30) for velocities larger than 1 km/s, the relative velocity precision ($\Delta v/v$) is less than one percent. Equation (30) is the standard across all PDV research for acceptable uncertainty in velocity measurements greater than 1 km/s. This relative velocity standard is sufficient to measure and investigate dynamic material properties, such as shock waves. This relationship between time duration and peak width is what makes the PDV appealing in hydrodynamic research. This PDV configuration is utilizing a single light source to sense the moving target. If the target is not moving, then there is no beating within the PDV signal because the reflected light off the target has not been shifted. A disadvantage of this configuration is that it does not do well with low velocity since the beat period of the PDV system is longer than the time duration of the analysis.

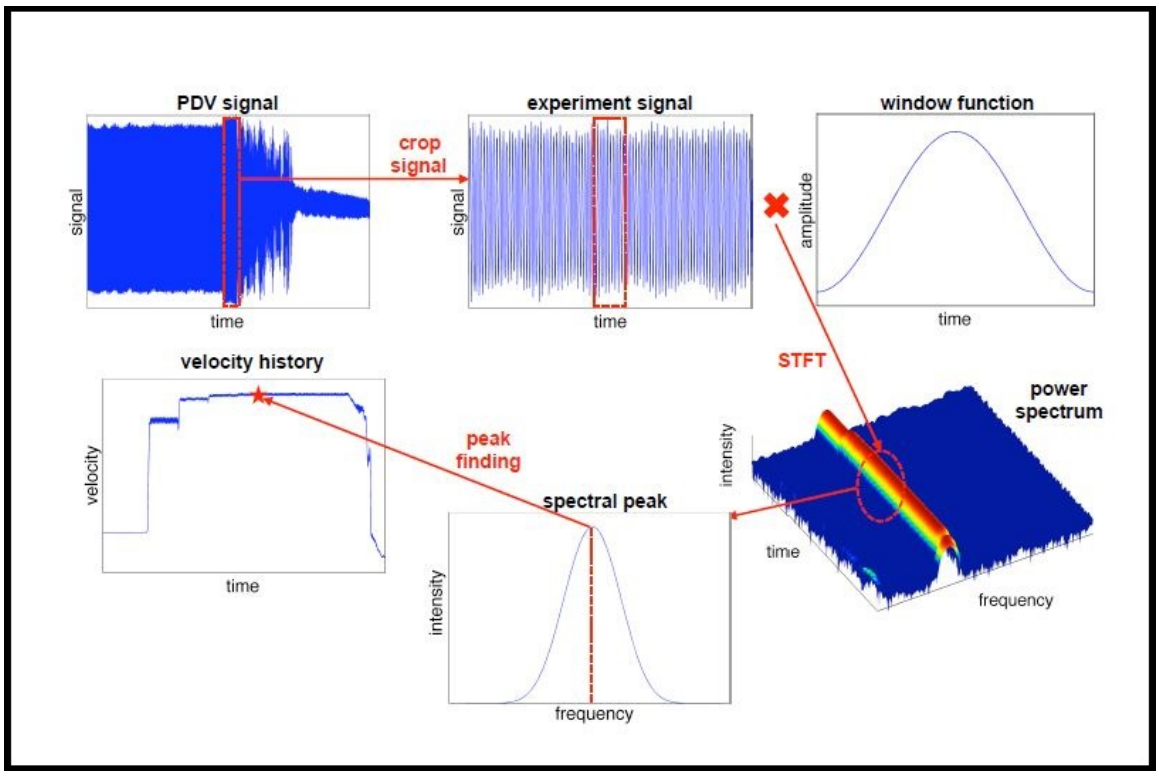

Figure 17. Visual representation of analysis stages in SIRHEN from [5, p. 31]

An outline of the analysis procedures for SIRHEN are shown in Figure 17 [5, p. 30]. The signal is time-cropped to the region of interest and then analyzed with a short-time Fourier transform (STFT) after being multiplied by a window function. The STFT is applied at certain discrete time points to generate a power spectrum of the cropped signal. Then at each time point, the frequency of each spectral peak is found through a peak finding algorithm, which in this thesis is the Gaussian. The peak frequencies are then converted to velocity values to form a velocity history of the experiment.

The SIRHEN program is only two screens: the "Selection Screen" and "Analysis Screen" as shown in Figure 18 below.

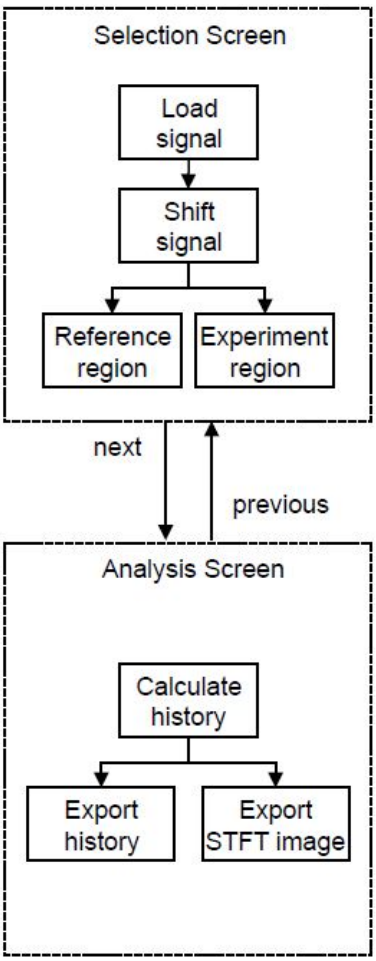

Figure 18. Schematic of analysis stages in SIRHEN from [5, p. 32]

SIRHEN's simple graphical user interface makes it very user-friendly. At the selection screen, the signal data can be loaded and a coarse STFT is performed on the full signal. SIRHEN can only accept a single data file at a time and it must be in either text or binary format. The time region of experimental interest can be selected as well as the reference region for a reference calculation. The "Next" button at the bottom of the "Selection Screen" takes the user to the "Analysis Screen." Then the STFT is performed on the selected experiment region of the signal and its STFT resulting image is displayed. Refinement of the velocity history can also be performed.

From here, the velocity history can be saved as a text file and the STFT image can be saved as a JPEG or PNG file.

3.1.2 pTool and PlotData

PlotData is also a program from Sandia National Laboratories that is used at the HERD [19]. The most updated version is from June 2012. The signal is recorded on Tektronix oscilloscopes and then loaded onto PlotData. From here, the signal is investigated to see if the data recorded is valid for analysis. If the user is unable to accurately select a good experimental region to extract velocity from on the Fast Fourier Transform (FFT), then additional filtering may be required. The frequency band of interest from the signal is recorded in the Fourier domain and a bandpass is applied in PlotData to eliminate noise. The bandpass spans from 0.5 GHz to a maximum of 1 GHz above and below the desired frequencies. This bandpass is the main usage for PlotData and at this point the data is transferred to pTool for further FFT analysis. From here, the velocity can be extracted and saved for further optional analyses, such as pulse duration or particle velocity time history.

pTool version 1.4.9 is being used and is somewhat outdated, with the last update being in August 2008 [3, p. 1]. pTool was developed from the Physics and Analysis Section of NSTec from the Los Alamos Operations. pTool can operate on any PDV signal (raw or filtered) and any part of that PDV signal. It can perform a FFT, Hilbert Transform, and Hilbert-Huang Transform on the signal. The transform used in this thesis was a FFT. pTool allows the user to perform direct extraction of velocities and a velocity graph with error bars as well. The velocity versus time graph can be written to ASCII text files for use in other applications.

pTool is also a stand-alone application, like SIRHEN, but it is written in the Interactive Data Language (IDL). The program was developed and tested on Microsoft

Windows so Mac users may encounter problems using this application. pTool will accept input data in the form of .dig files and ASCII (.txt) files. In either case, the program data will be represented in microseconds and the amplitude in volts. When first opening the program, there will be many options in the top left hand corner of the window screen. The three main sub-menus are *File*, *Filter*, and *Analysis*. The *Filter* menu is quite powerful in this program because it is possible to setup pre-analysis signal filtering before loading the signal.

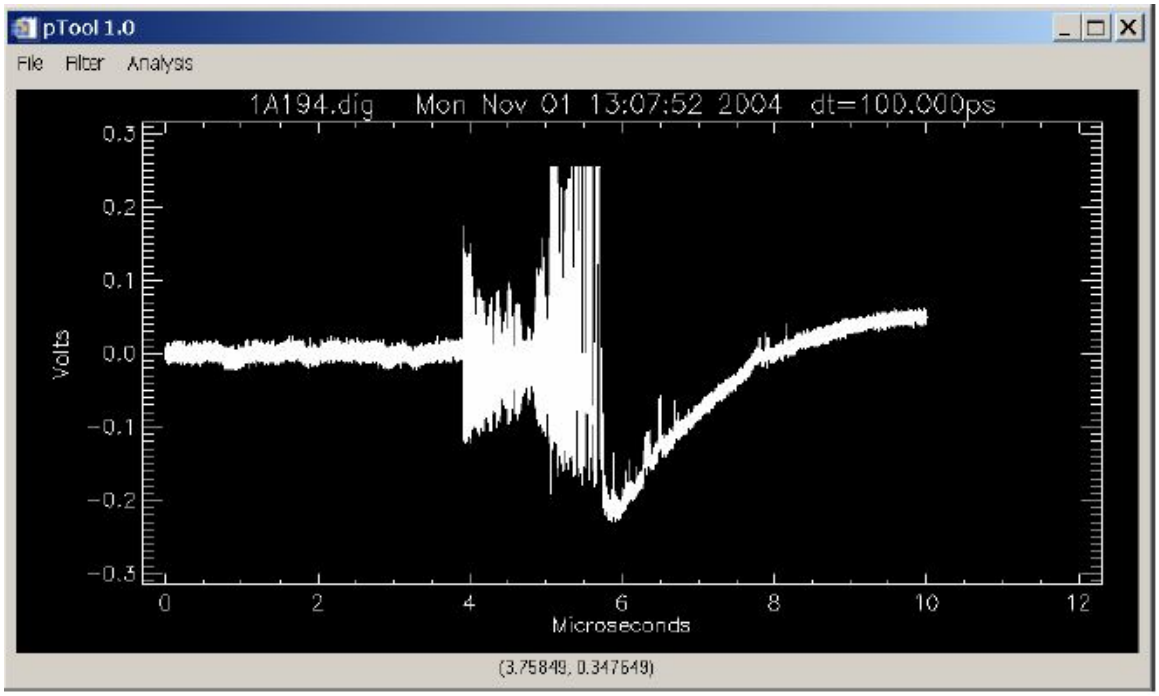

Figure 19. Example of loaded raw signal in pTool [3, p. 3]

Figure 19 shows an example of what a raw signal may look like loaded in pTool. Before the user can continue, pTool requires calibration information about the signal. The laser wavelength must be inputted and the velocity conversion factor, which is 0.99 in this thesis. pTool can do whole datasets as well if there are other similar files in the same file directory. It is also possible to zoom in on the region of interest in the signal before analysis. This feature of zoom is much more user-friendly on pTool

than SIRHEN.

The *Filter* menu is multifaceted in this program [3, p. 5]. A band pass, high pass, or low pass can be applied on the signal among other filters such as a time derivative filter. Then under *Analysis*, a FFT can be performed on the zoomed-in portion of the signal. A dialog box appears that gives the user many variables to adjust but the most important are $WindowSize$ and $Shift$ which are also options for SIRHEN. These two variables determine the number of FFTs performed on the signal and consequently the maximum number of velocity values that can be extracted. Depending on if the user wants time resolution or frequency resolution, window size and shift can be adjusted to tradeoff one variable resolution for the other. These tradeoffs will be explained further in the Results and Discussion section. A limit of pTool is that it cannot display the power spectrum in three dimensions like in SIRHEN, only in two dimensions. Therefore, the FFT/STFT graphs will be presented only in two dimensions. From here velocities can be enclosed and extracted, along with uncertainties. These velocity graphs are presented similarly to SIRHEN velocity graphs along with the uncertainties.

3.2 Lab Setup

This section will present PDV blueprints and pictures of equipment used during this research.

3.2.1 PDV Blueprint/Schematic

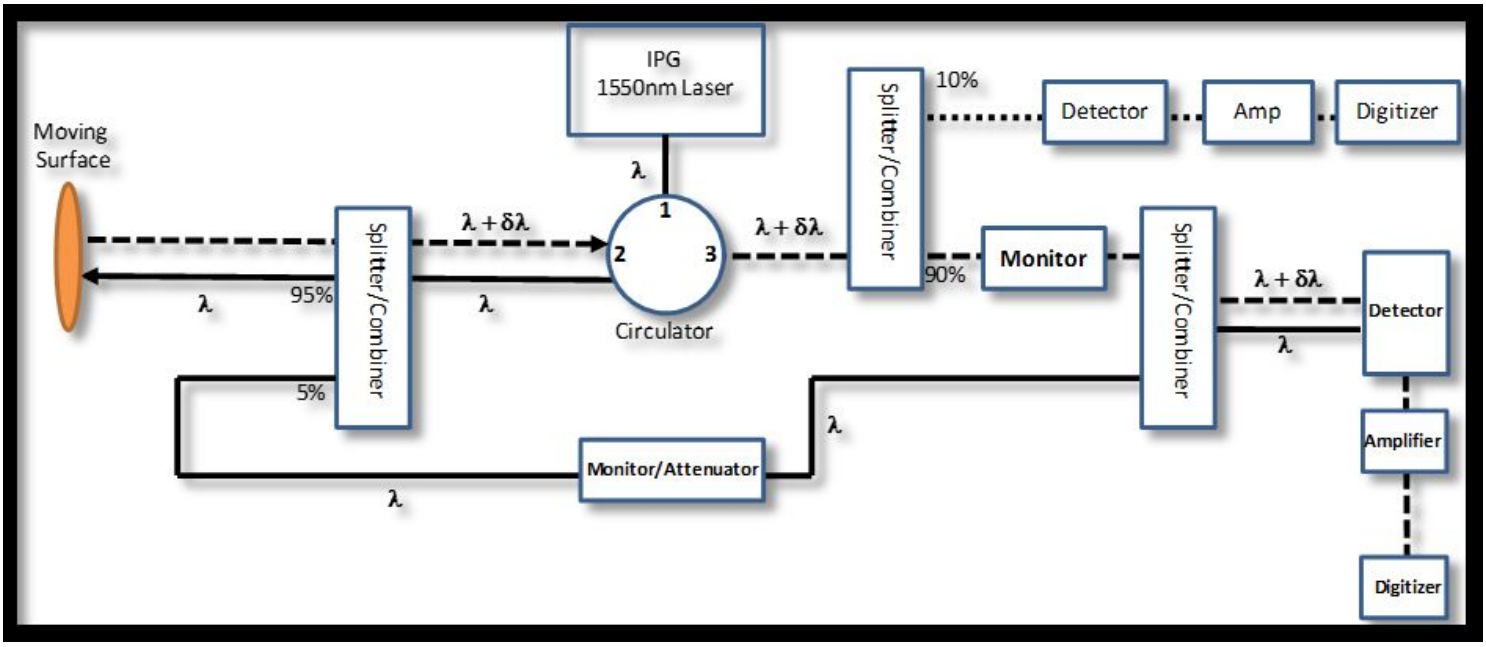

Figure 20. Schematic of PDV system in the Advanced Initiation Sciences (AIS) lab at Eglin AFB

Figure 20 is the most updated schematic of the PDV system used in this thesis since of November 2014. The monitors/attenuators at the bottom of Figure 20 are used to balance all the PDV channels to the optical power level in order to capture all possible data on the digitizer. The PDV injects a laser light of known wavelength into a networked fiber optical system that splits the laser light into two different optical paths: one for the target and one used as the reference leg. When these

signals are recombined, they are transmitted to a photodetector and digitized with an oscilloscope. As the target moves toward the optical probe, the instantaneous motion of photons being reflected off of the target creates multiple Doppler shifts in the detected signal which causes changes in the beat frequency. From this information, the particle velocity of the target can be calculated as:

$$v = \frac{f_b \lambda}{2n} \tag{31}$$

In equation (31), f_b is the beat frequency, λ is the known wavelength, and n is the window correction factor of an optically clear material the laser is transmitted through, which is 0.99 for this thesis.

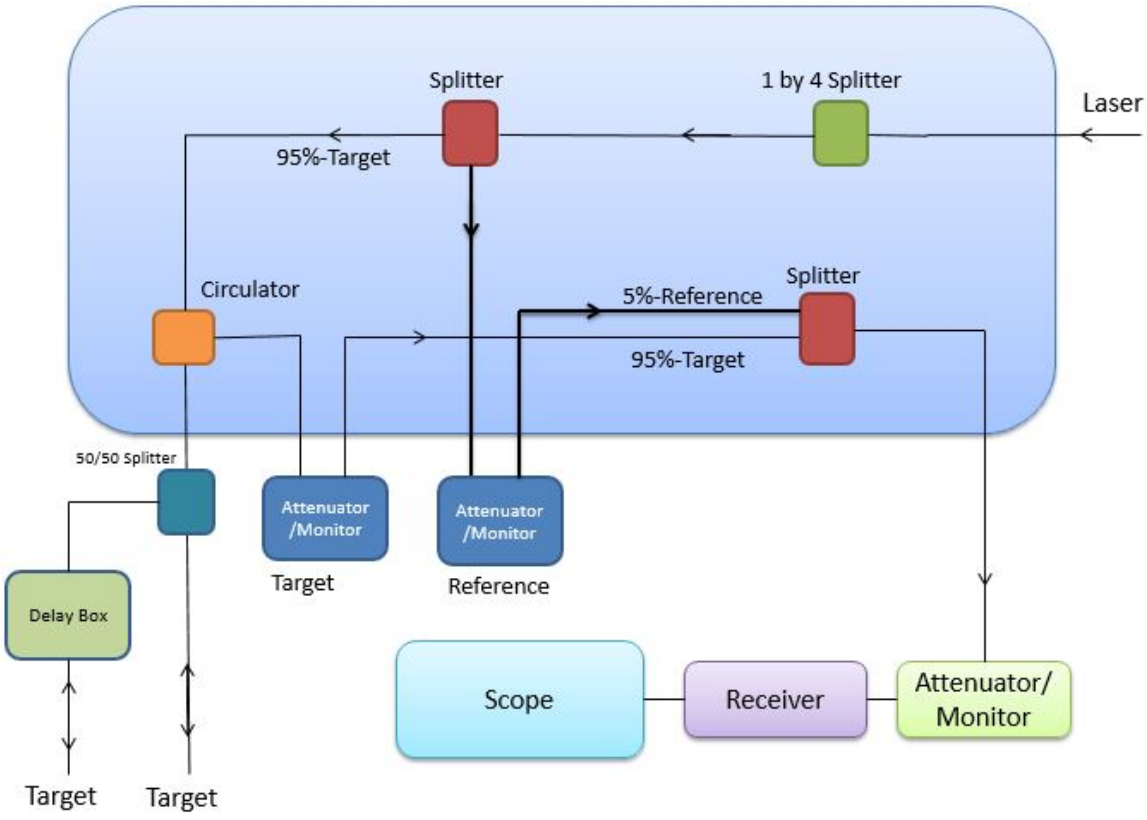

Figure 21. Detailed Schematic of PDV system in the AIS lab at Eglin AFB

There are six main components to a PDV system: the control computer, the laser, the main chassis, variable attenuation monitors, a photodiode optical receiver, and a high speed oscilloscope as shown in Figure 21. The control computer can set the laser settings and store experimental data from the scope. The laser wavelength is 1550 nm and a critical disadvantage of this laser is that it is not visible to the human eye. Therefore, another visible wavelength must be used to align the probe to the moving surface being measured. The main chassis divides the laser energy evenly among four channels by a 1X4 fiber splitter. Each channel has an individual circulator up to 0.5 watts and each circulator has three ports. The laser is connected to port 1, the target is connected to port 2, and the detector is connected to port 3. the source of the non-Doppler shifted and Doppler shifted light comes from the 95/5 splitter out of port 2. Afterwards, it is combined sent through an analog-digital converter and amplified before the raw data is sent to the control computer. The attenuation monitors are used to measure the amount of Doppler shifted and reference light that is being directed to the optical detectors, as well as balance the two signals to optimize the beat frequency. The oscilloscope can record velocities up to 10 km/s and will store beat frequency history on its hard drive, essentially backing up any data.

The hardest part about maintaining the PDV is continually cleaning the fiber optic connectors. If any particles such as dust or lint are within the fiber optic connector, the optic signal will not be complete and the data will be skewed. Lack of maintenance can also lead to misalignment of fiber cores and instability in the laser system. Misalignment can lead to coupling losses from angular misalignment to lateral misalignment. These misalignments are dependent on fiber type, core diameter, and the distribution of optical power among propagating modes.

The splitter in the PDV system utilized during testing was an FC Series 1x4 Compact Fiberoptic Splitter from Agiltron. This splitter is a very important piece

of equipment because it sets the precedent for the rest of the PDV system. If the splitter does not split the power level to 95% for the target and 5% reference, it can skew the rest of the readings for all the instruments involved in the system. A high percentage of light is required to go downstream to the target due to probe losses and returns on the target port. The reference laser percentage is all internal so it does not experience that loss in signal.

The circulator used in the PDV system was a 1310/1550 nm high power optical circulator which minimizes back-reflection and back scattering in the opposite direction of the light's vector. The circulator also connects the target path of the laser to two other ports. One port aims the laser to the target and the other port sends the reflected laser from the target to the attenuator/monitor. Looking closely at the circulator in Figure 21, the first port is where the target's 95 light percentage is sent after the 95/5 splitter. The third port on the bottom is where the target laser exits and returns back through the same fiber after reflecting off the moving target. The Doppler-shifted target laser is then sent to the second port on the right where an attenuator receives the Doppler-shifted laser.

The power monitors in Figure 21 display the power level being received in units of decibel-meters (dBm). This instrument ensures that the splitter is splitting the laser in the intended ratio, as well as ensuring the power levels of the reference light and the Doppler-shifted light are balanced before recombining. There is one monitor for the target, one for the reference, and finally one another monitor right before the optical receiver after the split-paths recombine. The power monitors for the target and reference light are EigenLight's Series 400 Power Monitor-Attenuators (PMAs). The power monitor after the lasers recombine is an EigenLight Series 500 PMA. Both models of power monitors have the same attenuation range of 40 decibels (dB) and the same attenuation resolution of 0.1 dB. All of the power monitors in the

schematic should be reading between -15 to 22 dBm when completely unattenuated. The power monitors do not have to be the same value due to losses in power from fiber misalignment and lack of perfect cleanliness.

The measurement instrument of the PDV system is located within the optic receiver as a photodiode responder. After the lasers recombine, an interference is created due to the differences in frequency between the two sets of light. This light interference is known as a fringe shift, or "beat frequency", and the photodiode responder samples this fringe shift to digitize the signal in the oscilloscope. The lasers recombine at a second splitter named a coupler as shown in Figure 21. This coupler is identical to the first splitter but it is installed backwards. After the recombined light passes through the final power monitor, the light is sent to the optic receiver which measures the power from the recombined light and outputs the result in volts via the oscilloscope. The model number for the optic receiver is SCMR-100K20G by MITEQ, Inc. This piece of equipment is vital to determining the sampling rate of the PDV system. The higher the sampling rate is for the optic receiver, the lower the velocity uncertainty and frequency uncertainty will be for the Fourier transformed signal because of the higher amount of captured frequency points from the photodiode. The bandwidth sampling rate for the optic receiver is 100 kilohertz (kHz) to 20 gigahertz (GHz). In this thesis, the max sampling rate of 20 GHz was used because the oscilloscope also had a max sampling rate of 20 GHz which resulted in incredible signal resolution. The oscilloscope used during testing was a 50 GS/s Scope by Tektronix.

Once all connections have been made in the PDV, a "thumper check" must be done. Essentially, an optical mirror is connected to every port and the laser is on low power. This configuration of the laser allows the certified user to adjust the laser power for optimum performance. The signal return should be between -15 to 22

dBm on the monitors. Lastly, line checks and trigger checks are performed as well to make sure the complete optical signal is being received without delay. Safety is the number one priority as always in a laboratory. Laser safety glasses and warning lights must be in place before use. Only laser certified users should operate the PDV. High voltage is a safety hazard as well. The experiment requires high voltage to generate an electrical breakdown in the chip's bridge. This breakdown generates a plasma which then shears the top layer of the chip and accelerates the flyer at the PDV probe. This experiment should be operated in pairs just in case one of the certified users requires CPR.

3.2.2 Chip Slapper Experimental Setup

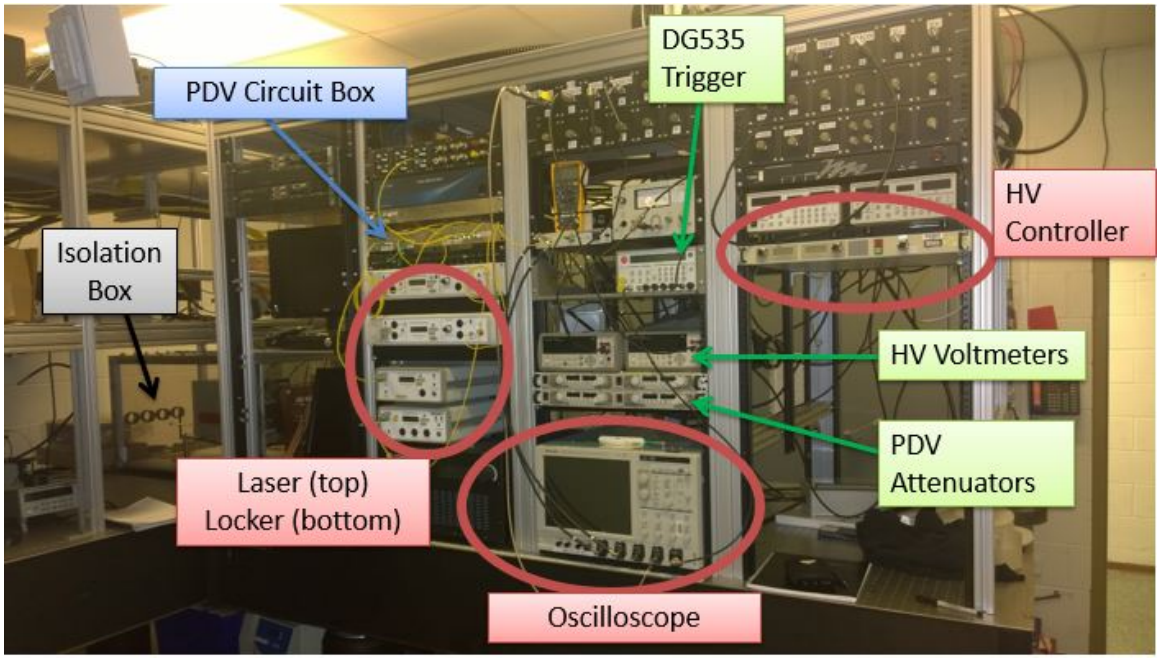

Figure 22. Essential equipment used in the AIS lab

The PDV circuit box in Figure 22 is the main control for operating the laser. The laser can be turned on and the power level as well can be adjusted here. The

isolation box is where the actual chip slapper experimentation occurs. The box is there to protect any persons within the lab in case anything goes wrong. It also has sensors which tells the users if any access doors are open and will not allow the users to continue hazardous operations if that happens.

The laser lockbox is used to upshift the PDV system but it was not used for this experiment. Only the certified technician can unlock the lockbox to operate the laser, else it will not turn on. The oscilloscope shows the digitized signal data. The PDV attenuaters balance the energy from the laser among the 4 channels for optimal optical signal.

The high voltage voltmeters show the voltage that is feeding into the PDV from the fireset during the experiment as well as the amount of voltage sent into the chip to cause it to discharge and collide with the plastic circular slab. The high voltage controller can determine how much energy is fed into the PDV and the chip. The DG535 trigger controls when the high voltage is released into the isolation box. The actual target laser wavelength during testing was 1550.12 nm and the reference laser wavelength was 1550.13 nm which attributes to uncertainty in data reduction and analysis.

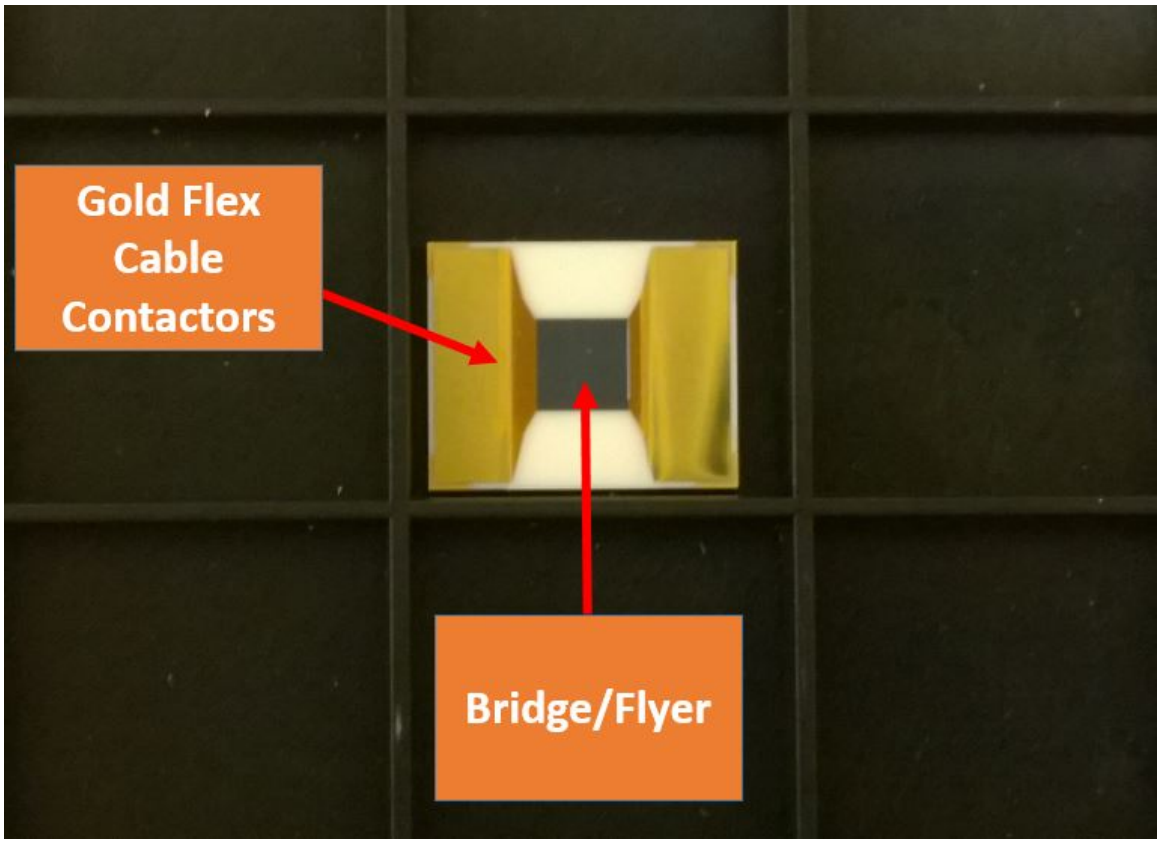

Figure 23. Actual chip used in the AIS lab

The chips, also known as flyers, can vary in thickness but all are made from the same material and chemical composition of Parylene C as shown in Figure 23. The PDV measures the velocity of these chips, or flyers, because the chips are the target in this experiment. The bridge or flyer itself is the only object colliding with the plastic slab, not the golden parts of the item. The gold flex cable contactors seen are to pass the high voltage to the chip to cause a massive discharge. Each chip used in the experiments was labeled wafer number W76 which corresponds to specific dimensions of the chip. Each chip was 0.4 inches wide by 0.5 inches long with a thickness of 50.09 microns. The chip was constructed out of Parylene C which is a special polymer.

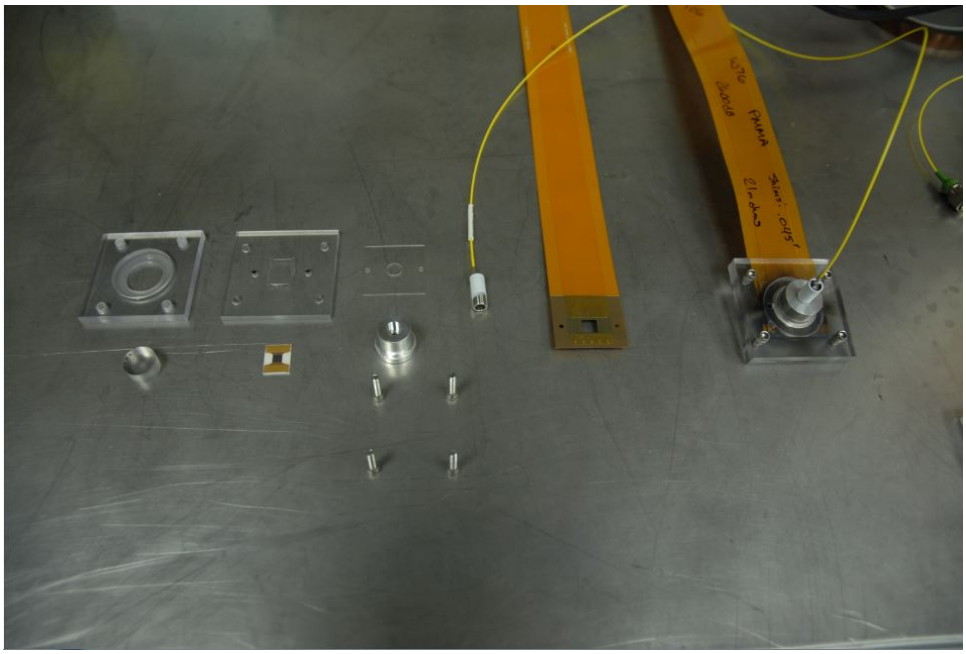

Figure 24. Chip Slapper setup used in the AIS lab

Figure 24 represents the chip slapper setup unassembled. The two square cases to the left are what contain the collision between the chip and circular plastic slab, which are below these two square cases. The circular slab is 0.5 inches in diameter and is made out of PMMA. There is another thinner plastic square (PMMA window) which is covered over the fiber optic cable to protect it from getting damaged and keep out residue particles from the collision. The fiber optic cable itself is screwed in the aluminum funneled cap to keep the fiber optic cable, and thus the laser, aligned against the flyer. The long brown strip is the flex connector cable itself that is connected directly to the 10 kilovolt (kV) fireset. The flex cable part number and revision used in these experiments was RSI-1129RevB. The fully assembled experiment setup is shown all the way to the right in Figure 24.

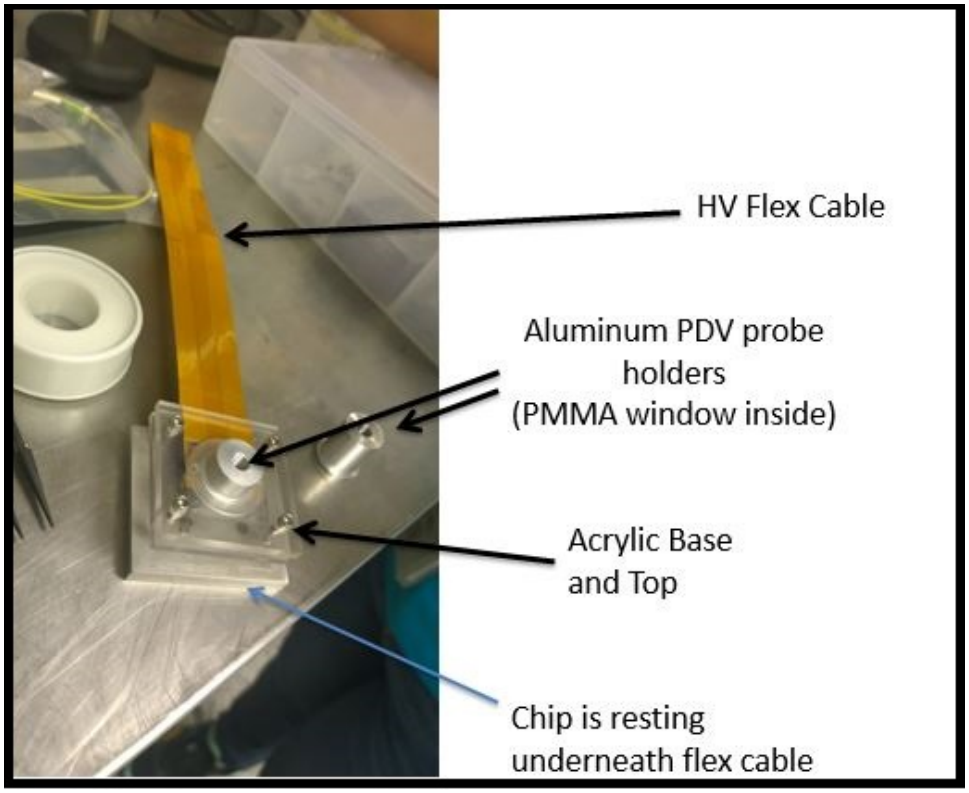

Figure 25. Chip Slapper setup assembled

A closer view of the assembled chip slapper experiment is presented in Figure 25. Note both the base and top are acrylic in order to withstand the high velocity at which the chip is moving at. The chip and the PMMA window are 0.045 inches apart when fully assembled. The chip must travel this distance before impacting with the window.

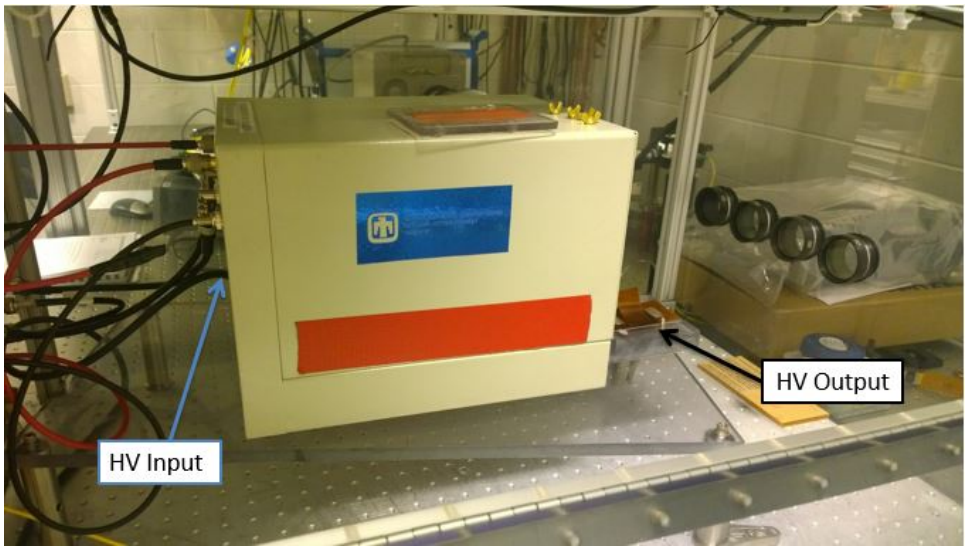

Figure 26. The 10 kV capacitor that delivers the high voltage to the PDV and flex connector

The Figure 26 is the 10 kV fireset inside the isolation box that delivers a jolt of high voltage to the chip slapper experiment through the flex connector cable. The model number for the fireset is LLNL SN2. This 10 kV fireset is a very dangerous piece of equipment to operate and should be handled with caution.

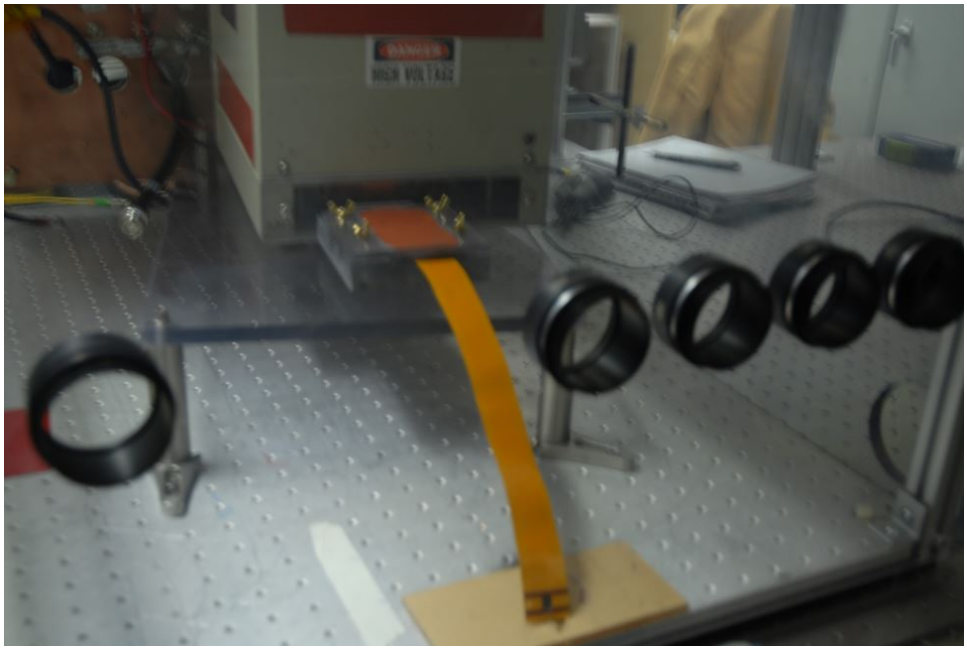

Figure 27. The chip slapper experiment connected to the 10 kV capacitor in the isolation box

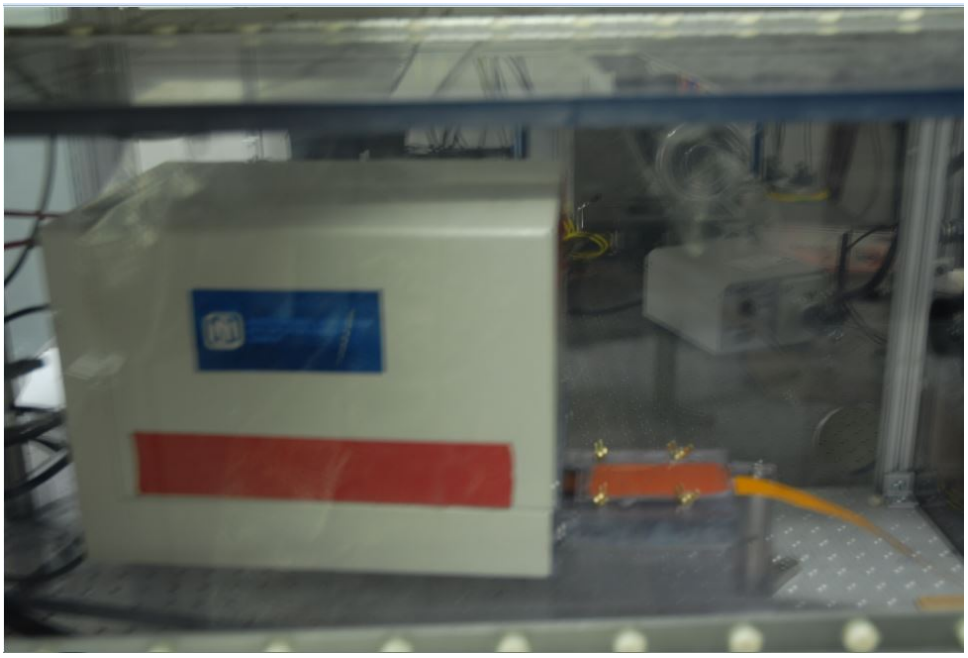

Figure 28. The chip slapper experiment connected to the 10 kV capacitor in the isolation box

Figures 27 and 28 present the complete setup at different angles (the chip slapper setup connected to the 10 kV fireset inside the isolation box) right before firing the high voltage fireset.

Figure 29. Example results of chip slapper experiment

Figure 29 exhibits the plastic slab after the chip collides with it at an incredible velocity. The imprint the chip leaves is impressive given the relative thickness of the plastic slab to the flyer. Sometimes the backside of the plastic slab is damaged as well from the force of the shock traveling through the material. The chip itself usually fragments, and if the plastic slab is placed under a microscope, fragments from the chip can be seen embedded in the circular slab.

IV. Data Results and Discussion

Table 3 represents important equipment readings during all the chip slapper experiments conducted at Eglin Air Force Base. Table 3 contains the actual cap voltage data that each chip was charged with before jolting off the bridge and colliding with the plastic PMMA cylinder window slab. The actual cap voltage was how the chip's velocity was controlled. Varying the cap voltage would vary the chip's velocity. The higher the cap voltage, the higher the chip's velocity. The target/reference power ratio is also included in the table and it represents the ratio between the target wavelength power and the reference wavelength power. A general pattern in this ratio is that as the voltage increases, the ratio increases which makes it difficult to separate noise from actual meaningful lab signal data which can attribute to error. However, the tradeoff is as the voltage increases, the faster the chip collides with the slab. For those chip shots with higher target/reference power ratio, band passes and band stops were applied in PlotData to reduce the amount of noise. Shot classification numbers in both figures are simply a methodical way to organize the shots in the AIS laboratory.

Table 3. Chart of equipment readings during testing

Shot Classification	Actual Cap Voltage (volts)	Target/Reference Power Ratio
EG-I0119	4511	0.3906
EG-I0120	4510	0.4303
EG-I0121	4757	0.1883
EG-I0122	4511	1.7012
EG-I0123	7996	1.2495
EG-I0124	8093	2.0126
EG-I0125	6035	0.5032
EG-I0126	6048	2.7024

All chip slapper experiments were captured by the photodiode responder in the optical receiver at a sampling rate of 20 GHz and digitized on the oscilloscope at a sampling rate of 20 GHz. Figures 30 and 31 are the results of the first chip slapper experiment. Figure 30 is the untransformed signal from the oscilloscope in the lab. Figure 31 is the result of performing a STFT/FFT on the raw signal. The window type method used was the Hamming method. The Hamming method was applied with a 1024 window size and 512 frequency points with an overlap ratio of 2 for all chip slapper shots. This large window size and frequency point shift was best for frequency resolution. A larger window size is best for frequency resolution but horrible for temporal resolution. A narrow window size is best for temporal resolution but results in poor frequency resolution. The window size can be adjusted depending on the phenomenon being studied, which in this case is the frequency resolution. Both pictures in this figure are zoomed in on the experimental region of the signal in order to better view shock Hugoniots.

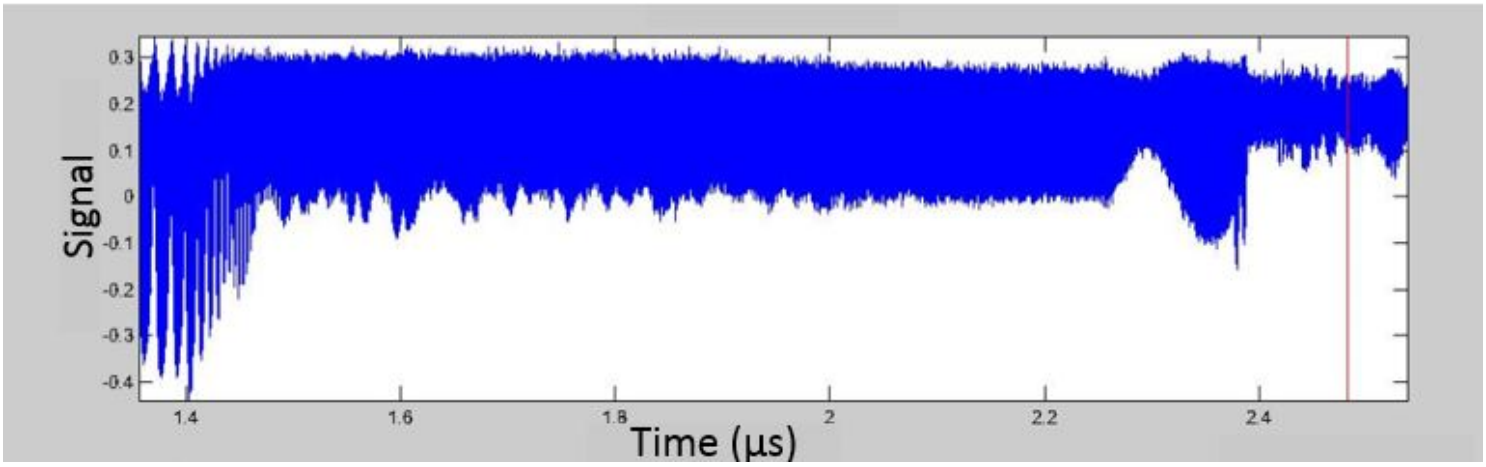

Figure 30. Digitized signal of EG-I0119 in SIRHEN

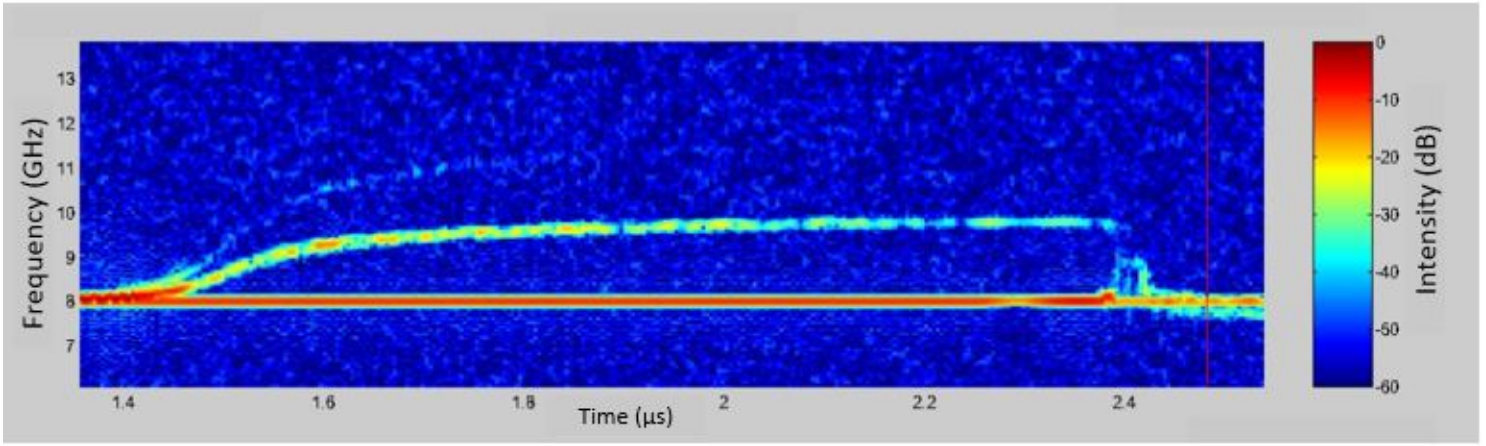

Figure 31. STFT signal of EG-I0119 in SIRHEN

In Figure 31, the blue background represents natural noise from the lab. The multicolored curve in this picture represents the target's reflected frequency as it approaches the PMMA slab. The target's acceleration can be noted by the increasing frequency in the curve. The different coloration between the target's frequency curve and the background noise is from the difference in intensity of sound pressures. The bright red line below the curve represents the target's frequency at a stationary position as it is still connected to the bridge. The x-axis is time, measured in microseconds, and the y-axis is frequency, measured in Hz. The magnitude of the y-axis changes throughout the data reduction process. There will be projections of lower intensity stemming from the target's frequency curve, as it can be slightly seen in the lower picture of Figure 30. Intensity represents the abundance of that specific frequency during the experiment, whose axis is on the right side of the STFT graph. These projections are due to the multichannel sensitivity inherent in the PDV system. The actual measurement of the chip's frequency can be recognized by the stationary frequency with the higher intensity which is the bright red line at under the curve. After the chip, or flyer, discharges from the bridge to collide with the PMMA slab,

two shocks are instantly produced. These shocks are observed in the final microseconds of each target's frequency curve and this phenomenon can be better observed in Figure 32. There seems to be an additional smaller curve produced after the chip collides with the PMMA slab and begins to slow down. This smaller curve is located at the end of the STFT signal, before rarefactions appear. This smaller curve is the production of two shocks from the chip's collision which is incredible to capture due to the speed this event occurs. At impact, The PDV system is measuring the reflected laser that was shifted from the shock vibrations that are moving through the slab from impact, as well as rarefactions moving through the slab. The deceleration and collision of the chip against the slab all occur in about 1 nanosecond.

The chip's peak frequency can be better seen after signal extraction in the Figure 33. The peak frequency is synonymous with the chip's peak velocity for these experiments. The signal extraction was performed through a dynamic limit of 1×10^8 Hz to extract data from the target's frequency curve with minimal noise. This dynamic limit is essentially a bandpass for SIRHEN. The chip's peak velocity is slightly just before collision. The peak velocities in this thesis lied between 1500 m/s to 4000 m/s which was dependent on the actual cap voltage. The first instance of deceleration, or decrease in frequency, is due to the compression of air that slows the chip before impacting the slab. Then there is a slight plateau, which is the actual collision of the flyer against the PMMA window slab which causes the production of two shocks. One shock travels through the flyer itself and the other shock travels through the circular slab, which is the shock the PDV system measures. At the shock, pressure decreases because the shock wave moves from high-impedance material to low-impedance material. The deceleration occurs so quickly at the end of the event the target's frequency curve becomes discontinuous during the sampling of the shot signal, even at 20 GHz sampling rate. After the collision, rarefactions can be seen in subsequent time due

to slight oscillations in the PDV measurement, as the rarefactions decompress the PMMA slab back down to its natural pressure.

This pattern of target acceleration, deceleration, shock plateau, and shock production will be seen in all of the proceeding figures for the chip slapper shots. The velocity extraction and Hamming method all also were performed in similar fashion. Also, every true measurement in every shot can be recognized with the 8 GHz target's natural reflected beat frequency.

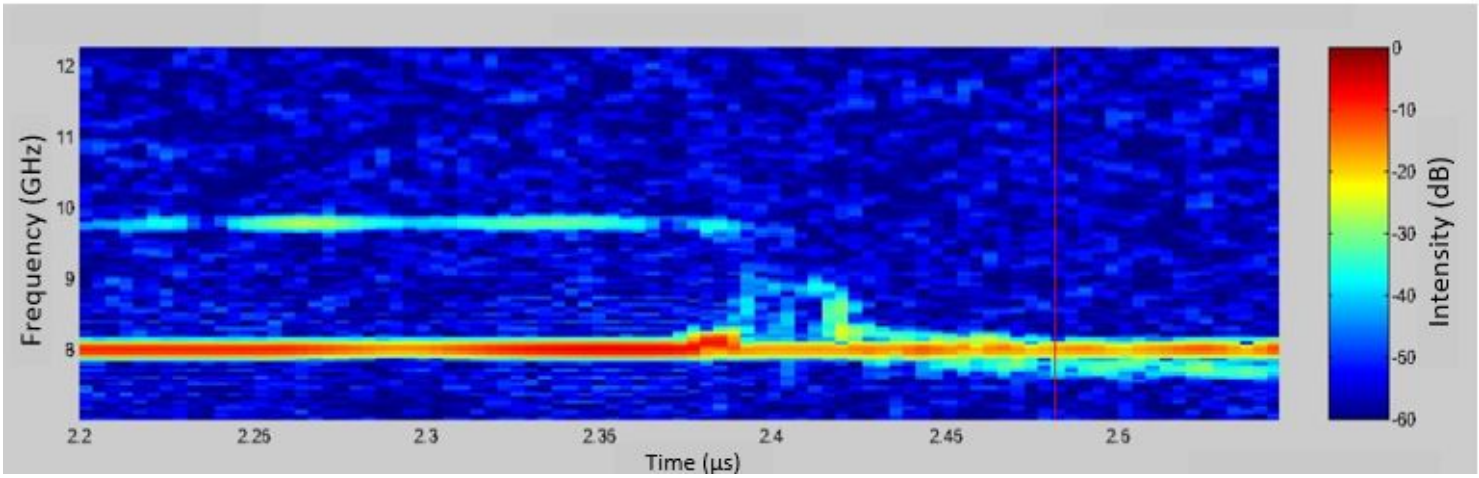

Figure 32. STFT signal of EG-I0119 zoomed in on shock in SIRHEN

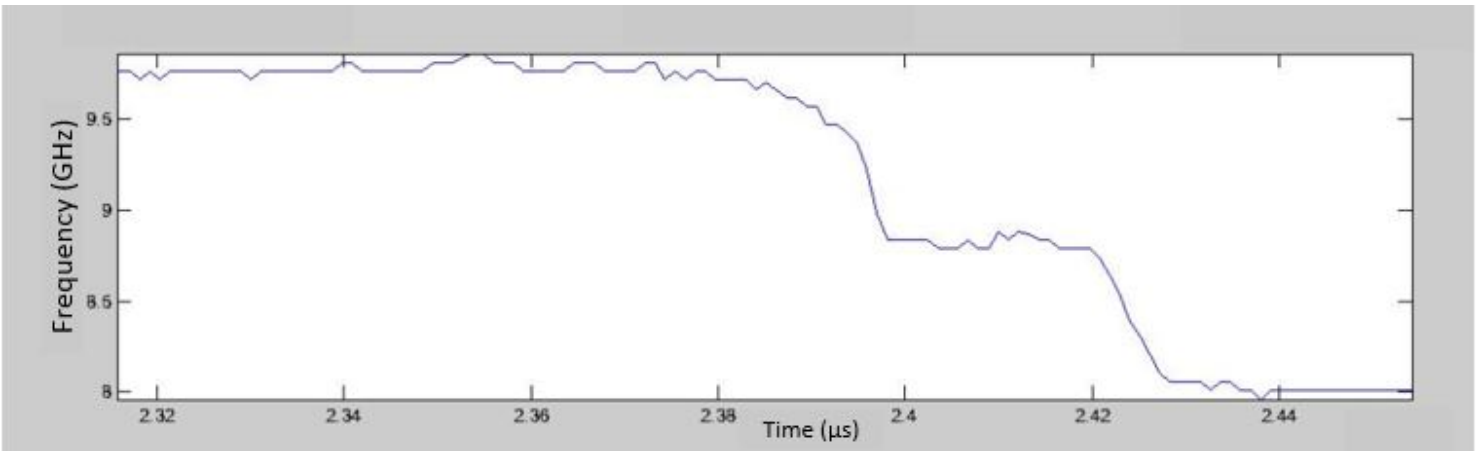

Figure 33. Extracted signal of EG-I0119 zoomed on on shock in SIRHEN

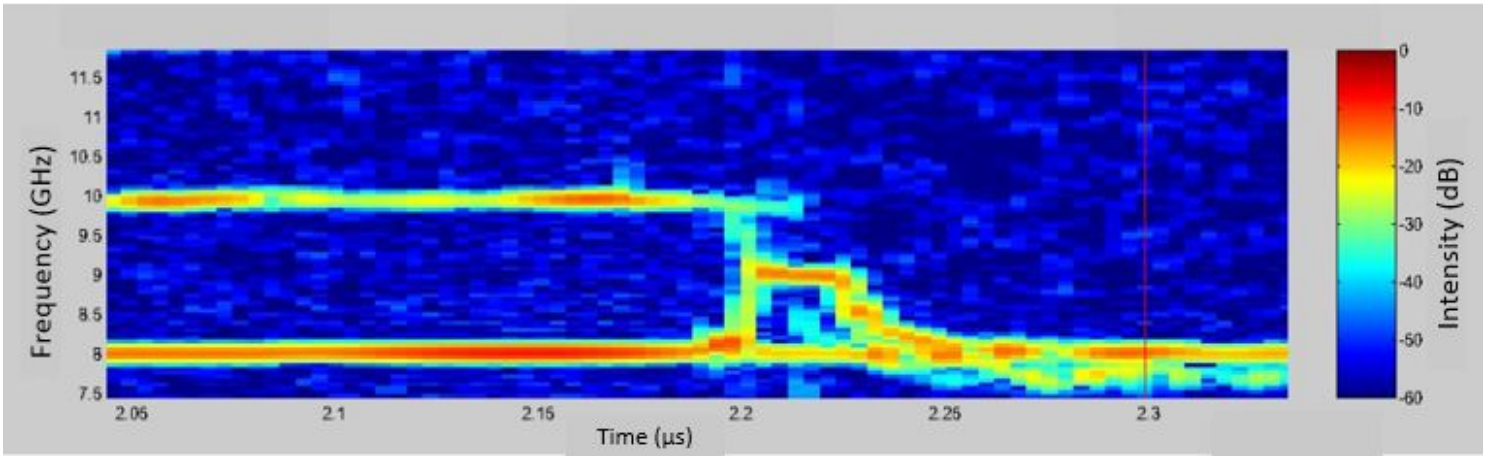

Figure 34. STFT signal of EG-I0120 in SIRHEN

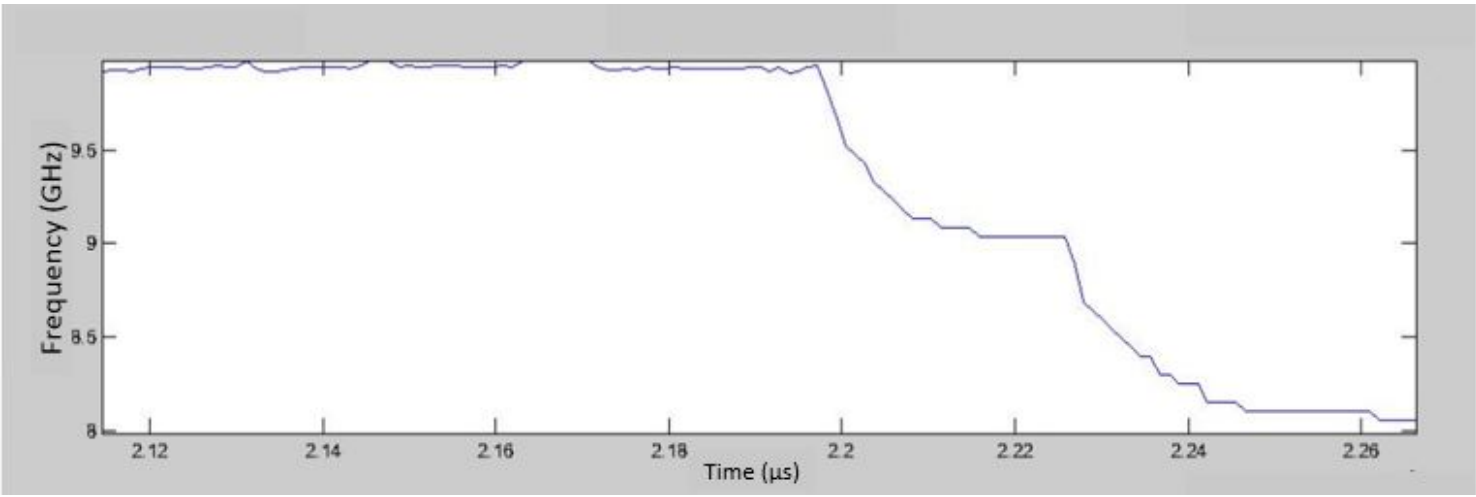

Figure 35. Extracted signal of EG-I0120 in SIRHEN

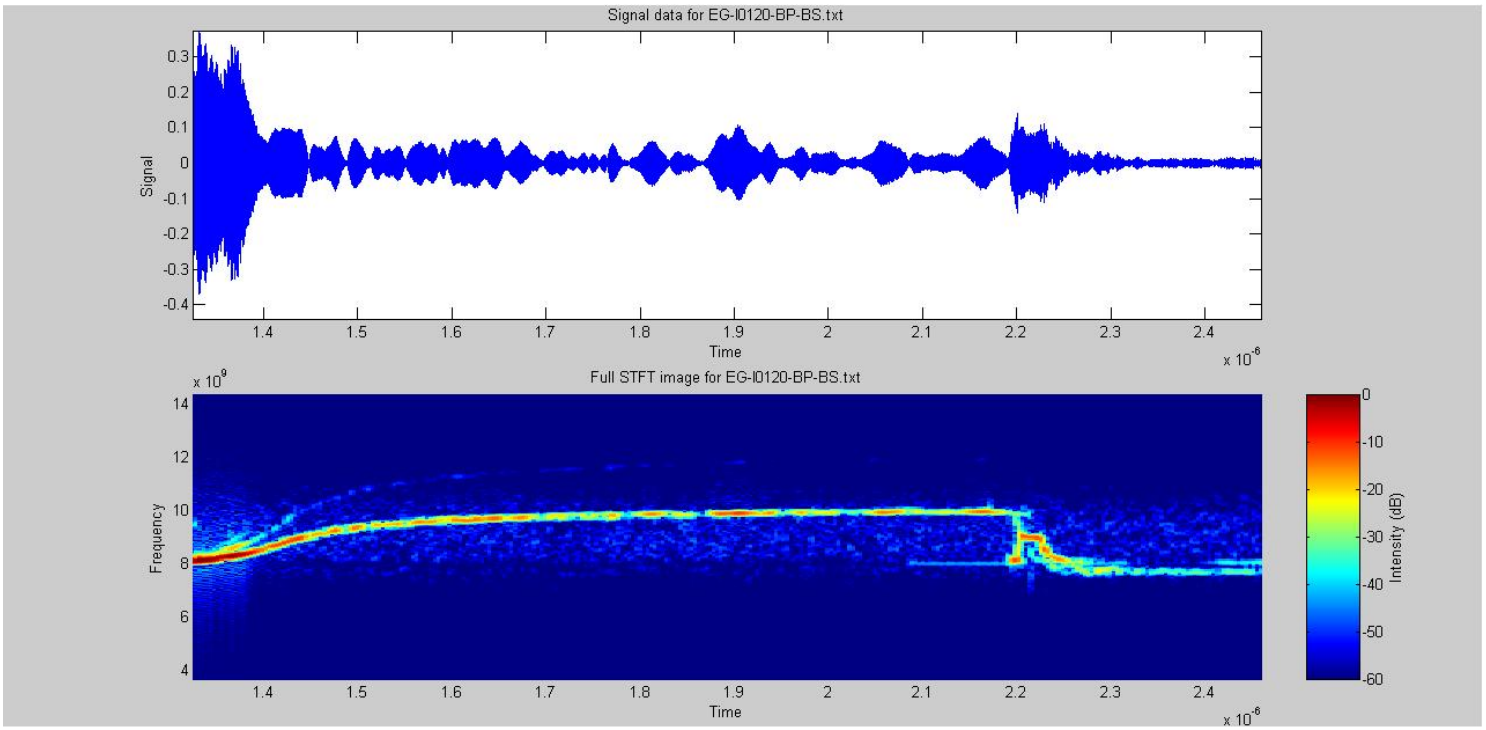

Figure 36. Filtered signal of EG-I0120 with a band pass and band stop by PlotData displayed in SIRHEN

Figures 34 and 35 represent the data captured from the second shot. In Figure 34, the shock plateau can be seen much clearer as well the deceleration of the target itself near the 2.2×10^{-9} second mark. After the collision, deceleration still continues after the shock plateau because the back end of the flyer is still accelerating towards the slab and compressing within itself until the shock produced by the original collision completely reaches the open end of the chip, as described earlier in the Background chapter of this thesis. In Figure 35, the excellent resolution in the STFT signal led to good extraction of the peak velocity and shock plateau extraction. The extraction of this shock plateau is important in this thesis because it signifies the beginning of shock production from solid-solid collisions. The strength and speed of the shock

wave can be deduced from the extraction of the shock plateau.

Figure 36 is the raw data of the second shot with a bandpass and bandstop applied to it. This set of raw data is different from the pictures before because there is no longer a projection of the event as well as significantly reduced noise. Also, the raw signal itself is no longer shifted but centered around the zero axis due to the bandpass. The bandstop has eliminated almost all of the noise in this case. Although PlotData does a wonderful job of eliminating extraneous noise, it can also lead to loss of important data. The bandpass and the bandstop do not change the peak velocity or peak frequency of the data. SIRHEN had trouble dealing with this sort of data which will be explained later in this chapter.

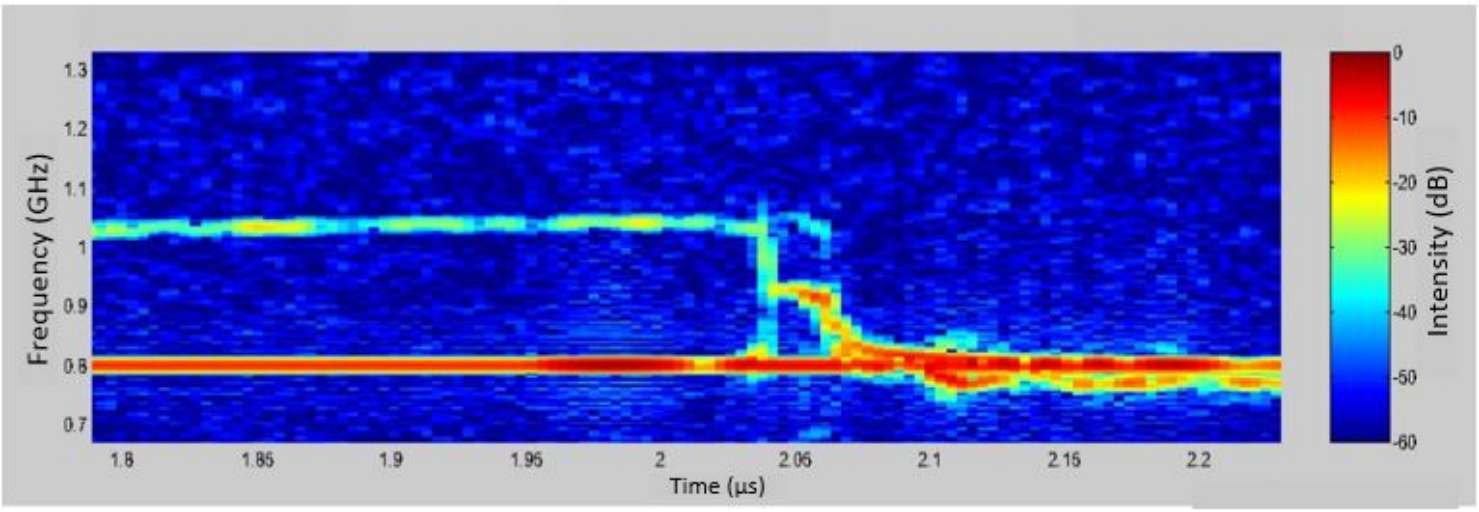

Figure 37. STFT signal of EG-I0121 in SIRHEN

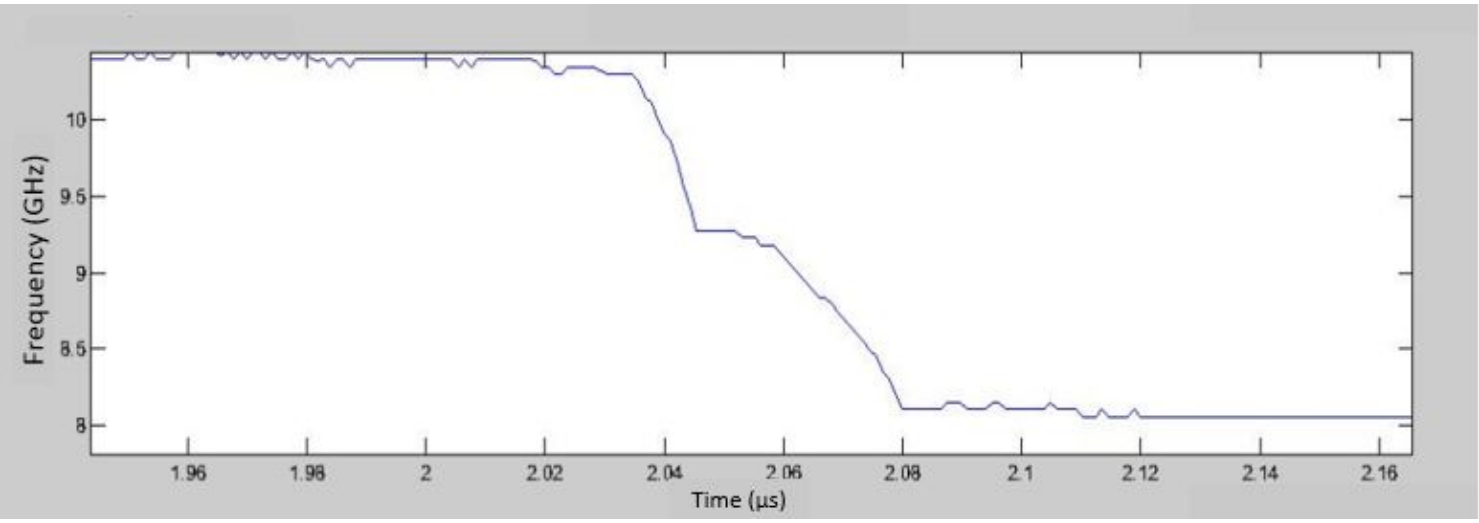

Figure 38. Extracted signal of EG-I0121 in SIRHEN

The third shot is represented in Figures 37 and 38. This shot had a much larger voltage potential than the previous shots, as seen in the greater intensity during collision in Figure 37. Also, the deceleration is much higher in this case due to the greater acceleration. The shock plateau in Figure 37 is much sharper than the shots before it due to this greater deceleration. Also, the oscillations are much greater during the decompression phase of the experiment in Figure 37. The peak velocity in this case is much greater than the two previous shots as well and the shock plateau happens about a 0.1 nanosecond earlier than the two previous shots, as shown in Figure 38.

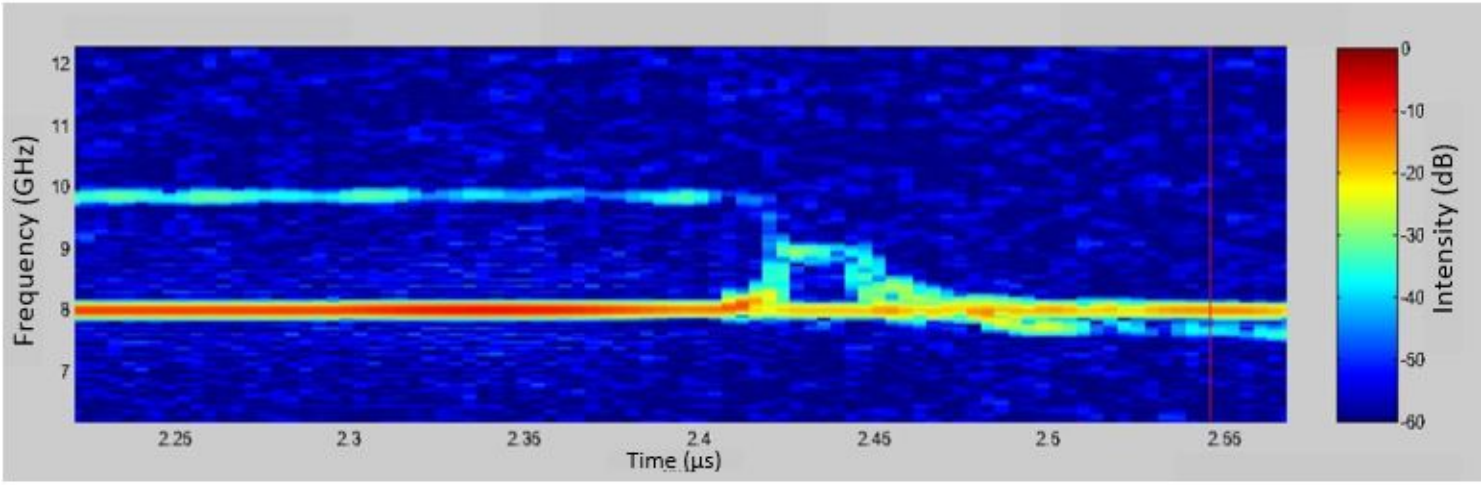

Figure 39. STFT signal of EG-I0122 in SIRHEN

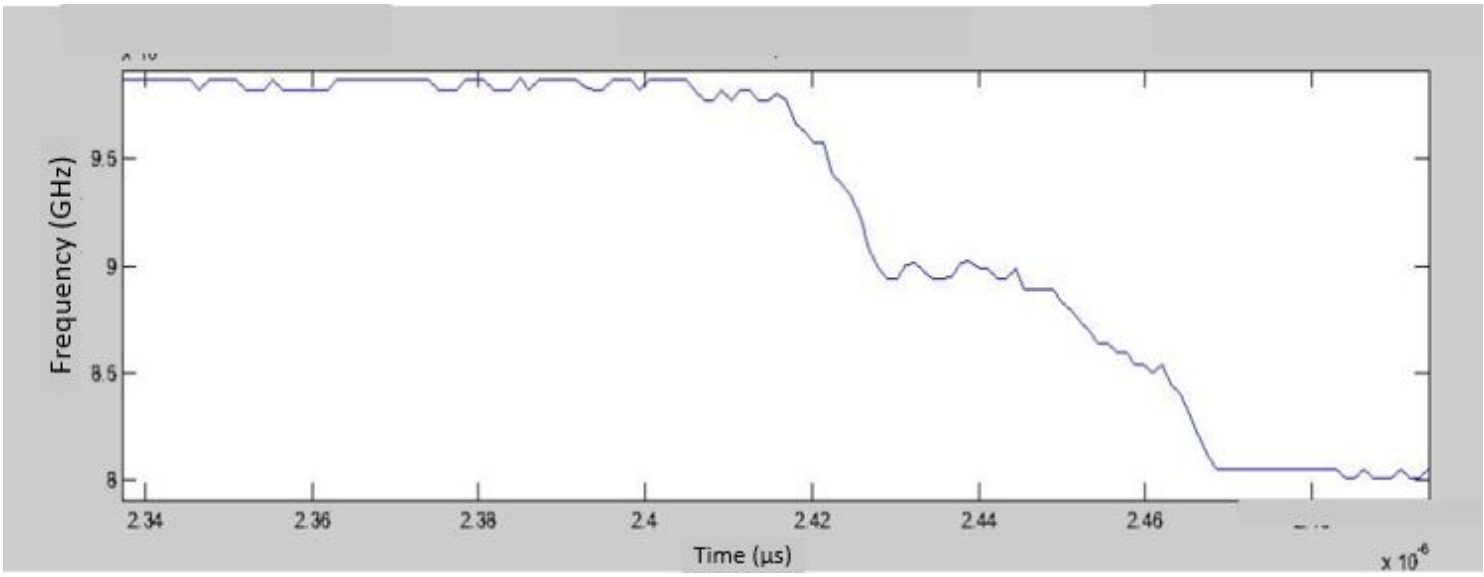

Figure 40. Extracted signal of EG-I0122 in SIRHEN

Figures 39 and 40 are a series of data plots for the fourth shot. The shock plataeu is acceptable in Figure 39, with an intensity at collision of about -30 dB. The rapid acceleration causes much noise in this case which makes it difficult to extract the

peak frequency or velocity, as depicted by Figure 40. The larger the voltage, the faster the flyer impacts the PMMA window, and the greater the noise fraction is but this increase in noise fraction is minimal. Noise fraction is the ratio between true signal and background noise, and it is represented in percentage.

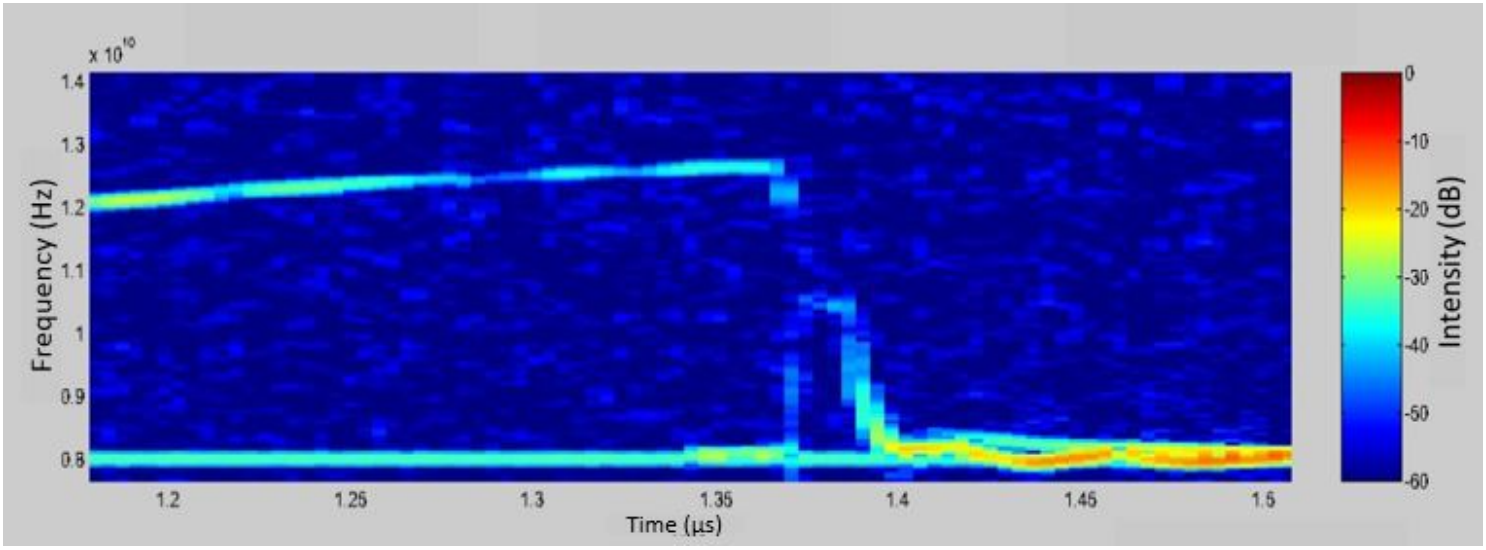

Figure 41. STFT signal of EG-I0123 in SIRHEN

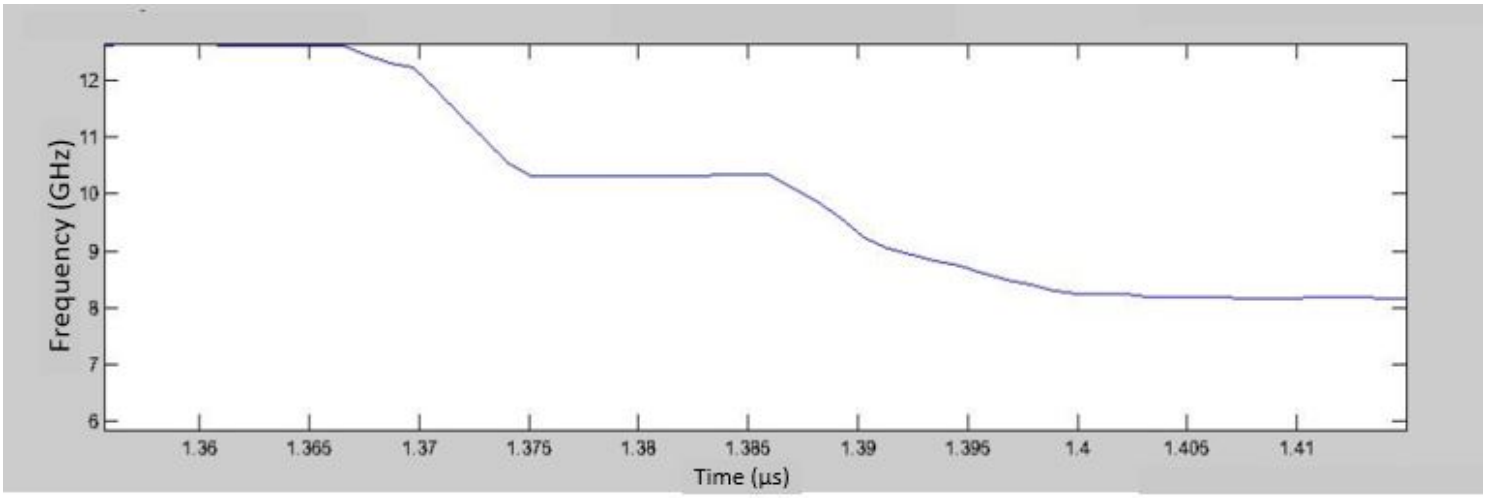

Figure 42. Extracted signal of EG-I0123 in SIRHEN

The data in Figures 41 and 42 is of lower intensity when compared to the previous sets of data. In Figure 41, there is a discontinuity in the initial deceleration of the flyer, as well as in the collision with the slab, yet the oscillations afterwards are quite small compared to the rest of visualized data. It was quite difficult to apply a dynamic limit to such a low-intensity signal, as shown in Figure 42. The shock plateau itself is much longer in Figure 42 than in most data sets, resulting in a much longer impact time against the PMMA window due to the chip's relatively high peak velocity.

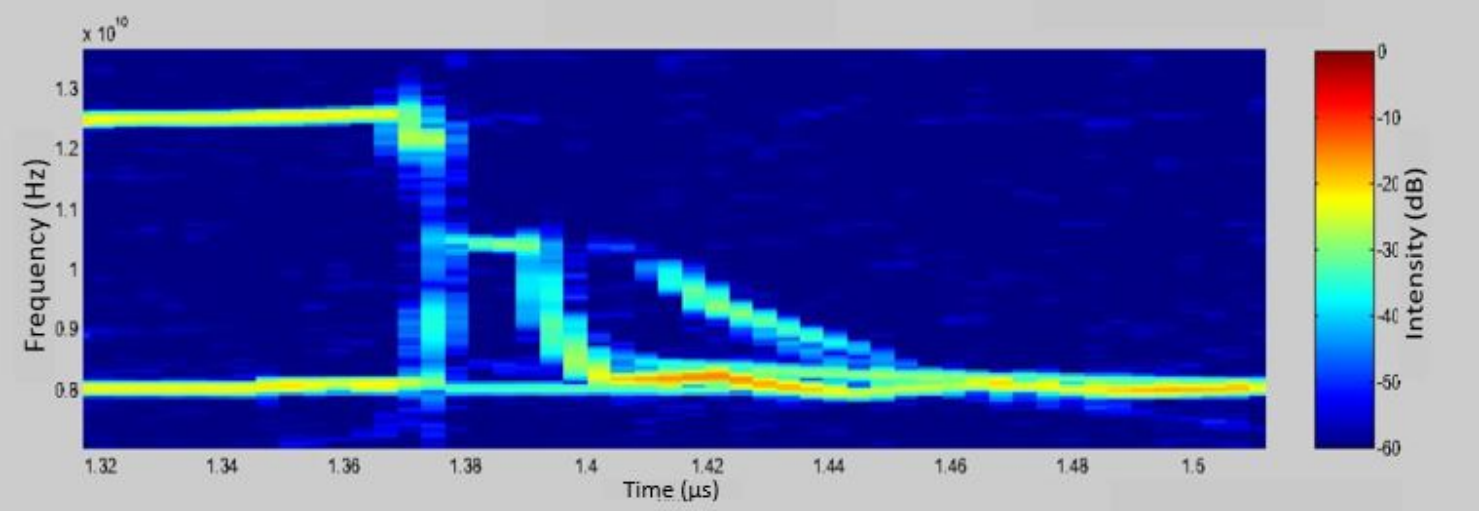

Figure 43. STFT signal of EG-I0124 in SIRHEN

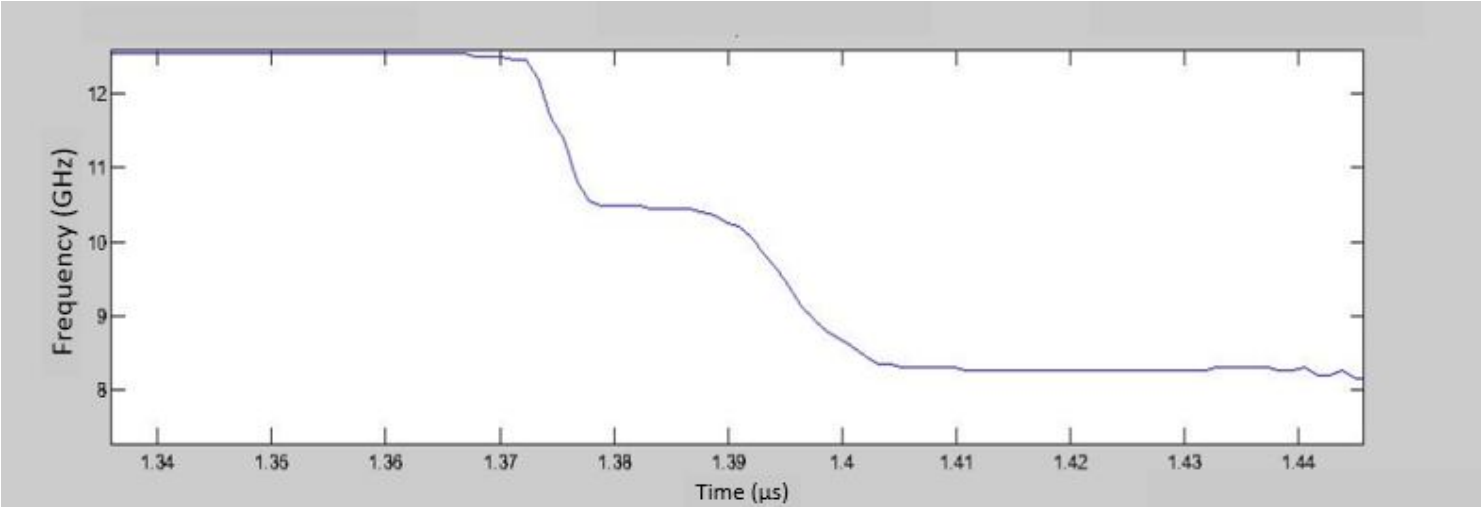

Figure 44. Extracted signal of EG-I0124 in SIRHEN

The set of data in Figures 43 and 44 is slightly stronger than the previous shot. The discontinuities occur mainly during deceleration and the shock production after collision, as shown in Figure 43. The shock plateau was captured by the PDV system, regardless of the low-intensity of the frequency, but the deceleration of the chip was barely recorded. The sampling of the chip's deceleration is important because this deceleration influences the timing of shock production from solid-solid collisions. As the magnitude of the chip's deceleration increases, the strength and speed of the produced shock from collision also increase.

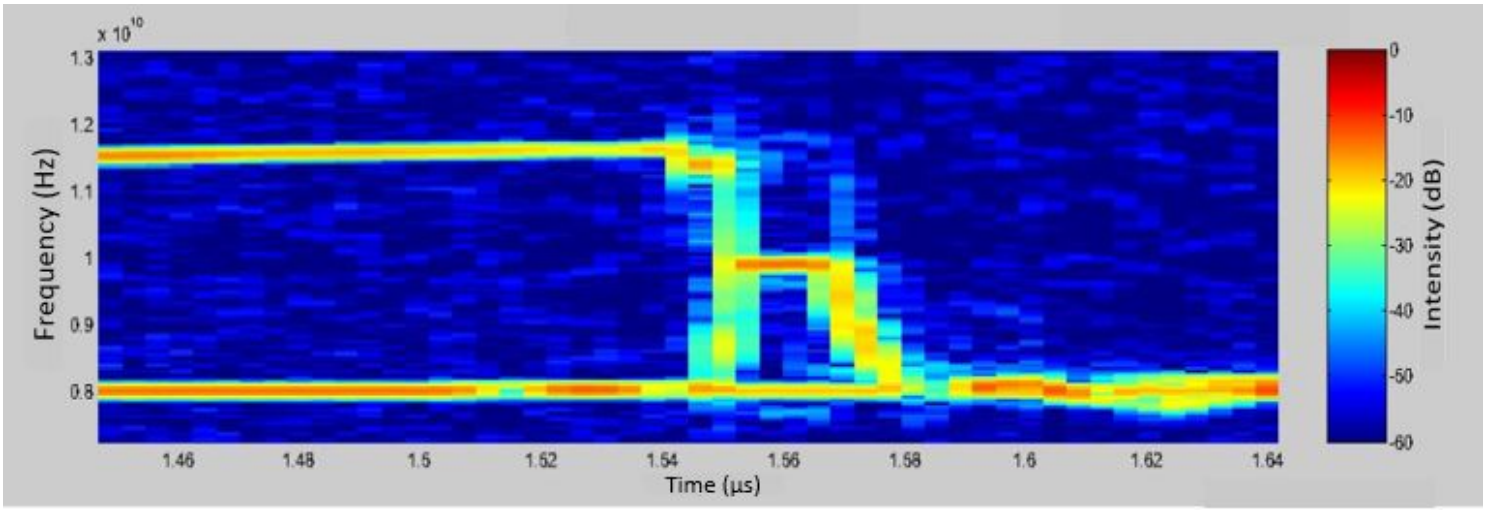

Figure 45. STFT signal of EG-I0125 in SIRHEN

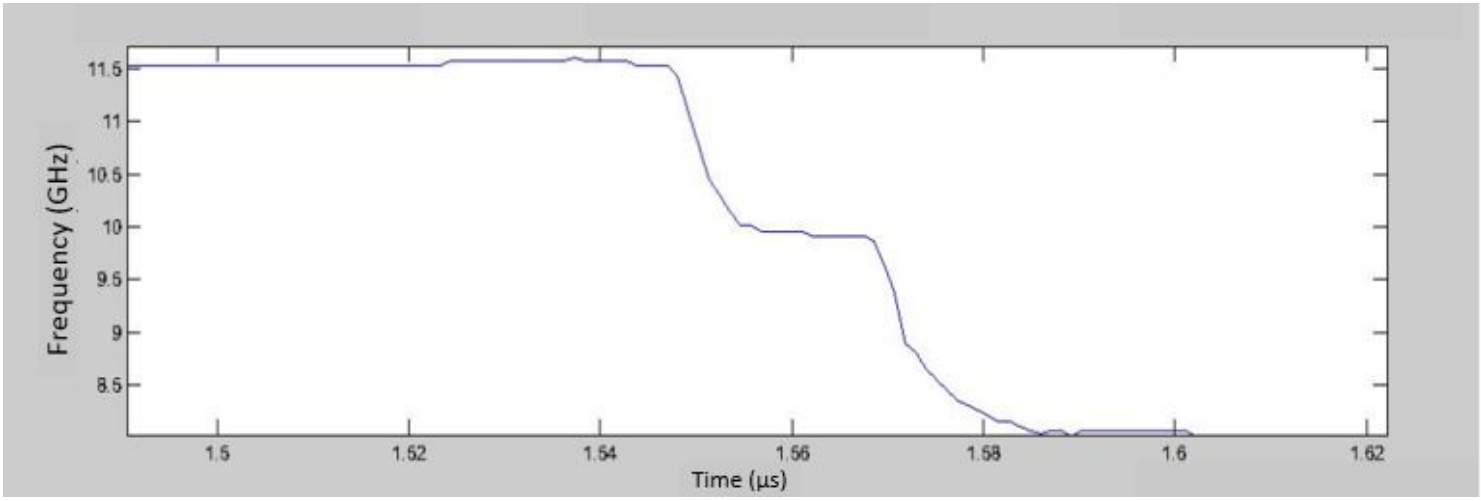

Figure 46. Extracted signal of EG-I0125 in SIRHEN

The data for Figures 45 and 46 can be considered an ideal set of data for its continuity and intensity. The shock plateau in Figure 45 can be clearly seen and the peak frequency in Figure 46 is easily discernible. Figure 46 shows how well defined the shock plateau in this case, as well as the steep deceleration in the chip's velocity.

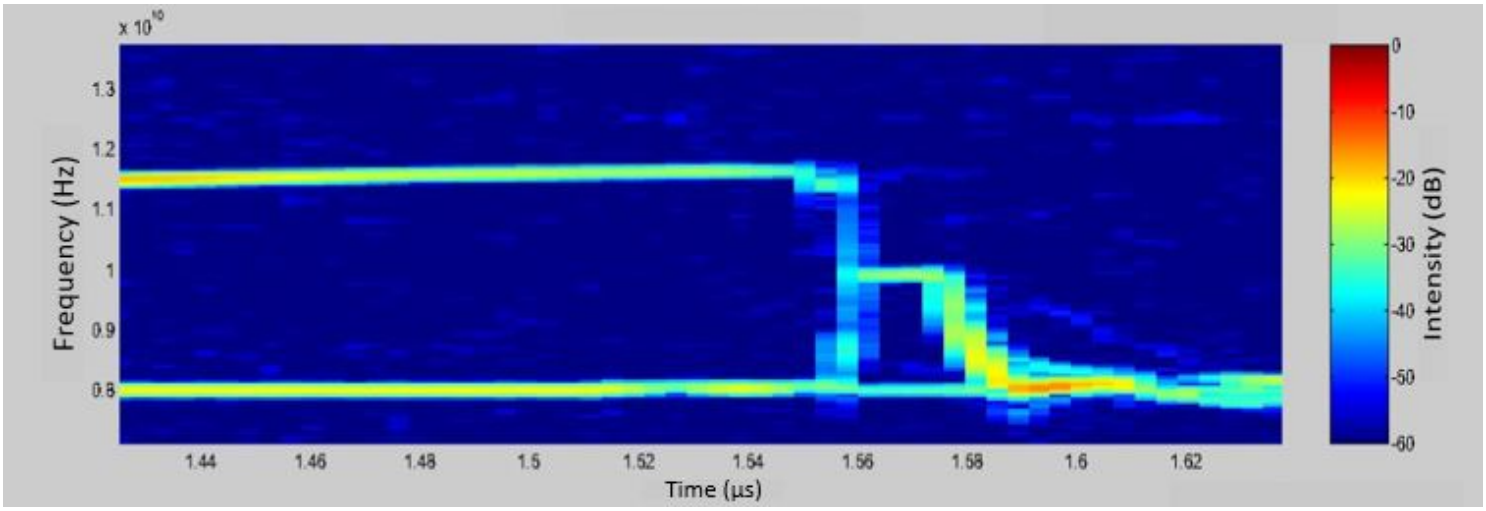

Figure 47. STFT signal of EG-I0126 in SIRHEN

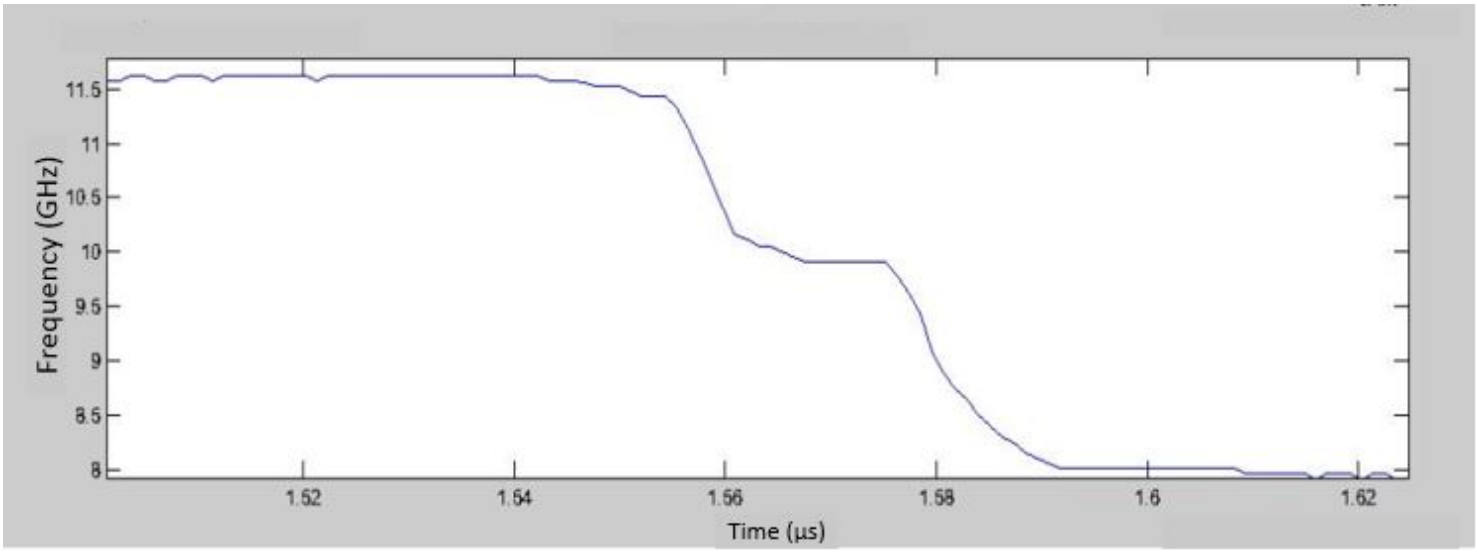

Figure 48. Extracted signal of EG-I0126 in SIRHEN

The last shot data is presented in Figures 47 and 48. Figure 47 shows the PDV captured the chip's deceleration and collision with the PMMA window reasonably accurate at an intensity around -35 dB, but the peak frequency does not have high

resolution. This lack of resolution is shown in Figure 48 where a definitive peak frequency is absent. The peak frequency represents the chip's peak velocity before impact with the PMMA window. It is important to capture this peak frequency because the time from peak velocity to physical collision must be measured in order to improve precision in the timing of shock production.

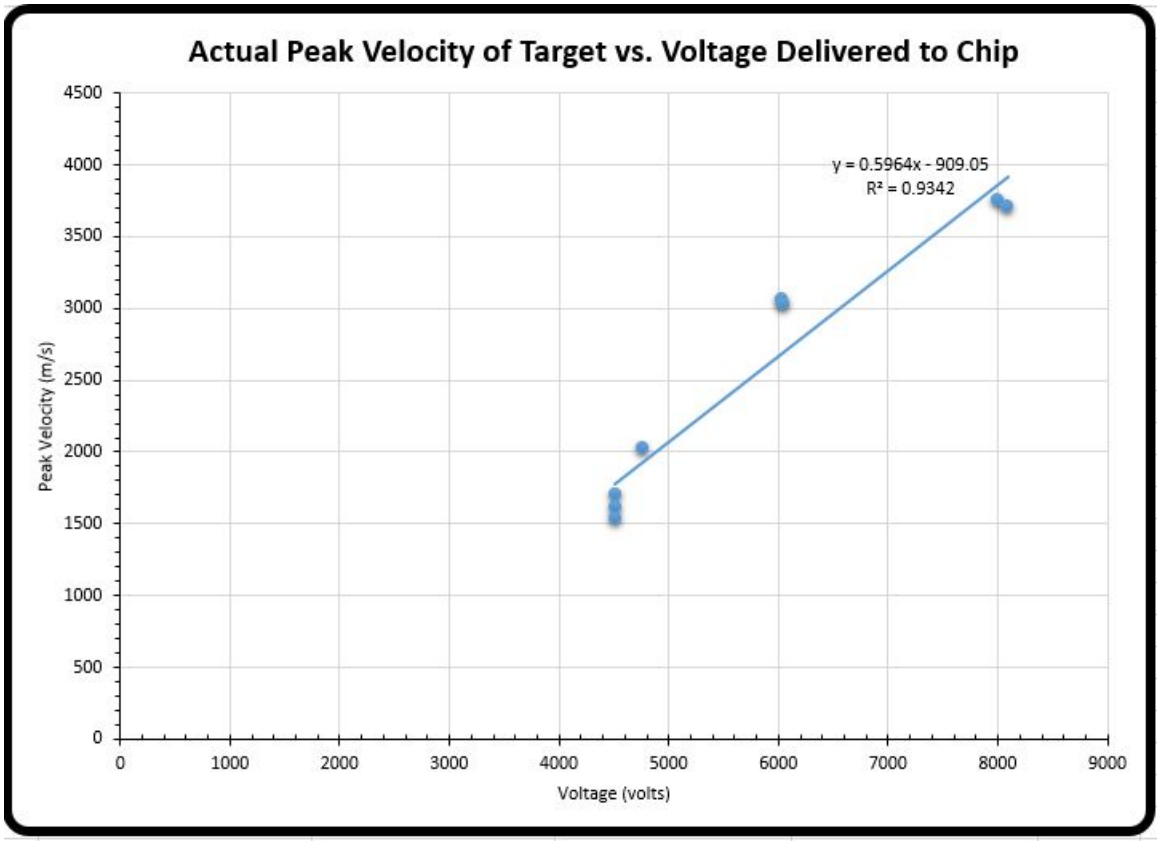

Figure 49. Plotted voltage and peak velocity data of all shots displayed in Microsoft Excel

The peak frequency in each chip slapper experiment does not represent the actual velocity. Although there may be higher frequency peaks in some cases throughout the signal data, it does not necessarily mean that it corresponds to a higher velocity [12]. Those high-frequency peaks merely represent the projected or apparent velocity in some cases. In this thesis, it is safe to assume the highest averaged peak frequency,

as derived by the Gaussian method, is the fastest perceived velocity with a small degree of uncertainty. In order to obtain the actual velocity, the target's natural stationary frequency must be subtracted from the measured peak frequency. This subtraction results in the actual frequency peak because it is being measured from a zero frequency. The actual peak frequency is then converted to the actual peak velocity of the target through the following familiar equation:

$$\overline{v} = \frac{\lambda_0}{2}\overline{f} \tag{32}$$

The results of this calculation were then plotted on Figure 49 against the actual cap voltage delivered to the bridge of each chip. As seen in the figure, the chip's peak velocity ranged from 1500-4000 m/s for each experiment at differing voltages. From this plot, an equation of correlation was obtained that could predict the peak velocity of this specific W76 chip. Error bars are plotted in the chart but could not be seen due to the small magnitude of the uncertainties relative to the actual peak velocity value. The uncertainty values for frequency and velocity will be shown in a table later in this chapter. Further shots must be done with this chip in order to confirm the equation in Figure 49 but it shows the chip's peak velocity is predictable given an actual cap voltage.

Table 4. Table comparing peak frequencies for each shot experiment

Shot Classification	Peak Frequency (GHz) (Gaussian)
EG–I0119	10.0586
EG–I0120	10.1704
EG–I0121	10.5957
EG–I0122	9.96094
EG–I0123	12.7930
EG–I0124	12.7441
EG–I0125	11.9141
EG–I0126	11.8652

Table 4 revealed a general pattern between the resolution of the signal in the STFT and the perceived peak frequency. The resolution of the signal would increase as the peak frequency increased up to a point. After near 11.9 GHz point of peak frequency, the resolution of the frequency would slightly diminish, especially near the discontinuity and shock plateaus. The source of this loss in resolution can come from the fragmentation of material during collision. Fragmentation of the chip became more likely as the actual cap voltage increased, which could result in scattering of the reflected light and loss in target frequency resolution.

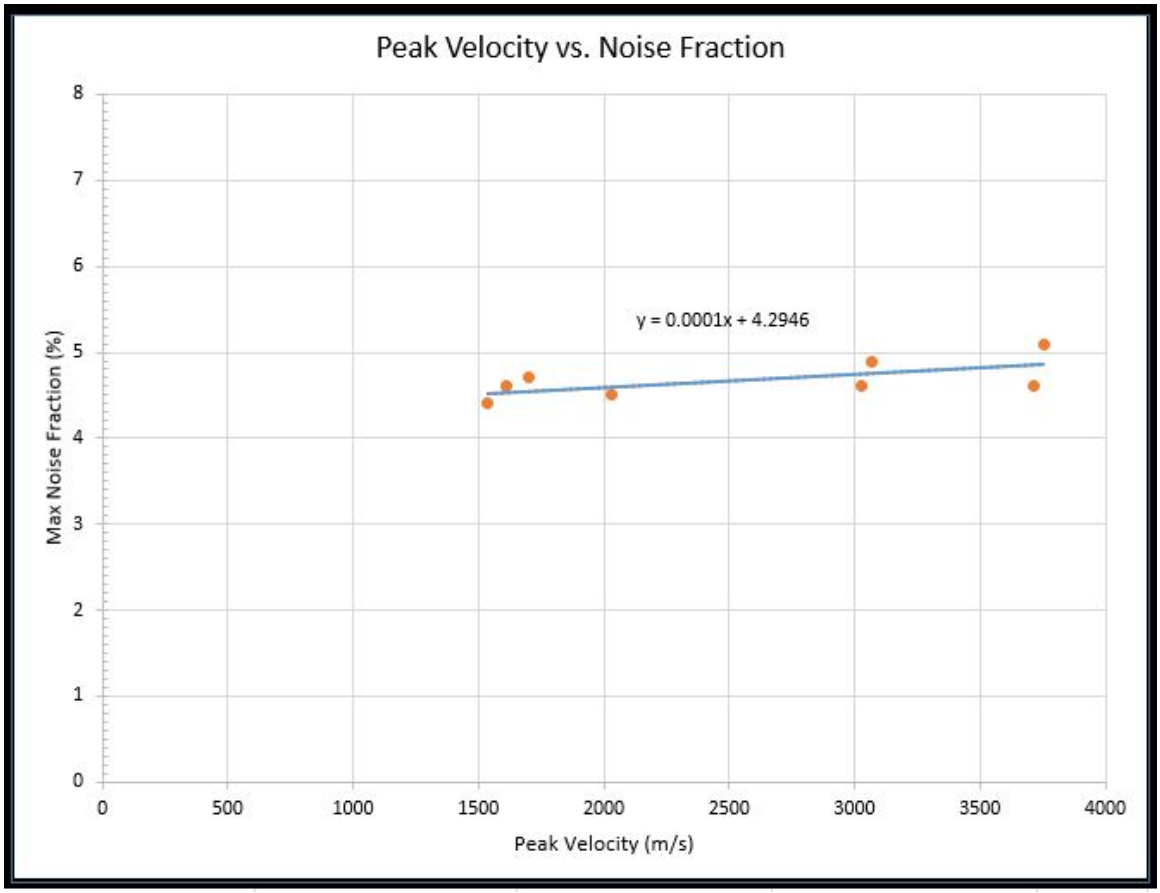

Figure 50. Plotted max noise fraction and peak velocity data of all shots displayed in Microsoft Excel

An investigation of Figure 50 shows that although there is a slight decrease in signal resolution, the noise fraction was reasonably constant given an increase in peak velocity throughout the experiments. The noise fraction would stay between 2 percent and 5 percent, which is acceptable for this thesis. The importance of this constant noise fraction shall be presented in the conclusion.

Table 5. Table listing frequency uncertainties and velocity uncertainties for each shot experiment

Shot Classification	Frequency Uncertainty (Hz)	Velocity Uncertainty (m/s)
EG–I0119	8.1×10^5–1.8×10^6	0.63–1.40
EG–I0120	5.7×10^5–1.8×10^6	0.44–1.40
EG–I0121	6.6×10^5–1.7×10^6	0.51–1.30
EG–I0122	7.1×10^5–1.7×10^6	0.55–1.30
EG–I0123	9.2×10^5–1.9×10^6	0.71–1.51
EG–I0124	8.0×10^5–1.7×10^6	0.62–1.30
EG–I0125	8.4×10^5–1.8×10^6	0.65–1.40
EG–I0126	7.8×10^5–1.7×10^6	0.60–1.30

The frequency and velocity uncertainty also increased with the increase in perceived frequency, as shown in Table 5. If the voltage delivered to the bridge becomes too high, it essentially overloads the PDV system's sensors. According to the data, near 8000 volts is where the frequency resolution begins to slightly deteriorate.

Table 6. Table listing frequency uncertainties and velocity uncertainties for each shot experiment's signal that was filtered

Shot Classification	Noise Fraction	Frequency Uncertainty (Hz)	Velocity Uncertainty (m/s)
EG–I0120	4.3%–2.1×10^2%	1.6×10^6–7.7×10^7	1.2–60
EG–I0122	2.1%–8.4%	7.8×10^5–3.1×10^6	0.61–2.40
EG–I0124	2.4%–8.6%	8.9×10^5–3.2×10^6	0.69–2.50
EG–I0125	2.6%–9.0%	9.5×10^5–3.4×10^6	0.74–2.60
EG–I0126	2.4%–8.5%	8.7×10^5–3.2×10^6	0.68–2.50

Table 6 is displayed in order to show a drawback of using the SIRHEN program. The SIRHEN program does not extract frequency points from prefiltered signals.

Prefiltered signals include any signal that has been filtered by a bandpass or a bandstop. SIRHEN does worse with the bandstop. This error arises from the process of selecting a reference region and an experimental region. SIRHEN compares the two region to help the user evaluate the magnitude of the dynamic limit but if there is not much noise, the user is essentially comparing an experimental region with another experimental region, or at least altered reference region.

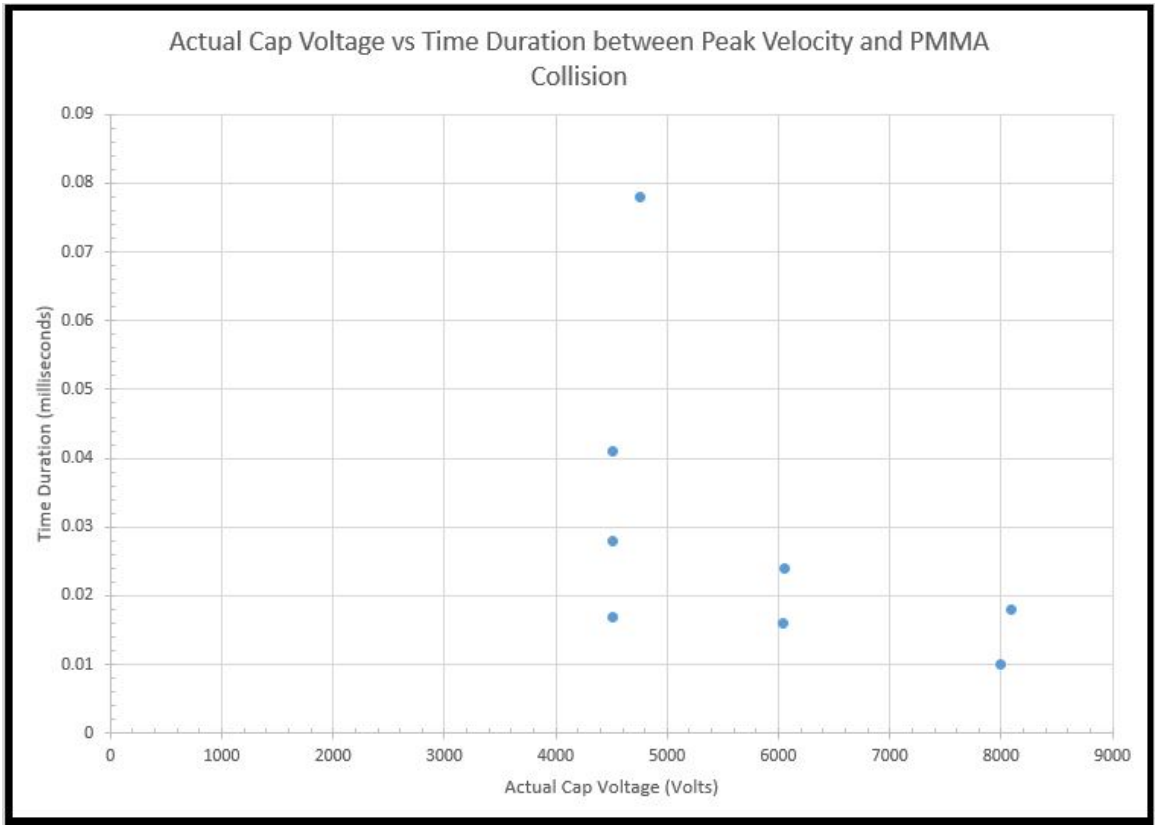

Figure 51. Plotted actual cap voltage and time duration data of all shots displayed in Microsoft Excel

Figure 51 shows the time elapsed for the chip to decelerate from its peak velocity to colliding with the PMMA window. In general, the chip's with the higher velocity (higher actual cap voltage) had shorter time durations than those with lower velocities. This trend does not hold true for all the ship slapper shots because some of

the chips would partially fragment from such high voltage jolts before collision. The reason for this general pattern is because the faster the chip accelerated towards the PMMA window, the faster it would also decelerate due to the formation of the shock in front of the chip interacting with the PMMA window. The faster the chip accelerated, the stronger this shock became which caused faster air drag from the compressed air in between the two materials as the chip approached the PMMA window. The lowest time duration was around 0.01 μs for about 8000 volts charged to the flyer. The digitization and quantification of this deceleration is vital in precise-timing of munition shock detonation.

V. Conclusions

5.1 Data Deductions

The aim of this thesis was to perform an analysis of the PDV system and determine whether the PDV system was prepared for explosive sensitivity testing through shock-solid material interaction. This thesis has proven the standard PDV system located at Eglin AFB is prepared for explosive sensitivity testing by analysis of noise fraction and uncertainty. The PDV becomes less precise as signal intensity decreases, with a reduction of at least 4×10^6 Hz in frequency accuracy, according to this thesis data, but the uncertainty still met PDV laboratory standards. PDV systems typically are accurate to about 1×10^5-1×10^6 Hz when peak frequency measurements are above 2 GHz. Therefore, the thesis data aligns well with past experimental results considering the thesis measurements are well above 2 GHz and accuracy uncertainties in this thesis are comparable in magnitude [9]. Peak velocities measured in this thesis were also comparable to typical detonation velocity criteria for solid explosives, approaching velocities of shock-shock interaction between two solids. Peak velocities were in between 1500-4000 m/s while detonation velocities for most explosives used in combat are between 2000-5000 m/s [7, p. 258-262]. These explosives include forms of TNT, RDX, and PETN.

Noise fraction stayed relatively constant given an increase in peak velocity, which means the noise fraction will continue to be relatively low throughout these velocity regimes. The extraction of true signal from signal randomness will continue to have similar resolution given increases in peak velocity. This extraction means deceleration and shock production from solid collisions can be measured and quantified for improved shock detonation precision in explosives. The decelerations and shock plateaus are what must be captured to better understand shock detonation explosives

and the PDV system demonstrated it is capable of capturing these phenomenons in a cost-efficient manner. These solid-solid impacts are what begin the process to hotspot emergence and eventual deflagration-detonation transition to cause a munition to explode on target. The improvement in munition detonation timing will lead to improved cost-effective warfare, reduction in collateral damage, and more lives saved.

5.1.1 Uncertainty Explanation

Uncertainty in the STFT signal can be attributed to a multitude of factors. The uncertainties can be caused by the thickness of the chips. Several of the chips fragmented during the course of impact against the PMMA window. If the thicker chips were utilized, the signal readings would be more stable because the thicker chips would withstand the impact force with greater durability, resulting in less fragmentation. The pulverization of the chip itself can cause scattering of the Doppler-shifted laser, leading to inaccurate readings from the PDV optical receiver. Perhaps more ductile material can be used in future experiments to minimuze the amount of pulverized material embedded into the PMMA window to reduce light scattering. Also, the sampling rate of the photodiode optic receiver can be increased to reduce uncertainty. The current photodiode has a maximum sampling rate of 20 GHz but there are several photodiode detectors that are commercially available through Photonics with max sampling rates of 50-60 GHz. This purchase would have to be in conjunction with an upgraded oscilloscope in order to accurately capture the voltage data. Oscilloscopes of identical sampling rates are available through Tektronix or Teledyne Lecroy.

5.2 Recommendations for Further Research

Regardless of the plethora of advantages the PDV system has to offer, technology can always be improved upon and must be improved upon if the Air Force expects to continue its air-space dominance and global reach. Although the 4 channel PDV shows great promise in the use of explosive mixture design and munition case engineering, its accuracy and precision can still be improved upon to overcome the discontinuities in the STFT signal. Also, the potential applicability of the PDV system exceeds far beyond just velocimetry and shock wave analysis. The PDV system would be useful in the study of thermally ignited explosives after improving upon the standard PDV configuration itself. Also, PDV systems would work excellently in conjunction with microscaled high-speed cameras in order to better define real world visualizations through digitization.

5.2.1 Green Laser

The Munitions Directorate under AFMC at Eglin AFB has been exploring the potential of comparing the data of a standard PDV configuration against a recently developed PDV configuration. The newly developed PDV configuration would utilize a laser at a wavelength of 532 nanometers, instead of 1550 nanometers. A 532 nm wavelength laser is being considered because it is a standard Nd:YAG laser, therefore it is widely-available in the scientific community. A laser of another color in the visible spectrum would require the development of a new laser which would lead to higher costs. A wavelength of 532 nanometers lies in the visible range of the electromagnetic spectrum, which corresponds to the color green. The wavelength of the standard PDV configuration lies in the infrared range of the electromagnetic spectrum, which means it is invisible to the naked eye.

The invisibility of the standard PDV 1550 nm laser makes it difficult to correctly

align and center the laser against the target, which results in error that cannot be exactly quantified. Another visible laser is required currently to align the standard PDV configuration. With the green laser, another visible laser would not be needed to correctly align the green laser which overall would save the Air Force money spent to maintain and operate another visible laser.

This inherent invisibility of infrared lasers also makes them more dangerous than visible lasers because humans cannot see in what direction the infrared laser is deflecting after it comes in contact with a surface. At least with the visible laser, it is possible to see what direction the laser is deflecting.

The new green laser would have a shorter wavelength than the standard PDV laser, which means the new PDV laser would have a higher frequency. The green laser would have three times the frequency of the standard PDV. This increase in frequency would result in more frequency points in the power spectrum, which means less "zero-padding." Less "zero-padding" means less computational time required to perform fast Fourier transforms or short-time Fourier transforms. Also, the higher frequency from the green laser should result in less uncertainty and smaller error bars than the standard PDV system. The upshifted frequency in the green laser would overall result in better temporal and frequency resolution, which means better velocity resolution as well. The larger amount of data from the green laser would mean more frequency points would have to be recorded in a short time period. The installation of the green laser would have to be in conjunction with upgraded photodiode detectors and oscilloscopes. Higher sampling rates would be needed in order to accurately capture data from the green laser's fringe shift. The green laser was still being constructed before any testing could begin on it and the AIS team is currently in the process of repairing it. If this PDV green laser configuration proves superior, past PDV experiments could be redone for better results, such as the controlled fragmentation

testing done at Eglin Air Force Base in 2010. These improved results from a cost-effective configuration will lead to better munitions in the future.

5.2.2 Study of Explosive Grains

The microstructure of an explosive is a major influence on the detonation behavior [13, p. 1]. With the advent of the green laser in future PDV systems, better resolution will be possible for shock wave interaction with explosives. Stronger quantified correlations were revealed between pressed microstructures and threshold initiation behaviors using a 1550 nm upshifted PDV configuration. In an experiment led by Dr. Welle for AFRL involving explosive microstructure, he used a James like framework model to evaluate pulse duration effects within microstructures. These same pulse duration effects were later quantified by an upshifted PDV configuration. This same experiment hopefully can be revisited once the AIS team installs a green laser in the PDV for better resolution. Dr. Welle states that for future similar experiments, higher shock waves should be produced by using finer grained explosive and thinner flyers for a more versatile data set [13, p. 9].

Another similar experiment was conducted by Dr. Schwarz to investigate shock initiation threshold sensitivity of HNS type explosives [13, p. 2]. He noticed as the individual grains of the explosive grew larger, the narrower was the range of pressures separating detonation from deflagration. This narrow range of pressures can be identified and quantified using PDV systems in future similar experiments. These narrow ranges of pressures can be the difference between detonating on target and predetonating on a civilian.

Bibliography

1. Documented civilian deaths from violence. Iraqi Body Count, 15 February 2015. Accessed 15 Feb 2015.

2. Report on the Protection of Civilians in the Armed Conflict in Iraq: 6 July 2014–10 September 2014. UNITED NATIONS Assistance Mission for Iraq Human Rights Office, 18 August 2014.

3. pTool: Photonic Doppler Velocimetry Analysis Tool. Technical report, NSTec, Los Alamos Operations, 2008.

4. General Curtis E. LeMay, (1906-1990). Public Broadcasting System, 2009. Accessed 14 Feb 2015.

5. Tommy Ao and Daniel Dolan. SIRHEN: a data reduction program for photonic Doppler velocimetry measurements. Technical report, Sandia, 2010.

6. Andrew Beath, Fotini Christia, and Ruben Enikolopov. Winning Hearts and Minds? Evidence from a Field Experiment in Afghanistan. Technical Report 2011-14, Department of Political Science, Massachusetts Institute of Technology, 2012.

7. Paul Cooper. *Explosives Engineering*. Wiley-VCH, Albuquerque, NM, 1996.

8. Air Force Research Lab Munitions Directorate. Controlled Loading Fragmentation: Experiments and Continuum Damage Modeling. `www.DTIC.com`, July 2010. Accessed 13 Feb 2015.

9. D.H. Dolan. Accuracy and Precision in photonic Doppler velocimetry. *Review of Scientific Instruments*, 81, 2010. `rsi.aip.org`.

10. Jennifer Elsea. Terrorism and the Law of War: Trying Terrorists as War Criminals before Military Commissions. Technical report, American Law Division, 2011.

11. Reuven Erlich. The Use of Mosques for Military and Political Purposes by Hamas and Other Terrorist Organizations and Islamic Groups. Think-Israel, 1 March 2009. Article from Israel Intelligence Heritage and Commemoration Center.

12. Daniel Dolan et al. What does "velocity" interferometry really measure? Technical report, LANL and Sandia, 2009.

13. Dr. Eric J. Welle et al. Microstructure effects on the initiation threshold behavior of HMX and PBXN-5. Technical report, Air Force Research Laboratory, 2013.

14. Strand et al. Velocimetry using Heterodyne Techniques. Technical report, LLNL, 2004.

15. Defense Science Board Task Force. Munitions System Reliability. Technical report, United States Department of Defense, 2005.

16. Arnie Heller. Ten Times More Data for Shock-Physics Experiments. *Science and Technology Review*, 2012 Research and Development 100 Awards by Lawrence Livermore National Laboratory, 2012.

17. David B. Holtkamp. Photonic Doppler Velocimetry for Dynamic Experiments. Technical report, LANL, 2011.

18. Samuel King. Explosives research program evolves through statistics. Eglin Air Force Base, 3 Oct 2011. Accessed 13 Feb 2015.

19. Jared Langhals O-1. Explanation of PlotData and pTool. Technical report, Eglin Air Force Base, 2015.

20. Maurice Tugwell. Terrorism and Propaganda: Problem and Response. *Journal of Conflict Studies*, Volume 6, No. 2, Spring 1986.

21. Wikipedia. Acoustic Impedance. `http://en.wikipedia.org/wiki/Acoustic_impedance`, 10 Dec 2014. Accessed 20 Jan 2015.

22. Wikipedia. Vietnam War Casualties. Wikipedia, 14 February 2015. Accessed 15 Feb 2015.

23. Wikipedia. Velocimetry. `http://en.wikipedia.org/wiki/Velocimetry`, 14 Sept 2013. Accessed 29 Nov 2014.

24. Wikipedia. Gulf War. Wikipedia, 15 February 2015. Accessed 15 Feb 2015.

25. Jonas A. Zukas and William P. Walters. *Explosive Effects and Applications*. Springer, New York, NY, 1998.

REPORT DOCUMENTATION PAGE

Form Approved
OMB No. 0704–0188

1. REPORT DATE *(DD–MM–YYYY)*	2. REPORT TYPE	3. DATES COVERED *(From — To)*
03–13–2015	Master's Thesis	Sept 2013 — Mar 2015

4. TITLE AND SUBTITLE

Reflections of a Wave: An Analysis of Photonic Doppler Velocimetry Systems

5a. CONTRACT NUMBER

5b. GRANT NUMBER

5c. PROGRAM ELEMENT NUMBER

6. AUTHOR(S)

Lagrange, Brian K, 2nd Lt.

5d. PROJECT NUMBER

5e. TASK NUMBER

5f. WORK UNIT NUMBER

7. PERFORMING ORGANIZATION NAME(S) AND ADDRESS(ES)

Air Force Institute of Technology
Graduate School of Engineering and Management
2950 Hobson Way
Wright-Patterson AFB OH 45433-7765

8. PERFORMING ORGANIZATION REPORT NUMBER

AFIT-ENY-MS-15-M-242

9. SPONSORING / MONITORING AGENCY NAME(S) AND ADDRESS(ES)

Munitions Directorate
Air Force Research Laboratory (AFRL)
Dr. Eric J. Welle
101 West Eglin Blvd
Eglin AFB FL 32542-6810
Email: eric.welle@us.af.mil

10. SPONSOR/MONITOR'S ACRONYM(S)

AFRL/RWMFS

11. SPONSOR/MONITOR'S REPORT NUMBER(S)

12. DISTRIBUTION / AVAILABILITY STATEMENT

DISTRIBUTION STATEMENT A
APPROVED FOR PUBLIC RELEASE; DISTRIBUTION IS UNLIMITED

13. SUPPLEMENTARY NOTES

This work is declared a work of the U.S. Government and is not subject to copyright protection in the United States.

14. ABSTRACT

Munitions are one of the Air Force's most effective weapons in eliminating targets, but also one of the most expensive. Due to the inherent high-cost in deploying munitions, munition shock wave detonation must be better observed and quantified for munitions to be more cost-efficient. PDV systems have the potential to achieve this quantification of shock wave properties on a molecular scale during solid-aginst-solid impacts. The overall goal of this research was to determine whether the current photonic Doppler velocimetry (PDV) system at Eglin Air Force Base is prepared for future explosive sensitivity testing. This determination was done through an uncertainty analysis of the PDV system's results. The PDV system was given shock detonation velocities comparable to experimental explosive detonation velocities to investigate how well the system performed. This thesis concluded that the current PDV system employed by the Advanced Initiation Sciences team, (Munitions Directorate, AFRL) is capable of explosive sensitivity testing.

15. SUBJECT TERMS

Thesis, photonic Doppler velocimetry, PDV, shock detonation, heterodyne, interferometer

16. SECURITY CLASSIFICATION OF:			17. LIMITATION OF ABSTRACT	18. NUMBER OF PAGES	19a. NAME OF RESPONSIBLE PERSON
a. REPORT	b. ABSTRACT	c. THIS PAGE			Dr. R. B. Greendyke, AFIT/ENY
U	U	U	UU	113	19b. TELEPHONE NUMBER *(include area code)* (937) 785-3636x4567; robert.greendyke@afit.edu